THESIS FOR THE DEGREE OF DOCTOR OF PHILOSOPHY

Reshaping the phase diagram of $YBa_2Cu_3O_{7-\delta}$ through strain in ultrathin films and nanowires

ERIC WAHLBERG

Department of Microtechnology and Nanoscience (MC2)

Quantum Device Physics Laboratory

CHALMERS UNIVERSITY OF TECHNOLOGY

Göteborg, Sweden 2021

Reshaping the phase diagram of $YBa_2Cu_3O_{7-\delta}$ through strain in ultrathin films and nanowires
ERIC WAHLBERG
Göteborg, Sweden 2021
ISBN 978-91-7905-559-2

Doktorsavhandlingar vid Chalmers tekniska högskola
Ny serie Nr 5026
ISSN 0346-718X

Quantum Device Physics Laboratory
Department of Microtechnology and Nanoscience (MC2)
Chalmers University of Technology
SE-412 96 Göteborg, Sweden
Telephone: +46 (0)31-772 1000

Cover
Illustration of the YBCO unit cell and doping mechanism (Left) together with the reshaped phase diagram of strained 10 nm thick YBCO thin films and Hall bars (Right). See page 9 for more information.

Printed by Chalmers Reproservice
Göteborg, Sweden 2021

Reshaping the phase diagram of $YBa_2Cu_3O_{7-\delta}$ through strain in ultrathin films and nanowires

ERIC WAHLBERG
Quantum Device Physics Laboratory
Department of Microtechnology and Nanoscience (MC2)
Chalmers University of Technology

Abstract

This thesis aims at adding important pieces to the puzzle of understanding the physics of the High critical Temperature Superconductor (HTS) cuprates, where despite over 30 years of intense research many open questions remain. The HTS cuprates are characterized by an incredibly complex phase diagram with multiple intertwined local orders, such as charge density waves (CDW). The superconducting state originates from an enigmatic state called "strange metal". One of the defining properties of the strange metal is a surprisingly simple linear temperature dependence of the resistivity, a possible consequence of the strong electron-electron correlations in these materials. This behavior cannot be accounted for by the conventional theories of electric transport and calls for new theoretical and experimental approaches that can give more hints about its true nature.

This thesis describes new experiments that are able to highlight the physics of the strange metal by studying the physical mechanisms that lead to its breakdown, using nanoscale $YBa_2Cu_3O_{7-\delta}$ (YBCO) thin films and devices.

So far, a detailed temperature-doping phase diagram describing the complex properties of the HTS cuprates was available only for single crystals. The first part of the thesis shows that we can reproduce all the main features of the HTS phase diagram for YBCO thin films and nanowires. By reconstructing the surface of the substrates, with high temperature annealing, we are able to grow highly strained, untwinned films. These films are instrumental for studying anisotropic transport properties of both the strange metal and the superconducting state.

In the second part of the thesis we have studied the evolution of the T-linear resistivity in the strained films as a function of the thickness and of the doping. In ultrathin and underdoped YBCO films the strange metal phase is restored when the CDW order, detected by resonant inelastic X-ray scattering, is suppressed. This observation points towards an intimate connection between the onset of CDW and the breakdown of the T-linear resistivity in underdoped cuprates, a link that was missing until now.

Finally, the thesis describes how the phase diagram of YBCO is reshaped for thin films and devices at the nanoscale, and in particular how the superconducting transition is enhanced by the suppression of CDW order in the underdoped regime. We also show that the dynamics of the phase-slip phenomenon in ultrathin nanowires becomes very different in the direction where the CDW order is suppressed. These results highlight the competing nature of superconductivity and charge order.

Overall, the research presented in the thesis work, demonstrates how strain control and nanoscale dimensions allow to manipulate the ground state of HTS which is an important step to disclose the mechanism for high critical temperature superconductivity.

Keywords: High-T_c superconductors, YBCO, underdoped, thin-films, nanowires, strange metal, charge density wave, phase-slip

Acknowledgements

I would like to start by thanking my supervisors Floriana Lombardi and Thilo Bauch for giving me the opportunity to work on such an interesting subject. Floriana, for your strong commitment and inspiring ideas, the endless support and for your encouragement in times of doubt. I hope we will live through another paper! Thilo, for your invaluable insight and support over the years. It has been a pleasure to work with you both.

Thanks to all the current and previous members of our group and QDP who have made this such a nice place for me to spend the last five years in, and to those who have contributed directly or indirectly to my work. Special mention to Riccardo Arpaia, Edoardo Trabaldo, Xavier Palermo, Ananthu Surendran, Silvia Ruffieux, Christoph Pfeiffer, Sobhan Sepheri, Gunta Kunakova, Domenico Montemurro, Marco Arzeo and Reza Baghdadi.

Riccardo, thank you for all your helpful advice and support during the years. You have occasionally been like my third supervisor! I have enjoyed all the experiments we have done together across Europe and celebrating my birthday in strange places. Also for the nice times spent together with you and Edoardo in China and the other conferences we have been to.

I want to give special thanks to Alexei Kalaboukhov who initiated my interest in complex oxide materials through the Masters thesis project that led me to working here at QDP, and for the countless hours he has spent to help and assist me with the AFM, PLD, PPMS and XRD systems.

Also to the MC2 administrative and technical staff for their support during the years. In particular I want to thank Henrik Frederiksen and Mats Hagberg for keeping the cleanroom tools most critical for this work in a good shape.

I am very grateful to all the collaborators that have contributed to this work. Special thanks to Ulf Gran, Giacomo Ghringhelli, Götz Seibold, Sergio Caprara and Marco Grilli for the discussions and your insight on CDWs and their relation to transport.

To my family and friends: thank you for always being there for me and believing in me.

Finally, I want to thank my wife Ellinor for her encouragement, love and support. I am very grateful that you skipped vacation this year and for the extra hours taking care of our daughter Eloise (that woke me up extra early in the morning) so I could finish writing this thesis on time. Jag älskar er!

List of publications

This thesis is based on the work contained in the following papers:

[I] R. Arpaia, **E. Andersson**, E. Trabaldo, T. Bauch, and F. Lombardi, "Probing the phase diagram of cuprates with $YBa_2Cu_3O_{7-\delta}$ thin films and nanowires", *Phys. Rev. Materials* **2**, 024804 (2018).

[II] R. Arpaia, **E. Andersson**, A. Kalaboukhov, E. Schröder, E. Trabaldo, R. Ciancio, G. Dražić, P. Orgiani, T. Bauch, and F. Lombardi, "Untwinned $YBa_2Cu_3O_{7-\delta}$ thin films on MgO substrates: A platform to study strain effects on the local orders in cuprates", *Phys. Rev. Materials* **3**, 114804 (2019).

[III] **E. Andersson**, R. Arpaia, E. Trabaldo, T. Bauch, and F. Lombardi, "Fabrication and electrical transport characterization of high quality underdoped $YBa_2Cu_3O_{7-\delta}$ nanowires", *Supercond. Sci. Technol.* **33**, 064002 (2020).

[IV] **E. Wahlberg**, R. Arpaia, G. Seibold, M. Rossi, R. Fumagalli, E. Trabaldo, N. Brookes, L. Braicovich, S. Caprara, U. Gran, G. Ghiringhelli, T. Bauch, and F. Lombardi, "Restored strange metal phase through suppression of charge density waves in underdoped $YBa_2Cu_3O_{7-\delta}$", *Accepted for publication in Science* `https://doi.org/10.1126/science.abc8372` (2021).

[V] **E. Wahlberg**, R. Arpaia, E. Trabaldo, N. Brookes, G. Ghiringhelli, T. Bauch, and F. Lombardi, "Reshaping the phase diagram of strained, ultrathin $YBa_2Cu_3O_{7-\delta}$ by a unidirectional charge density wave", *To be submitted* (2021).

Papers that are outside the scope of this thesis:

[A] R. Baghdadi, R. Arpaia, E. Stepantsov, M. Arzeo, D. Golubev, D. Montemurro, **E. Andersson**, T. Bauch, and F. Lombardi, "Study of in-plane electrical transport anisotropy of a-axis oriented $YBa_2Cu_3O_{7-\delta}$ nanodevices", *Phys. Rev. B* **95**, 184505 (2017).

[B] E. Trabaldo, M. Arzeo, R. Arpaia, R. Baghdadi, **E. Andersson**, F. Lombardi, and T. Bauch, "Noise properties of YBCO Nanostructures", *IEEE Trans. Appl. Supercond.* **27**, 1–4 (2017).

[C] R Arpaia, S Caprara, R Fumagalli, G De Vecchi, Y. Peng, **E. Andersson**, D Betto, G. De Luca, N. Brookes, F Lombardi, et al., "Dynamical charge density fluctuations pervading the phase diagram of a Cu-based high-T_c superconductor", *Science* **365**, 906–910 (2019).

[D] E. Trabaldo, C. Pfeiffer, **E. Andersson**, R. Arpaia, A. Kalaboukhov, D. Winkler, F. Lombardi, and T. Bauch, "Grooved Dayem nanobridges as building blocks of high-performance $YBa_2Cu_3O_{7-\delta}$ SQUID magnetometers", *Nano Lett.* **19**, 1902–1907 (2019).

[E] E Trabaldo, R Arpaia, M Arzeo, **E. Andersson**, D Golubev, F Lombardi, and T Bauch, "Transport and noise properties of YBCO nanowire based nanoSQUIDs", *Supercond. Sci. Technol.* **32**, 073001 (2019).

[F] E Trabaldo, S Ruffieux, **E. Andersson**, R Arpaia, D Montemurro, J. Schneiderman, A Kalaboukhov, D Winkler, F Lombardi, and T Bauch, "Properties of grooved Dayem bridge based $YBa_2Cu_3O_{7-\delta}$ superconducting quantum interference devices and magnetometers", *Appl. Phys. Lett.* **116**, 132601 (2020).

[G] E. Trabaldo, C. Pfeiffer, **E. Andersson**, M. Chukharkin, R. Arpaia, D Montemurro, A. Kalaboukhov, D. Winkler, F. Lombardi, and T. Bauch, "SQUID magnetometer based on Grooved Dayem nanobridges and a flux transformer", *IEEE Trans. Appl. Supercond.* **30**, 1–4 (2020).

List of symbols and abbreviations

List of symbols

$\delta\rho$	Differential resistivity
δR	Differential resistance
δT_c	Deviation of T_c from parabolic doping dependence
ΔT_c	Width of resistive transition
ΔV_sw	Voltage switch amplitude
ϕ	In-plane angle orientation of device
γ	Temperature derivative of linear $\rho(T)$
Γ	Scattering rate
I_c	Critical current
I_ex	Excess current
J_c	Critical current density
l	Nanowire length
λ_L	London penetration depth
Λ	Quasiparticle diffusion length
N_sw	Fraction of nanowires with hysteretic switching
p	Hole doping, number of holes per planar Cu
P_ann	Oxygen post-annealing pressure
q_CDW	CDW wave vector
ρ	Electrical resistivity
ρ_ch	CuO chain resistivity
ρ_0	Electrical resistivity extrapolated to zero temperature
ρ_N	Normal state resistivity
R_H	Hall coefficient
R_q	Average surface roughness
R_xy	Transverse resistance
σ	Electrical conductivity
T_c	Superconducting critical temperature
T_c^0	Zero resistance T_c
T_c^av	T_c average
T_c^on	T_c onset
$T_\mathrm{CDW}^\mathrm{on}$	CDW onset temperature
T_L	Temperature where linear $\rho(T)$ ends

$T_{\max}$	Temperature of maximum R_{H}
T^*	Pseudogap temperature
t	Thin film thickness
$v_{\mathrm{F,a,b}}$	Fermi velocity component along the YBCO a and b-axes
w	Nanowire width
ξ	Coherence length

List of Abbreviations

AF	Antiferromagnetic
AFM	Atomic force microscopy
ARPES	Angle-resolved photoemission spectroscopy
BSCCO	$Bi_2Sr_2CaCu_2O_{8+x}$
CDF	Charge density fluctuations
CDW	Charge density wave
DC	Direct current
FS	Fermi surface
FWHM	Full width at half maximum
HTS	High critical temperature superconductivity
IV	Current-voltage
LN2	Liquid nitrogen
LSCO	$La_{2-x}Sr_xCuO_4$
NMR	Nuclear magnetic resonance spectroscopy
PDW	Pair density wave
PLD	Pulsed laser deposition
PSC	Phase-slip center
PSL	Phase-slip line
QCP	Quantum cricital point
RIXS	Resonant inelastic X-ray scattering
rlu	Reciprocal lattice units
SDW	Spin density wave
SEM	Scanning electron microscopy
SNSPD	Superconducting nanowire based single photon detector
STM	Scanning tunneling microscopy
STO	$SrTiO_3$
XRD	X-ray diffraction
YBCO	$YBa_2Cu_3O_{7-\delta}$

Contents

1 Introduction

Shortly after the discovery of high critical temperature superconductivity (HTS) in the copper oxide (cuprate) $La_{2-x}Ba_xCuO_4$ in 1986 [1] it became clear that the standard quantum theory of the electronic properties of solids, which has been extremely successful in describing the properties of conventional metals and superconductors, is unable to account for many of the properties of the HTS cuprates. The main reason comes from the fact that they belong to the family of strongly correlated systems [2].

The cuprates are layered compounds where the electronic properties mainly derive from weakly coupled CuO_2 planes. Their quasi-2D nature implies a weak screening of the Coulomb interaction and thus strong correlations between the electrons, which drastically enhances quantum effects.

Perhaps more puzzling than the HTS phenomenon itself is the normal state out of which it emerges. The strong electron-electron correlations give rise to a plethora of different electronic phases whose importance and relation to superconductivity is not clear. When the CuO_2 planes are doped with holes the cuprates evolve from antiferromagnetic insulators at low doping to Fermi-liquid like metals at high doping.

In the intermediate doping range, close to where the superconducting critical temperature (T_c) is highest, the normal state has unconventional properties and is referred to as a "strange metal". One striking property of the strange metal state is a simple linear in temperature behavior of the resistivity from low temperature up to several hundreds K [3], which is a strong violation of any conventional theory of electrical transport in metals. Strange metal behavior has been identified in other strongly correlated materials as well [4, 5], recently in magic angle bilayer graphene [6], and is considered one of the biggest unsolved problems of condensed matter physics [2]. A central problem is to identify the charge scattering mechanism responsible for the linear in T resistivity. One possibility is that the strange metal state is a manifestation of quantum fluctuations originating from a quantum critical point hidden by the HTS state [2, 7, 8]. However, evidence is not yet conclusive.

On the underdoped side of the HTS phase diagram the linear in T resistivity (and the strange metal state) ends by the opening of a partial energy gap at the Fermi level (pseudogap) at the temperature T^* [9]. Just like for the strange metal, the microscopic origin of the pseudogap is not settled. In the pseudogap region (below T^*) of the HTS phase diagram there is a strong tendency for the

formation of intertwined electronic local ordering phenomena that break the rotational/translational symmetry of the system [10–13]. Here charge density wave (CDW) order is the most prominent one [10]. The CDW order is characterized by a biaxial modulation of the charge density in the CuO_2 planes, as measured by resonant inelastic X-ray scattering [10, 14]. It is by now well-established that the CDW order competes with superconductivity [15]. At the doping levels where the CDW order is strong there is a large suppression of T_c [16, 17].

The CDW order might also have implications for the normal state. The experimental finding of small Fermi surface electron pockets, inferred from quantum oscillations in underdoped $YBa_2Cu_3O_{7-\delta}$ (YBCO) [18], seems to points towards an active role of the biaxial CDW to reconstruct the Fermi surface of the cuprates [19, 20]. Currently, there is no consensus on the causality hierarchy among the pseudogap, local orders and the strange metal, or their importance for the HTS phenomenon [21, 22]. The association between the breaking of the T-linear resistivity and the occurrence of the pseudogap has long been speculated [2, 9]. It is however difficult to disentangle the various possible mechanisms leading to the breakdown of the strange metal (pseudogap, CDW order etc.) since they all occur in a small range of temperatures. One way to address this challenge is to tune the local properties of the HTS cuprates. The CDW in particular can be strongly modified by pressure [23, 24], strong magnetic fields [15], or strain in thin films and crystals [25, 26].

So far a detailed phase diagram describing the properties of the HTS cuprates was available only for single crystals [16, 27]. Thin films offer certain advantages over bulk crystals when it comes to tuning of the ground state, such as the possibility to induce a strong strain by the substrate. Furthermore, in thin films the material dimensions can be squeezed down to the nanoscale by reducing the film thickness to a few unit cells or by the fabrication of nanostructures. Since the length scales of the local orders are in the nm range one can get valuable information by studying their characteristics in structures of similar dimensions.

The investigation of HTS at the nanoscale requires high-quality thin films. The structure and morphology of the films and nanostructures should be as close to the bulk material as possible so that any novel findings can be attributed to the intrinsic properties of the material rather than to defects and inhomogeneities. It is extremely challenging to fabricate HTS nanostructures, mainly because of the chemical instability of the material. There are currently a very limited number of reports on underdoped nanostructures, and the results are not very encouraging since the critical temperature of the structures is suppressed, indicating damage [28, 29].

The goal of this thesis is to add important pieces to the understanding of the HTS phase diagram by tuning the ground state of the cuprate $YBa_2Cu_3O_{7-\delta}$ by strain and nanoscale dimensions.

- The first part of the thesis is devoted to reproduce the main features of

the phase diagram in YBCO thin films. We have grown thin films with thicknesses down to the nanoscale and doping levels covering the whole underdoped side of the phase diagram by varying the in-situ oxygen pressure after the film deposition. Furthermore, by reconstruction of the surface of the substrates with high temperature annealing we have been able to grow untwinned films. These are instrumental for studying anisotropic transport properties that characterize the local orders. A fabrication process for underdoped YBCO nanowires retaining the properties of the bulk material has been developed and implemented as a tool to obtain new experimental signatures of the complex properties of HTS materials. The thin film and nanodevices platform developed here can be used to study the interplay between the various orders and phases characterizing the doping dependent phase diagram.

- The second part of the thesis deals with the study of the strange metal phase in nm thick YBCO thin films. We show that the linear in temperature resistivity of strained, ultrathin and underdoped YBCO films is extended to lower temperatures when the CDW order, measured by resonant inelastic X-ray scattering, is suppressed in the YBCO a-axis direction. This observation points towards an intimate connection between the onset of CDW order and the breakdown of the linear resistivity in underdoped cuprates, a link that was missing until now.

- The last part of the thesis describes how the phase diagram of YBCO is reshaped for nanoscale thin films and devices. In particular we show how T_c is enhanced by the suppression the CDW order in underdoped YBCO, and that the CDW induced Fermi surface reconstruction is similar in films with uniaxial and biaxial CDW. We also show how the dynamics of the phase slip phenomenon in nanowires becomes very different in the direction where the CDW order is suppressed.

Overall, the research presented in the thesis work, demonstrates how strain control and nanoscale dimensions allow to manipulate the ground state of HTS, which is an important step to disclose the mechanism for high critical temperature superconductivity.

2 Background

This chapter introduces the topic of the thesis with a brief historical overview of superconductivity up to the discovery of high critical temperature superconductors. The sections that follow focus on the details of the properties of $YBa_2Cu_3O_{7-\delta}$ and provides the necessary background for the rest of the thesis.

2.1 Historical overview of superconductivity

The first sign of superconductivity was discovered in Leiden 1911 by the Dutch physicist H. Kamerlingh Onnes [30]. Three years earlier he successfully liquefied helium which made refrigeration down to temperatures of a few kelvin ($\approx -269°$ C) possible. During the measurements of the electrical resistance of certain metals such as mercury and lead, at liquid helium temperatures, Kamerlingh Onnes found that, below a critical temperature T_c, that depended on the metal, the electrical resistance completely disappeared within a narrow temperature interval (perfect conductivity). This finding was very surprising and the start of an extensive campaign to understand the phenomena of superconductivity.

In addition to the finite T_c there is another property that characterise the superconductivity phenomenon: the Meissner effect. In 1933 the German physicists W. Meissner and R. Ochsenfeld discovered that a magnetic field is expelled from the superconductor when it is cooled below T_c [31].

In 1935 the two German-English physicists F. and H. London proposed two equations to describe the electrodynamics of superconductors [32]. The so called London equations are

$$\frac{\partial \mathbf{J}_s}{\partial t} = \frac{n_s e^{*2}}{m^*}\mathbf{E} \tag{2.1}$$

$$\nabla \times \mathbf{J}_s = \frac{n_s e^{*2}}{m^*}\mathbf{B} \tag{2.2}$$

where $\mathbf{J}_s$ is the superconducting current density, $\mathbf{E}$ and $\mathbf{B}$ are the electric and magnetic fields inside the superconductor and n_s, m^* and e^* are the density of superelectrons (that convey current without dissipation), the mass and the electric charge of the superconducting charge carriers respectively.

The first London equation (2.1) describes the property of perfect conductivity: a finite electric field accelerates the superconducting electrons without resistance

and a constant supercurrent $\mathbf{J}_\mathrm{s}$ can be sustained without dissipation and zero electric field.

The second London equation (2.2) describes the Meissner effect: when combined with Ampère's law $\nabla \times \mathbf{B} = \mu_0 \mathbf{J}$, where μ_0 is the vacuum permeability, one gets the following expressions for the magnetic field:

$$\nabla^2 \mathbf{B} = \frac{1}{\lambda_\mathrm{L}^2}\mathbf{B}, \qquad \lambda_\mathrm{L} = \sqrt{\frac{m^*}{\mu_0 n_\mathrm{s} e^{*2}}} \tag{2.3}$$

The solution of equation (2.3) gives an exponentially decaying magnetic field at the surface of the superconductor which implies that the magnetic field is screened from the bulk of the superconductor and is only present to a certain depth. This characteristic length scale is the so-called London penetration depth λ_L. The magnetic field exclusion from the bulk of the superconductor breaks down, together with the perfect conductivity, at a certain critical field B_c.

Although the London equations were instrumental to understand the Meissner effect, they have major limitations in describing some aspects of superconductors, such as their properties in strong magnetic fields close to B_c, and when the density of superelectrons n_s has spatial variations. This fact was recognized by the Russian physicists V. Ginzburg and L. Landau, who proposed their Ginzburg-Landau theory of superconductivity in 1950 [33]. The theory is based on Landau's previously developed theory of second-order phase transitions and introduced the complex order parameter ψ which relates to the density of superconducting electrons through $n_\mathrm{s} = |\psi(\vec{r})|^2$ where $\vec{r}$ is the position.

The Ginzburg-Landau theory introduces a new length scale for superconductors in addition to λ_L: the Ginzburg-Landau coherence length ξ. The relation between ξ and ψ can be expressed in a form similar to equation 2.3 for λ_L (if $|\psi|$ is small and $\mathbf{B} = 0$) :

$$\nabla^2 \psi = \frac{1}{\xi^2}\psi, \qquad \xi = \sqrt{\frac{\hbar^2}{2m\,|\alpha|}} \tag{2.4}$$

where α is a material dependent constant. Here ξ can be thought of as a length that represents the variation of ψ in the superconductor.

The ratio between the coherence length and the London penetration depth $\kappa = \frac{\lambda}{\xi}$ is called the Ginzburg-Landau parameter and is used to divide all superconductors in two groups (type I and type II) according to how the superconductivity interacts with a magnetic field. In type I superconductors ($\kappa < 1/\sqrt{2}$) the magnetic field is expelled from the bulk up to $B = B_\mathrm{c}$. In 1957 the Russian physicist A. A. Abrikosov showed that the behavior of type II superconductors is remarkably different [34]. He found that when $\kappa > 1/\sqrt{2}$ it is energetically favourable for the magnetic field to penetrate in a regular array of flux lines, where the magnetic flux of each line is the flux quantum $\phi_0 = \frac{h}{2e}$. The flux lines start to penetrate the

Material	Type	T_c (K)	Δ (meV)	λ_0 (nm)	ξ_0 (nm)	$B_c; B_{c,2}$ (T)
Al	I (LTS)	1.18	0.18	50	1600	0.01
NbN	II (LTS)	16	1-3	200	5	40
$YBa_2Cu_3O_{6.9}$	II (HTS)	93	20-25	100-300	1-3	120

Table 2.1: Comparison of superconducting characteristics of different types of superconductors [35]. For YBCO the parameters reported are for in-plane except for $B_{c,2}$ which is for an out-of-plane field (normally used in experiments). The values for NbN are approximate since they depend on how the material is prepared.

superconductor at a lower critical field $B_{c,1}$ and as the field increases the density of flux lines increase until the upper critical field $B_{c,2}$ where they overlap and the entire superconductor turns normal. B_{c2} in type II superconductors can be significantly larger than B_c in type I superconductors which enables their use for high magnetic field electromagnets; see table 2.1 for a comparison between different types of superconductors.

The Ginzburg-Landau theory is very successful in describing the properties of superconductors, but as it is a phenomenological theory it does not tell anything about the microscopic mechanism of superconductivity. In 1957, the same year as Abrikosov's paper, the American physicists J. Bardeen, L. Cooper, and J. R. Schrieffer published their famous BCS theory which settled the microscopic mechanism of superconductivity [36]. Experiments had suggested that the superconducting charge carriers are pairs of electrons (Cooper pairs), and that are separated from the normal conducting electrons by an energy gap at the Fermi level. In the BCS theory electrons of opposite spin and momentum close to the Fermi level pair up at $T < T_c$ to form bosons that all condense to the ground state. The theory predicted a minimum energy 2Δ that is required to break a Cooper pair and the calculated energy gap Δ corresponded well to the measurements. The electron pairing is caused by a weakly attractive potential, that in the case of conventional superconductors comes from electron-phonon interactions, as confirmed by the proportionality between T_c and the ion mass in superconductors of different isotopes of the same material (the isotope effect).

Following the discovery of superconductivity in 1911 new materials with higher T_c were discovered in a slow but steady pace and reached 23.2 K for Nb_3Ge in 1973 [37]. In the following decade no new materials were found, and there were doubts that a much higher T_c was possible. However, in 1986 the German and Swiss physicists G. Bednorz and A. Müller reported $T_c \approx 35$ K in a mixed lanthanum barium copper oxide compound [1]. The discovery stimulated research groups all over the world to look for superconductivity in similar materials which increased the maximum T_c in ambient pressure up to 135 K [38]. The most studied materials include $La_{2-x}Sr_xCuO_4$ (LSCO) $T_c \sim 40$ K, $YBa_2Cu_3O_{7-\delta}$ (YBCO) $T_c \sim 93$ K and $Bi_2Sr_2CaCu_2O_{8+x}$ (BSCCO) $T_c \sim 96$ K.

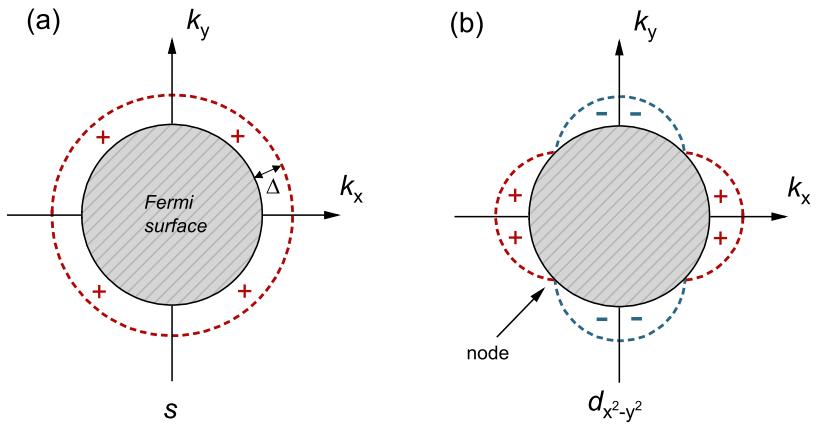

Figure 2.1: Illustration of the superconducting energy gap for (a) s-wave order parameter and (b) $d_{x^2-y^2}$ order parameter on a circular Fermi surface. The superconducting gap Δ and the sign of the phase of the order parameter is shown together with the presence of nodes in (b).

The common element of these so called cuprate high-T_c superconductors (HTS) is that they are layered compounds where CuO_2 planes dominate the electronic properties of the materials. The CuO_2 planes are only weakly coupled which results in very different properties measured in- and out-of-plane. The cuprates are strong type II superconductors with $\xi << \lambda$ and B_{c2} in the order of 100 T [39], see table 2.1 for a comparison to other materials. In contrast to conventional low-T_c superconductors (LTS) where the superconducting energy gap is isotropic in momentum space (s-wave order parameter), the gap in cuprates is strongly anisotropic. Phase sensitive experiments have shown that the gap predominately has a $d_{x^2-y^2}$ orbital character with a gap maximum along the Cu-O bonds and nodes along the diagonals [40], see figure 2.1.

Another characteristic of the cuprates is their rich electronic phase diagrams which is a consequence of the two-dimensional character of the CuO_2 planes and the low charge carrier density that causes strong electron-electron correlations [2]. By doping holes into the CuO_2 planes [41] the materials change from antiferromagnetic insulators to high-T_c superconductors including more exotic orders such as charge and spin density waves.

The microscopic mechanism of superconductivity in the cuprates is not settled despite over 30 years of extensive research on the subject. What seems clear is that the electron pairing is different compared to LTS, probably of electronic origin and possibly through magnetic interactions [42]. Furthermore, the complex phase diagram of the normal state is not well understood, and the importance of the different orders for superconductivity is an open question.

2.2 The high-T_c superconductor $YBa_2Cu_3O_{7-\delta}$

YBCO is one of the most studied cuprates. The main reason is that it is easy to grow high quality crystals with limited impact of impurities and defects on the material properties.

Crystal structure and oxygen hole doping

The unit cell of YBCO consists of three stacked, defect perovskite cells that can be visualized as an alternation of CuO_x, BaO, CuO_2 and Y planes [35, 44], see figure 2.2. In the undoped parent compound $YBa_2Cu_3O_6$ there is no oxygen in the outer CuO_x-planes ($x = 0$) and the unit cell is tetragonal with equal in-plane lattice parameters a and b [43]. When additional oxygen atoms are introduced they end up in the outer CuO_x-planes and form quasi-one-dimensional CuO chains running along the b-axis. The amount of oxygen in the CuO chains control the doping of the material since the oxygen attracts electrons from the CuO_2 planes and thus cause an effective hole-doping [43]. In $YBa_2Cu_3O_7$ all chain sites are filled ($x = 1$). The CuO chains cause an anisotropy in the structure that results in a transition to an orthorhombic unit cell with $b>a$. The increased level of oxygen also has an adhesive effect: the out-of-plane c-axis decreases in length with increasing oxygen content [43].

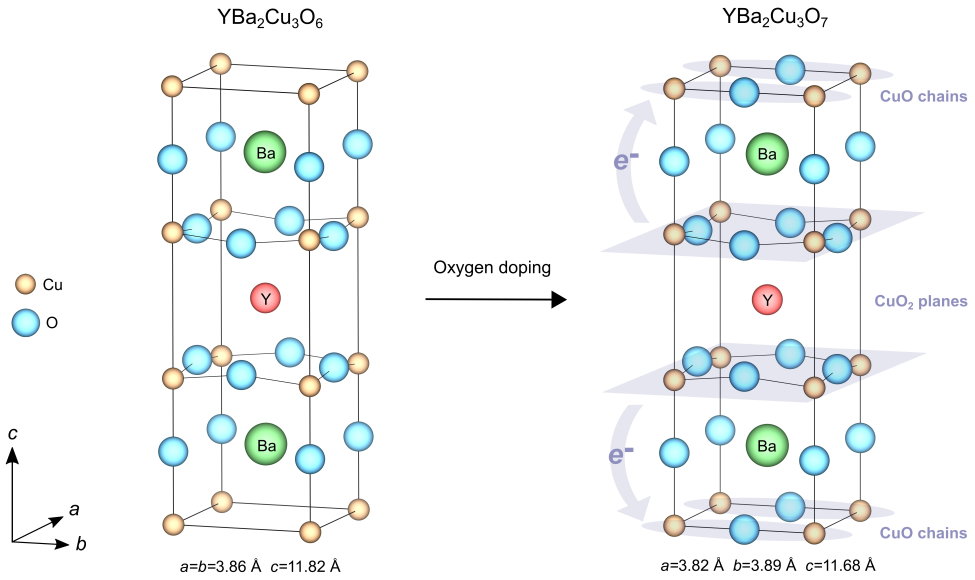

Figure 2.2: Illustration of the crystal structure and hole doping mechanism of YBCO. The left picture shows the tetragonal undoped parent compound $YBa_2Cu_3O_6$ and the right picture the orthorhombic fully oxygenated $YBa_2Cu_3O_7$. The CuO chains and the CuO_2 planes are highlighted in the right picture together with the hole doping mechanism [43].

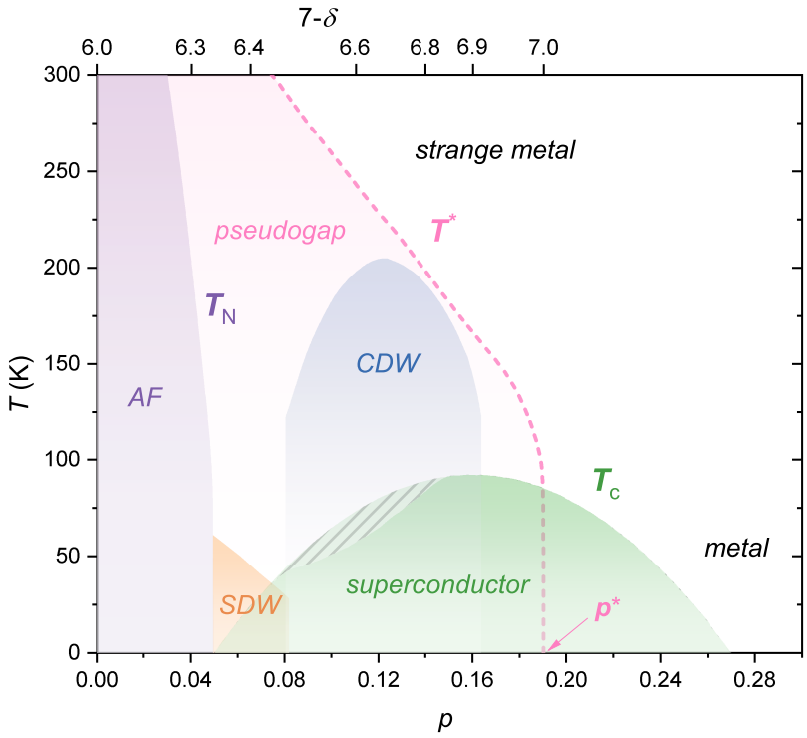

Figure 2.3: Phase diagram of YBCO. On the bottom x-axis, p is the number of holes per planar Cu; on the top x-axis 7-δ is the oxygen content. From left to right: antiferromagnetic order (AF) below the Néel temperature T_N, spin density waves (SDW), charge density wave (CDW), superconductivity below the critical temperature T_c, pseudogap below T^* (that terminates at $p^* \approx 0.19$), strange metal above T^* and conventional metal at high doping and low temperature.

Electronic phase diagram

Undoped $YBa_2Cu_3O_6$ is insulating, but as holes are introduced in the CuO_2 planes the charge carrier concentration increases and the material becomes metallic and superconducting below T_c. The doping level of cuprates is commonly expressed as p, the number of holes per planar Cu atom. This allows a comparison between different cuprates with different doping mechanisms. In YBCO there is a non-linear relation between p and $7 - \delta$, the amount of oxygen in the YBCO unit cell [17]. The temperature-doping phase diagram of YBCO is presented in figure 2.3. It is incredibly complex with numerous intertwined electronic orders in addition to superconductivity. In the following sections we will go into some details of each phase.

Superconductivity

In YBCO superconductivity spans the doping range $0.05 < p < 0.27$. $T_c(p)$ is parabolic with the maximum T_c=93 K close to $p = 0.16$ which is called optimal doping. Samples with doping levels $p < 0.16$ are called underdoped and with $p > 0.16$ overdoped. The T_c deviates from the parabolic doping dependence around $p \approx 0.125$ where it is suppressed by up to 20 K [17] (see the striped green area in figure 2.3). The suppression of T_c is commonly attributed to competition with charge order that is strong in this doping range [15] (see more in the section on charge order).

Strange metal

The normal state around optimal doping in YBCO is called "strange metal". Quickly after the discovery of high-T_c superconductivity in the cuprates researchers realized that the electronic properties of the normal state deviated from what is expected for a metal [2]. The basic properties of normal metals are well described by Landau's Fermi-liquid theory [45], which introduces the concept of quasiparticles. Essentially, the metal with many-body interactions is, in many ways, equivalent to a metal without many-body interactions but with quasiparticle excitations that have different dynamical properties, like mass, than a free electron (or hole). A defining property of a Fermi liquid is that electron-electron interactions results in a T^2 dependence of the resistivity at low temperature [45]. In the cuprates however, the resistivity has a linear T dependence down to the lowest T at optimal doping [3, 46, 47]. Furthermore, the linear T dependence extends up to several hundreds K [3, 48]. There is a theoretical upper limit for the resistivity of metals, where the mean-free path of the electrons is equal to the inter-atomic spacing [49]. When this limit is reached the resistivity should saturate, which it does not in the cuprates. Other signatures of the strange metal include the absence of a sharp quasiparticle peak in the electronic spectra measured by angle resolved photoemission spectroscopy [50] and a non-Drude like frequency dependence of the optical conductivity [51].

The central problem in the physics of the strange metal is to identify the scattering mechanism that causes the linear resistivity [52]. One possibility is that it is the consequence of quantum fluctuations originating from a quantum critical point (QCP) at T=0 and $p = p^*$ inside the superconducting dome [53] (see figure 2.3). There are signatures of a QCP in the cuprates such as a diverging effective mass [54], but the evidence is not conclusive. As recently suggested [46], the linear resistivity can come from the charge carrier scattering rate reaching the Planckian limit $\tau = k_B T/\hbar$, which is the maximum rate at which energy can be dissipated [55]. The Planckian limit and the T-linear resistivity is predicted right above a QCP in the theory of quantum phase transitions [7].

On the overdoped side of the phase diagram normal metallic behavior with a T^2 resistivity is recovered at high doping and low temperature [56]. On the

underdoped side the strange metal phase ends by the opening of a *pseudogap*.

Pseudogap

The pseudogap phase is present in the underdoped side of the cuprate phase diagram below the temperature T^*. It was first discovered by ARPES as a partial gap in the low-energy electronic spectrum [57]. In the strange metal phase the Fermi surface is a large hole-like cylinder centered at (π,π) in the first Brillouin zone, see figure 2.4 [35, 44]. As T^* is crossed, the Fermi surface is gapped around $(0,\pm\pi)$ and $(\pm\pi,0)$, with a symmetry similar to the superconducting order parameter that has nodes along the diagonals (figure 2.1) [57]. The resulting open sheets of Fermi surface are often referred to as Fermi arcs [58]. A translational symmetry breaking order can reconstruct a large Fermi surface to small pockets through zone-folding, but not to open Fermi arcs. A possibility is that the arc is part of a closed pocket that is not fully visible in the spectroscopic measurements [2]. Another signature of the pseudogap is that the resistivity deviates from the linear T dependence of the strange metal close to T^* [48, 59, 60]. This is surprising as a gap at the Fermi level usually increases the resistivity. T^* has a roughly linear p dependence in the underdoped side of the phase diagram and abruptly ends in the overdoped side at $p \approx 0.19$ [61] (see figure 2.3). The origin of the pseudogap is presently unknown. A complicating fact is that a plethora of different electronic phenomena have been reported close to T^* and their relation to the pseudogap is not settled. Examples include electronic nematicity [11], loop current order [13] and charge order [10, 14].

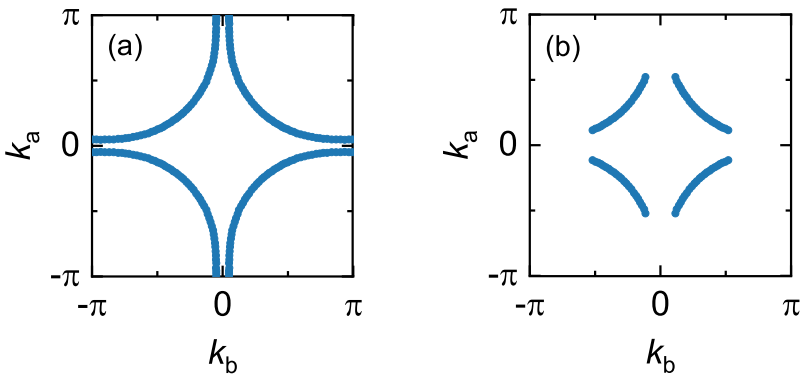

Figure 2.4: Model Fermi surface of the cuprates (a) at room temperature (b) below T^*, in the pseudogap phase. The effect of the CuO chains and bi-layer splitting is disregarded.

Charge order

In a large portion of the underdoped side of the phase diagram there is charge order in the form of charge density waves (CDW) [10, 15]. CDW is a periodic

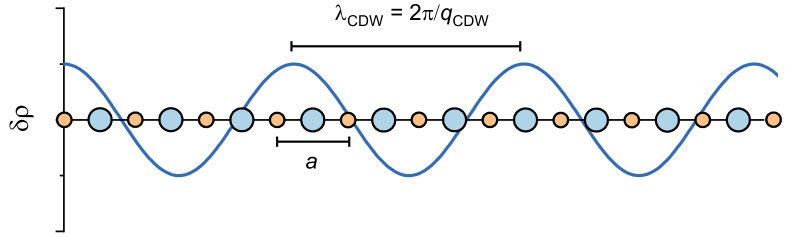

Figure 2.5: Simplified picture of the incommensurate CDW in YBCO. The yellow and blue circles represent the Cu and O atoms of the CuO_2 planes seen from the side. $\delta\rho$ is the deviation of the charge density from the average value, a the lattice constant and λ_{CDW} the wavelength of the charge density modulation.

modulation of the charge density in the CuO_2 planes [62]. It is present in the doping range $0.08 \lesssim p \lesssim 0.17$ and the onset temperature has a dome-shape doping dependence with a maximum at $p \approx 0.12$ [14] , see figure 2.3. For YBCO the CDW q-vector ($q_{\mathrm{CDW}} \approx 0.31$ reciprocal lattice units (rlu) at $p \approx 0.12$) is incommensurate with the lattice (see figure 2.5 for a simple illustration). The charge modulations are biaxial (present along both the YBCO a- and b-axis) with equal amplitude along the two directions at $p \approx 0.12$ and slight anisotropy at higher and lower p [14]. The in-plane correlation length of the CDW order is up to 75 Å(≈ 20 lattice constants) at $p \approx 0.12$ [14] , and there is very little correlation in the c-axis direction [10].

A 3D CDW that is correlated along the c-axis has been found at low temperature and high magnetic field [22, 63]. In contrast to the quasi-2D CDW in zero field the 3D CDW is uniaxial along the b-axis.

There is compelling evidence that the CDW competes with superconductivity. The amplitude of the CDW order increases with decreasing T, but reaches a maximum at T_{c}, decreasing below [10, 15]. Furthermore, the deviation of $T_{\mathrm{c}}(p)$ from the parabolic p-dependence is largest at $p \approx 0.12$ [16, 17] (often referred to as 1/8 doping) where the CDW is strongest, and the CDW amplitude increases if superconductivity is weakened by a magnetic field and vice versa [15, 64].

In the doping range were CDW order is present, quantum oscillations of e.g. the transverse and longitudinal resistivity in magnetic field have been reported [18, 20] The quantum oscillations indicate the presence of a closed Fermi surface and coherent quasiparticles. The main oscillation frequency corresponds to a Fermi surface area of only 2% of the Brillouin zone, which is not compatible with the large hole-like cylinder of overdoped YBCO or the open Fermi arcs of the pseudogap region, as seen in figure 2.4. Another hint of the character of the Fermi surface in the CDW phase comes from Hall measurements. The Hall coefficient R_{H} changes from positive at high T to negative at low T which indicates a transformation from hole-like to electron-like transport [65] This together with the quantum oscillations points towards a scenario where the CDW order induces

a Fermi surface transformation to small electron pockets [66]. The mechanism of this transformation is not settled, but in the simplest scenario the pockets are created by zone-folding of the Fermi surface by $\boldsymbol{q}_{\mathrm{CDW}}$ along the a- and b-axis where the Fermi arcs form the outline of the pockets [19, 67].

Recently, dynamical CDW fluctuations present in the majority of the phase diagram were discovered, even in the strange metal phase [68]. There are conjectures that these fluctuations provide the scattering mechanism of the strange metal [52].

Spin order
At p=0 YBCO is an antiferromagnetic (AF) Mott insulator [69] In a Mott insulator the electrons are localized because of strong Coulomb interactions between electrons on neighbouring lattice sites, characteristic of strongly correlated materials [2]. The antiferromagnetic order is quickly suppressed when YBCO is doped: the Néel temperature T_{N} goes to 0 at $p \approx 0.05$ [70]. Above this doping there is another kind of spin order present, spin density wave order (SDW), which is a periodic modulation of the electronic spin density [71, 72]. In contrast to the AF order at low doping the SDW order is incommensurate and is uniaxial along the YBCO a-axis. At low temperatures (few K) the SDW order is static and slowly fluctuating at higher T [70, 72, 73].

Key differences between different cuprate families Most of the orders presented in the previous section are generic in all different cuprate families (with different onset temperatures and doping levels), but there are some key differences. The most notable one is the so called stripe order in the LBCO cuprate family [12, 74]. In YBCO the CDW and SDW orders are separated (with slight overlap at $p \approx 0.08$) [27] while in the stripe order state they are intertwined. There is evidence for an exotic state called pair density wave (PDW) in stripe ordered LBCO [75]. The PDW is characterized by a periodic spatial modulation of the cooper-pair density and a finite momentum [76]. The PDW order has also been found in BSCCO which could mean that it is a generic phase of the cuprates [77]. The PDW state is one of the candidates to explain the pseudogap [76].

Theory of high-T_{c} superconductivity

Although there is not a generally accepted theory of the high-T_{c} superconductivity in the cuprates, some scenarios have attracted more attention than others [42]. Many theories have their starting point in the Hubbard model, which is used to describe the physics of the undoped antiferromagnetic insulator [78]. In these models the electron pairing is mediated by electron-electron spin interactions that usually result in a d-wave order parameter (as in figure2.1(b)). Notable examples include the resonant valence bond theory, which was devised shortly after the

discovery of high-T_c superconductivity [79].

One problem with the theoretical models is that it is very difficult to capture the full picture of the cuprates, including the different intertwined orders described here (that may or may not be important for the mechanism of superconductivity), within a single theoretical approach [80].

Studies of the phase diagram in thin films and nanostructures

In this chapter we have briefly described the complex properties of the cuprates through the phase diagram of figure 2.3. As we discussed in the introduction, the relation between the different electronic and spin orders and their relevance for high-T_c superconductivity is not settled. One way of simplifying the picture is to tune one of the orders by e.g. strain or magnetic field and observe how it impacts the other orders. In this way one can learn about their intertwining. In crystalline thin films a strong strain can be imposed at the substrate/film interface [81]. The strain can be tuned by changing the thickness of the film. Thin films can also be patterned into nanostructures that have dimensions similar to the ones involved in the ordering phenomena, such as the CDW correlation length. At these length scales the intertwining of the orders might change and give valuable information about their origin. These facts have motivated us to study the phase diagram of $YBa_2Cu_3O_{7-\delta}$ in thin films and nanostructures, which is the subject of this thesis.

3 $YBa_2Cu_3O_{7-\delta}$ thin film deposition and characterization

The high-T_c cuprates are challenging materials to grow in thin film form. Many of their transport properties critically depend on the crystallinity and the specific structure of the unit cell, that can be tuned by strain. In literature two kinds of samples are used: single crystals and thin films. In this thesis work we employ YBCO thin films for our experiments. Here we will describe the process of YBCO thin film deposition and the morphological,structural and electrical transport characterization of the films.

3.1 Thin film deposition

One of the key challenges in YBCO growth is to get the correct stoichiometry of the deposited thin film, since the structure is very complex. Another challenge is to get homogeneous thin films with smooth surfaces and high crystalline quality, which is crucial for fundamental studies of the material and for fabrication of high quality nanodevices. Mainly two methods are used today for deposition of YBCO thin films: pulsed laser deposition (PLD) and high pressure DC magnetron sputtering. Figure 3.1 illustrates the PLD system we have used for YBCO thin film deposition.

Depending on the substrate and the required properties of the YBCO thin film a set of optimal deposition parameters can be found. The laser fluence E and pulse repetition rate f together with the background oxygen pressure P_d control the dynamics of the plasma plume which will affect the nucleation and growth of the thin film. The distance between the target and the substrate d together with the substrate temperature T_d affect the energetics of the atoms impinging on the substrate. In epitaxial growth the deposited atoms adapt to the crystal lattice of the substrate surface, through diffusion at high temperature, and form crystalline

T_d	P_d	d	E	f	P_{ann}
760 °C	0.6 mbar	55 mm	2 J/cm^2	6 Hz	900 mbar

Table 3.1: Typical deposition parameters used for PLD of YBCO thin films. The parameters are described in the text.

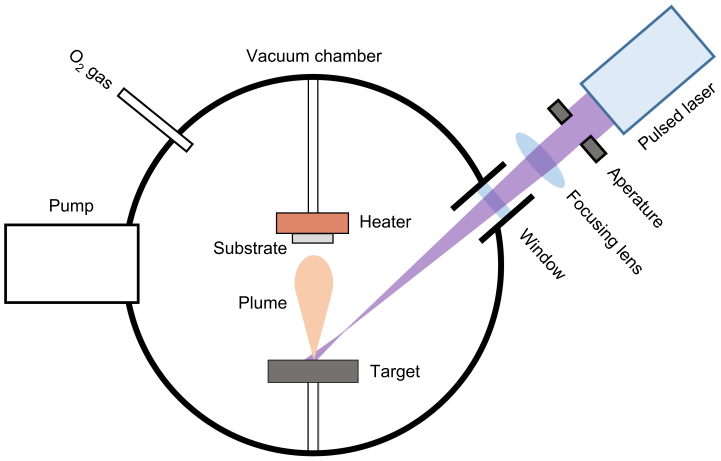

Figure 3.1: Illustration of the pulsed laser deposition system used in this thesis.

grains with a specific orientation. The hole doping is set by the post-annealing oxygen pressure P_{ann} that oxygenates the film after the deposition. P_{ann} is set close to atmospheric pressure in order to get slightly overdoped ($p \approx 0.18$) YBCO with a high T_c [82]. More details on how we grow underdoped films is discussed in section 3.4. In table 3.1 the typical deposition parameters used for YBCO deposition in our PLD system are presented.

3.2 Substrates, strain and twinning

The choice of the substrate is of paramount importance in epitaxial growth as it serves as the template for the thin film growth. To get high quality thin films with a specific crystal orientation one typically uses a substrate with surface lattice parameters that closely match the lattice parameters of the material.

The substrate can also be used to induce a specific strain in the thin film. If the lattice parameters of the substrate and the thin film are slightly mismatched the YBCO unit cell deforms to adapt to the substrate lattice. The strain is relaxed as the thickness of the film increases and the influence of the substrate/film interface to the structural and transport properties diminishes. The thickness dependence of the induced strain can be used to study the properties of the thin film as a function of the strain.

Twinning is another important concept related to the choice of substrate. YBCO as deposited, before the oxygen annealing, grows in the tetragonal phase where the a- and b- axes are equal. The unit cell becomes orthorhombic when the CuO chains are formed and the two axes (a and b) become non-equivalent. If the two in-plane lattice parameters of the substrate are equal there is no preferential direction for the CuO chains to align. In this case the YBCO thin film consists of

crystal grains that are randomly oriented along the two substrate directions. One therefore gets a twinned film. In an untwinned film, the CuO chains (b-axis) are aligned along one of the substrate in-plane directions. Untwinned films enable studies of the properties that break the rotational symmetry, such as a nematic order.

In the following sections we describe the growth of strained and untwinned YBCO thin films on two different substrates: (110)-oriented MgO and (001)-oriented $SrTiO_3$.

Untwinned films on MgO(110)

The majority of the samples in this thesis are grown on (110)-oriented MgO substrates. The motivation mainly comes from the possibility to grow untwinned films with a specific strain, as it will be explained in the following sections.

Structural characterization

Magnesium oxide (MgO) is an ionic crystal with rock salt structure and lattice parameter a_{MgO}=4.212 Å. It is a clean crystal with a thermal expansion coefficient that is close to that of YBCO ($\sim 1 \cdot 10^{-5} K^{-1}$ at 0°C). Since MgO has cubic symmetry, any YBCO film grown on a (001)-oriented surface would be twinned. The (110)-oriented MgO surface instead is rectangular with $[001]_{MgO}$=4.21 Å and $[1\bar{1}0]_{MgO}$=5.96 Å, which in principle allows for the growth of untwinned YBCO.

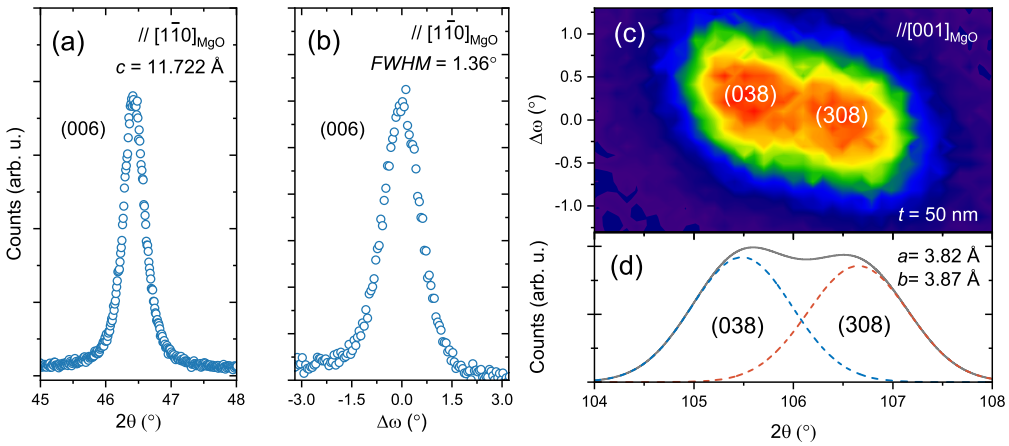

Figure 3.2: XRD structural characterization of a 50 nm thick YBCO film grown on MgO(110). (a) $2\theta - \omega$-scan close to the (006) Bragg reflection. (b) Rocking curve (ω-scan) close to the (006) Bragg reflection. (c) Asymmetric $2\theta - \omega$ map of the YBCO (308)/(038) Bragg reflections. (d) Sum of the $2\theta - \omega$ scans in (c). The dashed lines are Gaussian fits to the total signal (full line) showing the individual contributions of the (308) and (038) reflections to the map.

In figure 3.2 an X-ray diffraction (XRD) characterization of a YBCO thin film grown on MgO(110) is presented. Figures 3.2(a,b) show a symmetric $2\theta - \omega$-scan and the rocking curve ($\Delta\omega$) of the YBCO(006) Bragg reflection respectively. The YBCO c-axis lattice parameter is estimated from the 2θ angular positions of the YBCO $(00L)$ Bragg reflections (only L=6 is shown here). The rocking curve gives information about the mosaicity of the film: the width of the peak depends on the degree of alignment between different crystal grains of the thin film. Here a narrow peak means that the crystal grains are well aligned in the c-axis direction.

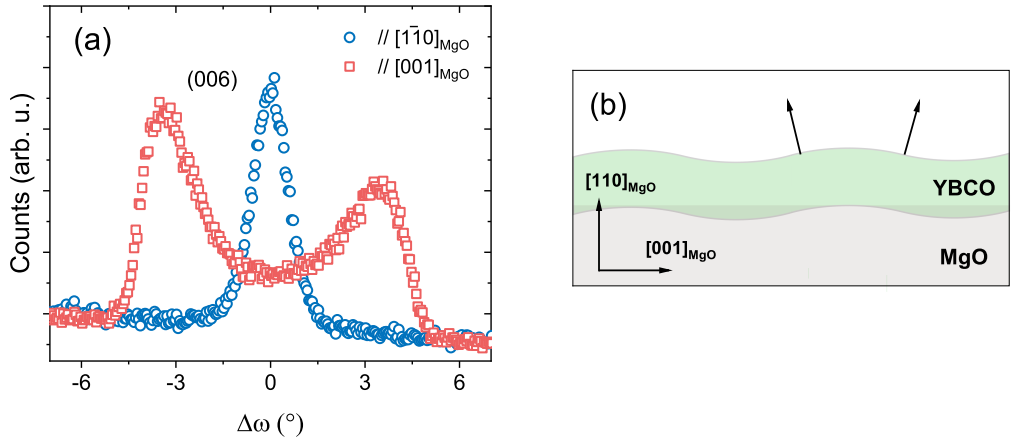

Figure 3.3: Buckling of the YBCO atomic planes in films grown on MgO(110). (a) Rocking curves of the YBCO (006) reflection measured along the two crystal directions of the substrate surface. (b) Illustration of the smooth waving of the YBCO planes compatible with the measurement in (a).

The YBCO in-plane a- and b-axis alignment is investigated with asymmetric $2\theta - \omega$ maps of the YBCO (308) and (038) Bragg reflections. In figure 3.2(c) a (308)/(038) map measured along the $[001]_{MgO}$ direction is shown. The a and b lattice parameters are estimated from the 2θ angles of the (308) and (038) reflections together with the c-axis length. From the lattice parameters (a=3.82 Å, b=3.87 Å, c=11.722 Å) we infer that there is an in-plane compressive strain induced by the substrate. The c-axis is longer and the b-axis shorter than in relaxed crystals [43] while the a-axis is approximately the same length. We will show later on that the situation changes in few nm thick films. Looking at the map in figure 3.2(c) it is clear that the thin film is twinned. The (308) reflection related to the a-axis is of nearly equal intensity as the (038) reflection related to the b-axis, as is also seen in the two-peak fit to the summed intensity in figure 3.2(d). In an untwinned film only one peak should be present when measuring along one in-plane substrate direction. The fact that the film is twinned even though the substrate lattice is asymmetric is most likely because the lattice mismatch is too large for the YBCO film to adapt to the orientation of the substrate lattice.

To accommodate the large lattice mismatch there is instead a unidirectional

buckling of the YBCO atomic planes. The buckling is clearly seen as a splitting of the (00L) Bragg peaks along $[001]_{MgO}$ direction, as shown in the rocking curves of figure 3.3(a). The split is $\approx \pm 3°$ with a non-zero intensity between the two peaks, which indicates a smooth in-plane waving (without grain-boundaries [83]), as illustrated in figure 3.3(b).

Untwinned films

To get untwinned thin films on MgO(110) we induce an additional asymmetry in the substrate by surface reconstruction. It is well known that the (110) surface of crystals with the MgO structure is thermally unstable and thus susceptible to the formation of facets of different crystal orientation [84].

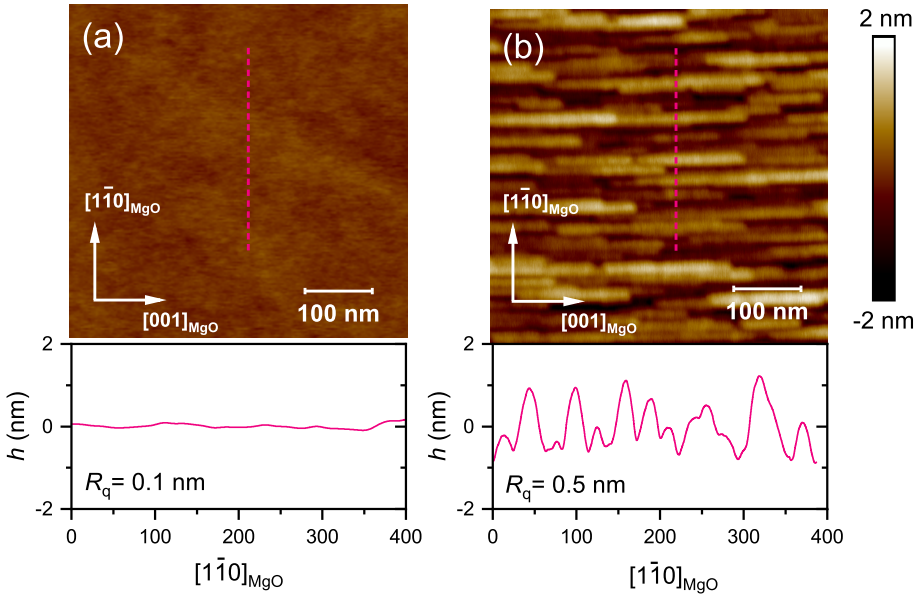

Figure 3.4: AFM images of the surface of a MgO(110) substrate before and after 5 hours of thermal annealing at $T = 790°C$. The pink dashed lines are the cuts for the line profiles of the AFM images below.

To reconstruct the substrate surface we make a thermal annealing at T=790°C and $P = P_d$ before the thin film deposition. Figure 3.4 shows atomic force microscopy (AFM) measurements of a MgO(110) substrate before and after a 5h long thermal annealing. The resulting facets are oriented along $[001]_{MgO}$ with dimensions ≈80x25x1 nm and ≈3.5-7° tilt angle from the surface. The average surface roughness R_q of the substrate increases from 0.1 nm to 0.5 nm because of the surface reconstruction. The buckling of the YBCO planes described in the previous section does not depend on the reconstruction of the substrate surface as it is almost the same on as-delivered substrates.

An XRD structural characterization of a YBCO thin film grown on an annealed

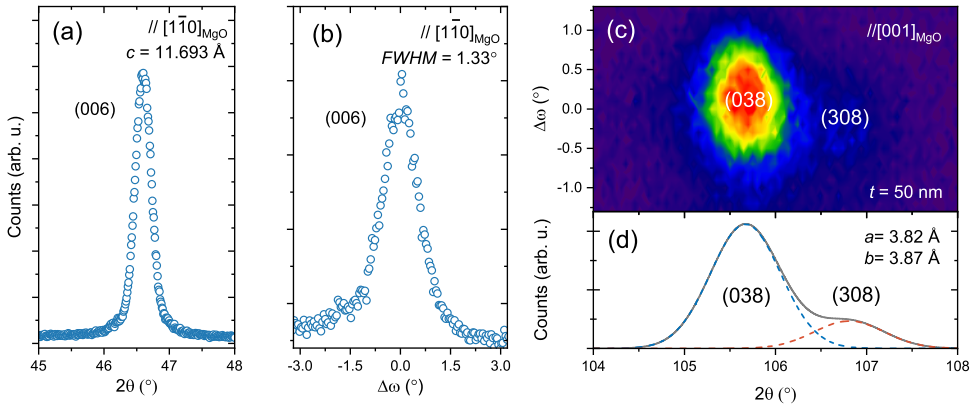

Figure 3.5: XRD structural characterization of a 50 nm thick YBCO film grown on annealed MgO(110). (a) $2\theta - \omega$-scan close to the (006) Bragg reflection. (b) Rocking curve (ω-scan) close to the (006) Bragg reflection. (c) Asymmetric $2\theta - \omega$ map of the YBCO (308)/(038) Bragg reflections. (d) Sum of the $2\theta - \omega$ scans in (c). The dashed lines are Gaussian fits to the total signal (full line) showing the individual contributions of the (308) and (038) reflections to the map. The film is $\approx$ 84 % untwinned.

MgO substrate is presented in figure 3.5. The c-axis is shorter (c = 11.693 Å) compared to the film grown on the flat MgO substrate which indicates that the thin film is slightly less strained. There is however no significant change of the in-plane lattice parameters. The fact that the width of the (006) Bragg reflection in 2θ and $\Delta\omega$ is unchanged tells that the crystalline quality of the thin film is similar, despite the greater roughness of the substrate surface. The (308)/(038) map is however very different. The (308) reflection related to the YBCO a-axis is strongly suppressed along the $[001]_{MgO}$ direction, which means that there is a high

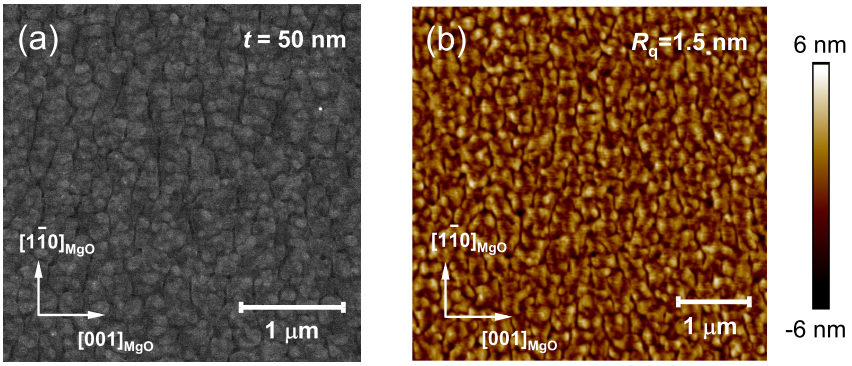

Figure 3.6: Surface characterization of YBCO grown on annealed MgO(110) by (a) SEM and (b) AFM.

degree of untwinning. From the relative intensity of the (308) and (038) peaks (see figure 3.5 (d)) the untwinning degree is estimated to ≈84%.

Surface characterization through scanning electron microscopy (SEM) and AFM shows that the YBCO film surface is smooth with three-dimensional c-axis spiral growth and low density of particles/holes , see figure 3.6. The smoothness of the surface is demonstrated by the low average surface roughness R_q=1.5 nm. There are ≈ 1 nm deep channels preferably oriented along $[110]_{\mathrm{MgO}}$ (or the YBCO a-axis). These channels are not present in films grown on flat MgO(110) substrates and are thus a consequence of the substrate surface reconstruction.

Transport characterization

In a twinned film all macroscopic measurements such as the resistivity give results that are a mixture of the properties of the two in-plane directions and therefore there is no difference in measuring along one or the other direction. In an untwinned film it is instead possible to see the effects of the in-plane anisotropy, such as the conductivity contribution from the b-axis oriented CuO chains or other rotational symmetry breaking phenomena such as nematicity.

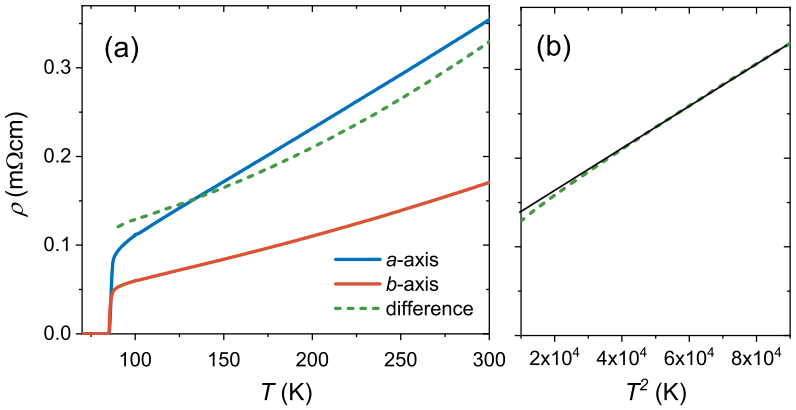

Figure 3.7: Resistivity anisotropy and chain conductivity in a t=50 nm slightly overdoped YBCO film grown on annealed MgO(110). (a) ρ(T) measured along the YBCO a- and b-axis. The dashed green line is the difference in resistivity along the two directions calculated as $1/\rho_{\mathrm{ch}}=1/\rho_{\mathrm{b}}-1/\rho_{\mathrm{a}}$. (b) ρ_{ch} plotted versus T^2. The gray line is a linear fit to the data.

Resistivity versus temperature ($\rho(T)$) measurements along the two in-plane directions of an untwinned, slightly overdoped YBCO thin film is presented in figure 3.7. The measurements are done in a 4-point van der Pauw configuration and the resistivity is calculated according to the relation $\rho = \pi Rt/\ln 2$ where R is the resistance and t the film thickness [85]. The resistivity along the a-axis (ρ_{a}) has the typical linear T dependence of a slightly overdoped cuprate [16]. Along the b-axis the resistivity (ρ_{b}) has a different T-dependence, a consequence of the

CuO chains that contribute to the conductivity [86, 87]. The resistivity of the chains (ρ_{ch}) can be estimated by assuming a parallel conduction to the planes [87] ($1/\rho_{ch}=1/\rho_b-1/\rho_a$) which results is the green dashed line in figure 3.7. The chain resistivity has a T^2 dependence as seen by the linear fit of $\rho_{ch}(T^2)$ in figure 3.7(b). The resistivity anisotropy ρ_a/ρ_b due to the chains at room T (300 K) corresponds well to what has been measured in crystals if one takes the non-perfect untwinning into account [86].

Untwinned films on $SrTiO_3$

$SrTiO_3$ (STO) is a common substrate for YBCO thin film growth. The main reason is the close matching to the YBCO in-plane lattice parameters. STO is a cubic perovskite with the lattice parameter a_{STO}=3.905 Å. YBCO thin films grow with an in-plane tensile strain on STO since a_{STO} is slightly larger than the in-plane lattice parameters of YBCO. In this thesis we mainly use YBCO thin films on (001) oriented STO for comparison to the films grown on MgO. Since the properties of YBCO on STO are more thoroughly studied and the induced strain is tensile (opposite to the compressive strain in films on MgO) the comparison is very useful for finding differences in the properties of the films grown on MgO.

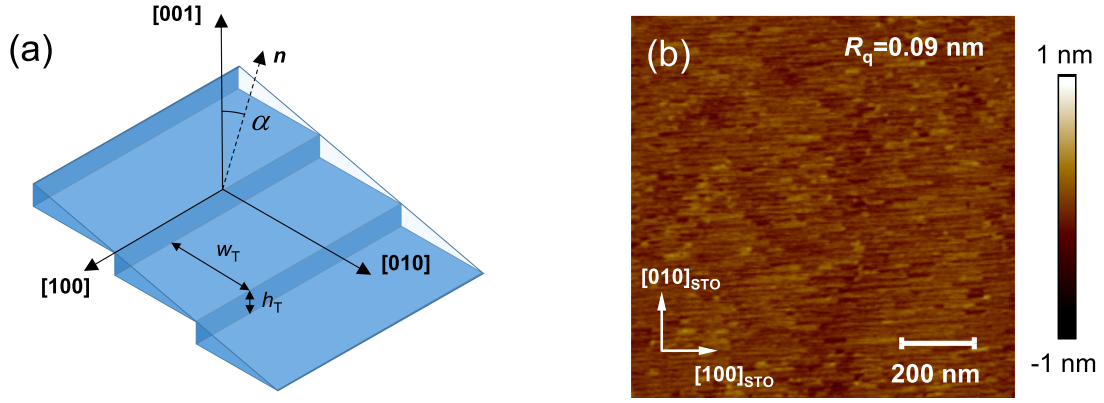

Figure 3.8: Surface of an STO substrate with a vicinal cut. (a) illustration of the step formation on the STO surface following the cut. The height h_T and width w_T of the steps depends on the vicinal angle α, which is defined as the angle between the [001] axis of the substrate and the cut surface normal $\boldsymbol{n}$. Adapted from Ref. [88]. (b) AFM image of the surface of a 1° vicinal angle cut STO substrate.

YBCO thin films grown on STO are normally twinned since STO is cubic. To grow untwinned YBCO films it is common to use a substrate with a vicinal angle cut [89], see figure 3.8. The substrates used in this thesis are cut with a $\alpha = 1°$ tilt angle towards the $[010]_{STO}$ direction. Steps are formed on the substrate surface because of the small-angle cut. The step height h_T is approximately one STO unit cell and they are 10-20 nm wide, as can be seen in the AFM image of figure

3.8(b).

When YBCO thin films are deposited on vicinal cut STO the YBCO *b*-axis tends to align parallel to the step edges ($[100]_{STO}$). This comes from the minimization of the strain energy at the film/substrate interface [88, 90]. To accommodate the YBCO crystal lattice a small compressive strain is imposed on the substrate surface layers. Because of the step formation, that causes a difference in the coordination of the surface atoms, it costs less energy to compress the STO lattice perpendicular to the step edges (along $[010]_{STO}$). The result is that the shorter YBCO *a*-axis preferentially aligns along $[010]_{STO}$ while the longer *b*-axis aligns along $[100]_{STO}$. A similar effect is most likely behind the untwinning of films on reconstructed MgO(110) where the *b*-axis aligns along the $[001]_{MgO}$ oriented facets (see figure 3.4(b)).

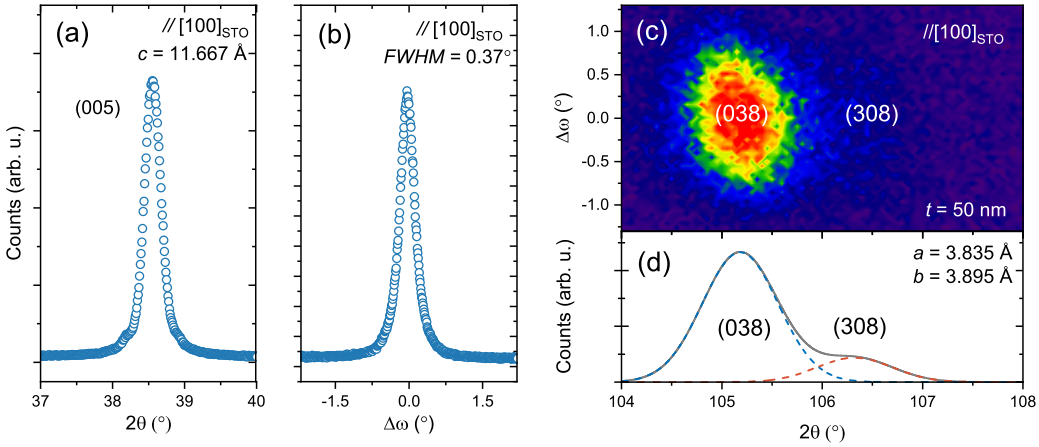

Figure 3.9: XRD structural characterization of a 50 nm thick YBCO film grown on STO with a vicinal angle cut. (a) $2\theta - \omega$-scan close to the (005) Bragg reflection. (b) Rocking curve (ω-scan) close to the (005) Bragg reflection. (c) Asymmetric $2\theta - \omega$ map of the YBCO (308)/(038) Bragg reflections. (d) Sum of the $2\theta - \omega$ scans in (c). The dashed lines are Gaussian fits to the total signal (full line) showing the individual contributions of the (308) and (038) reflections to the map.

XRD measurements of a 50 nm thick YBCO film grown on STO with a vicinal cut is shown in figure 3.9. The YBCO *c*-axis lattice parameter is shorter than in films on MgO (and bulk crystals [43]) as expected from the lattice parameter mismatch of the film and substrate. The compression of the *c*-axis follows from an in-plane tensile strain. The rocking curve shown in figure 3.9(b) is sharper compared to those measured in YBCO films on MgO indicating a more directional crystal growth. The *a*- and *b*-axis lattice parameters extracted from the (308)/(038) Bragg reflections (as shown in figure 3.9(c,d)) are longer compared to those of bulk YBCO. From the (308)/(038) map the untwinning rate is estimated to 87%, a slightly higher number than in the films on MgO. An even higher untwinning rate can be achieved by using STO with a slightly larger vicinal angle

cut ($\approx 1.1°$) [89]. Table 3.2 summarizes the structural parameters of thin films grown on STO and MgO and compares them to those of bulk YBCO crystals. The surface of the YBCO thin films on STO is smooth and characterized by *c*-axis spiral growth (see figure 3.10). Differently from untwinned films on MgO the surface structure is isotropic without directional channels.

	a (Å)	b (Å)	c (Å)	Untwinning rate
MgO(110)	3.82	3.87	11.69	84%
STO(001)	3.84	3.90	11.67	87%
Bulk	3.82	3.89	11.68	-

Table 3.2: Comparison of structural characteristics of 50 nm thick, slightly overdoped, untwinned YBCO thin films on MgO(110), STO(001) and bulk crystals [43].

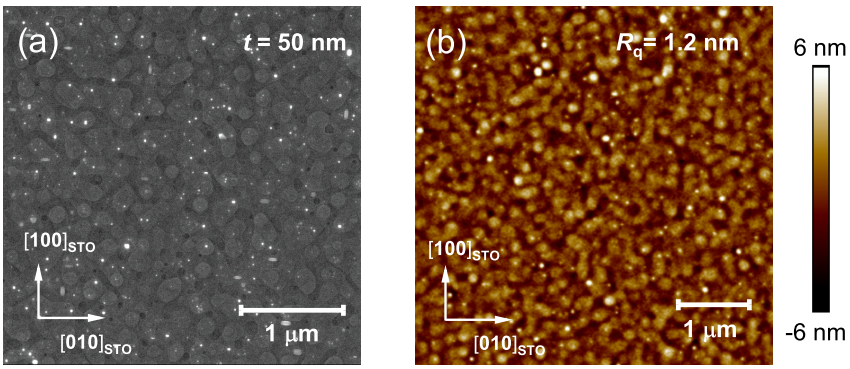

Figure 3.10: Surface characterization of YBCO grown on vicinal angle cut STO by (a) SEM and (b) AFM scanning.

3.3 Few unit cell thick films

There are many reasons for studying the properties of YBCO films as a function of the thickness. In epitaxial growth the strain induced by the substrate is stronger when the film thickness is small. The thin film lattice has to adapt to the substrate close to the interface, which can be used to induce a strong strain. Anisotropic, or uniaxial, strain can be induced by using a substrate with a non-square lattice, such as MgO(110). Another motivation is that the system becomes more two-dimensional (2D) when the film thickness is just a few unit cells which is interesting both for fundamental studies of the material [91, 92] and for devices such as single photon detectors [93, 94]. The growth of few unit cell thick films is challenging since defects will have a larger impact on the transport properties and it is thus even more important that the thin film is smooth and crystalline. In this section

we present the characterization of 10 nm thick slightly overdoped YBCO films grown on annealed MgO(110).

Structural characterization

The XRD structural characterization of a 10 nm thick film is presented in figure 3.11. Compared to the 50 nm thick films the (006) Bragg reflection is shifted to a lower 2θ value which means an increase of the c-axis length. The increase is most likely a consequence of the stronger strain induced by the substrate. There is also a clear increase of the width of the Bragg peak that possibly comes from a combination of smaller film thickness and the larger strain. Looking at the rocking curve, the FWHM is unchanged with respect to the thicker film. This indicates that the crystal quality of the 10 nm thick film is equally high as in the 50 nm thick film. There is a clear shift of the (038) Bragg reflection to a lower 2θ value, as seen in the map of figure 3.11(c). Consequently, there is an extension of the b-axis lattice parameter to $b = 3.89$ Å (from b= 3.87 Å in the 50 nm thick film). Since the Bragg reflections are very weak it is difficult to estimate the twinning rate of the 10 nm thick films. The (308) reflection is not discernible in the map, and we only fit one peak in figure 3.11(d).

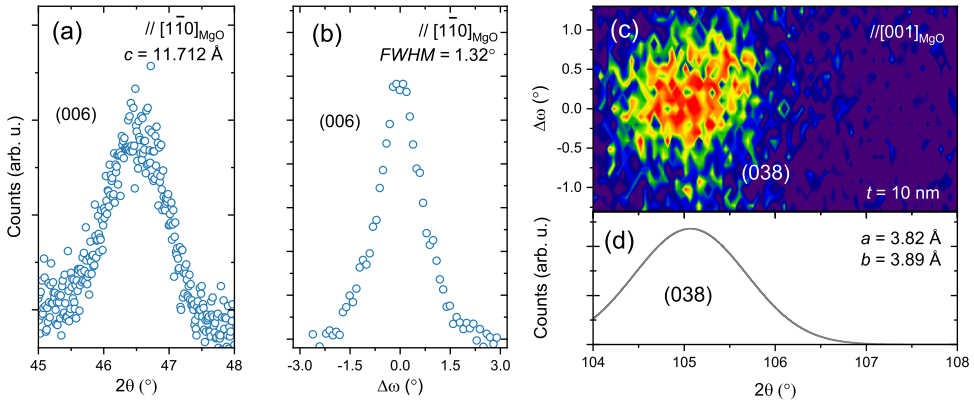

Figure 3.11: XRD structural characterization of a 10 nm thick YBCO film grown on reconstructed MgO(110) (a) $2\theta - \omega$-scan close to the (006) Bragg reflection. (b) Rocking curve (ω-scan) close to the (006) Bragg reflection. (c) Asymmetric $2\theta - \omega$ map of the YBCO (308)/(038) Bragg reflections. (d) Sum of the $2\theta - \omega$ scans in (c).

There is however no significant change, compared to 50 nm thick films, of the a-axis lattice parameter extracted from the map of the (308) reflection measured along the perpendicular $[1\bar{1}0]_{MgO}$ direction. Table 3.3 shows a comparison of the extracted lattice parameters in the 10 and 50 nm thick films on MgO(110). The increase of both the b- and c-axis in the 10 nm thick films thus leads to an increase of the unit cell volume. The origin and consequences of this peculiar

strain in slightly overdoped thin films will be the object of further studies.

Similarly to the 50 nm thick films the surface is smooth and characterized by c-axis growth spirals, see figure 3.12. The channels oriented in the a-axis direction are less pronounced than in thicker films. In some cases they are absent. There are shallow holes (mainly around the channels) that are clearly visible as bright spots in the SEM image indicating a lower conductivity. From the AFM measurement the film surface is flat with even smaller roughness than the thicker films.

t (nm)	a (Å)	b (Å)	c (Å)	T_c^{on} (K)	ΔT_c (K)	ρ_a/ρ_b @ 300 K
50	3.82	3.87	11.693	87.4	1.3	2.1
10	3.82	3.89	11.712	85.7	3.9	3.2

Table 3.3: Comparison of structural and superconducting characteristics of 50 and 10 nm thick, slightly overdoped, untwinned YBCO thin films on reconstructed MgO(110).

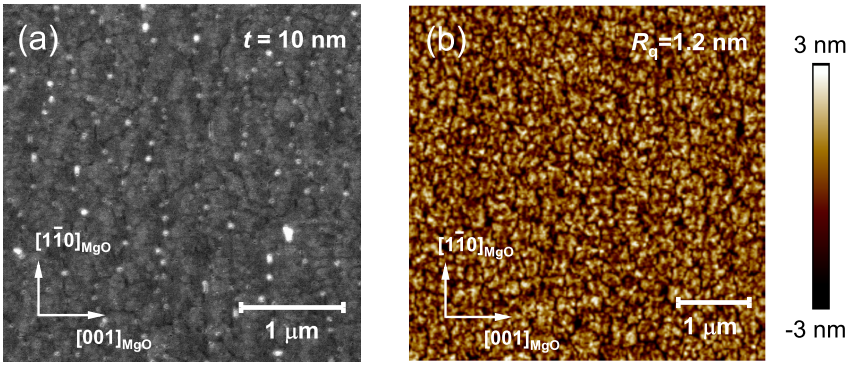

Figure 3.12: Surface characterization of YBCO grown on annealed MgO(110) by (a) SEM and (b) AFM scanning.

Transport characterization

The small film thickness also affects the electrical transport properties, both in the superconducting and normal state. As the film thickness decreases the superconducting resistive transition is broadened [94–96]. In a perfectly ordered bulk superconductor the resistive transition can be extremely narrow in temperature. In thin films the broadening of the transition can come from two different effects: two-dimensional transport and disorder. There is always a finite broadening in 2D superconductors due to vortex-antivortex pair dissociation (Kosterlitz-Thouless transition) [97]. The 2D effects become more evident as the number of unit cells approach unity. Disorder-induced broadening of the transition can either be structural, for example from inhomogeneous doping that gives a range of T_c values in

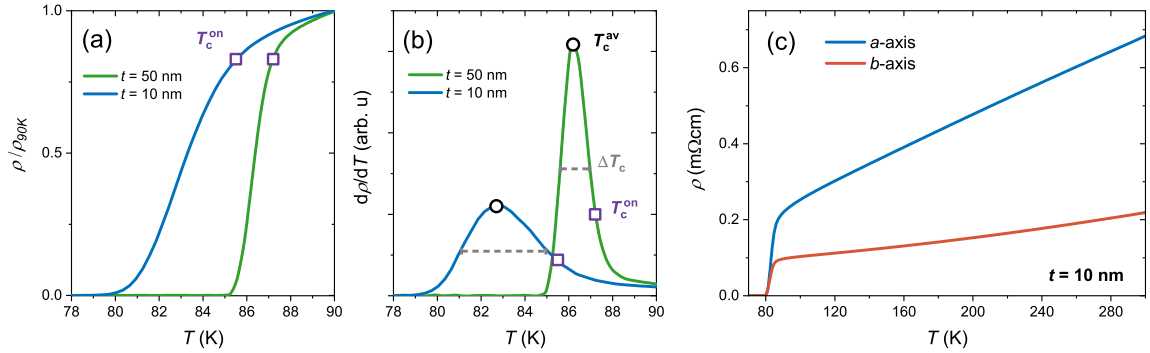

Figure 3.13: $\rho(T)$ of 10 nm thick slightly overdoped YBCO films on annealed MgO. (a) Comparison of the superconducting resistive transition in 10 and 50 nm thick films. (b) Temperature derivative of the resistive transitions in (a). The values of T_c^{on}, T_c^{av} and ΔT_c are shown for both films (see table 3.3 for the numbers). (c) Resistivity anisotropy of a 10 nm thick film.

the film, or electronic, for example from competing CDW order, which will be further discussed in chapter 7. A comparison between the resistive transition in 10 and 50 nm thick films is shown in figure 3.13(a) where the broader transition of the 10 nm thick film is evident. To quantify the broadening we use ΔT_c, which is defined as the FWHM of the peak in $d\rho(T)/dT$ at the transition, see the dashed gray lines of 3.13(b). Because of the broadening we use the onset of the resistive transition T_c^{on} to define the superconducting critical temperature when comparing thick and thin films. T_c^{on} is defined at 90% of the normal state resistance R_N above the transition. Other common definitions of T_c includes T_c^{av}, which is in the centre of the transition and taken at the maximum of $d\rho(T)/dT$ (see black circles in figure 3.13(b)), and the zero resistance temperature T_c^0. We do not expect T_c^{on} to be significantly different in films with the same doping but different thickness, while T_c^{av} and T_c^0 can significantly vary because of the broader transition in very thin films. As seen in figure 3.13(b) the difference in T_c^0 and T_c^{av} of the 10 and 50 nm thick films is greater than the difference in T_c^{on}. The small difference of T_c^{on} ($\approx$1.7 K) could however be related to a difference in doping [94]. The lower T_c^{on} of the 10 nm thick film translates to a higher doping, since we are on the overdoped side of the phase diagram where the T_c decreases with increased doping. A possible reason for the higher doping is that the 10 nm thick film is easier to oxygenate during the post annealing process of the film deposition. In figure 3.13(c) the $\rho(T)$ measurements along the a- and b-axis of a 10 nm thick slightly overdoped YBCO film are shown. Just like in the thicker films (figure 3.7) the CuO chains along the b-axis cause anisotropic resistivity along the two in-plane orientations. The resistivity anisotropy is however greater in the 10 nm thick films (see table 3.3). The excess resistivity anisotropy will be further discussed in chapter 6.

3.4 Underdoped films

Up to this point we have only discussed the properties of slightly overdoped YBCO thin films. To study the interplay between different electronic orders which characterize the phase diagram, one needs to be able to grow thin films at different doping levels. It is not possible to dope YBCO above $p \approx 0.19$ with oxygen ($\delta = 0$). Higher doping levels can instead be reached by replacing yttrium with calcium [98]. The doping of the film is reduced by introducing oxygen vacancies in the CuO chains, as described in section 2.2. Growing underdoped films is however very challenging. In most reports, on underdoped YBCO thin films, the doping dependence of T_c is quite different from what is found in pristine single crystals [99, 100]. The main reason is probably inhomogeneous oxygen (doping) distribution in the films. To properly study the YBCO phase diagram it is crucial to have films with homogeneous doping that reproduce the properties of single crystals.

As mentioned in section 3.1 the doping of the thin films is controlled by the post-annealing oxygen pressure P_{ann}. We get films with doping levels covering a major part of the phase diagram from slightly overdoped ($T_c \approx 86$ K) down to strongly underdoped ($T_c = 0$ K) by reducing P_{ann} from 9×10^2 to 1×10^{-5} mbar. The pressure is very stable ($\leq 2 \times 10^{-6}$ mbar) and set by pumping on a continuous flow of oxygen gas. A stable pressure is crucial for reproducible films and for a uniform doping distribution.

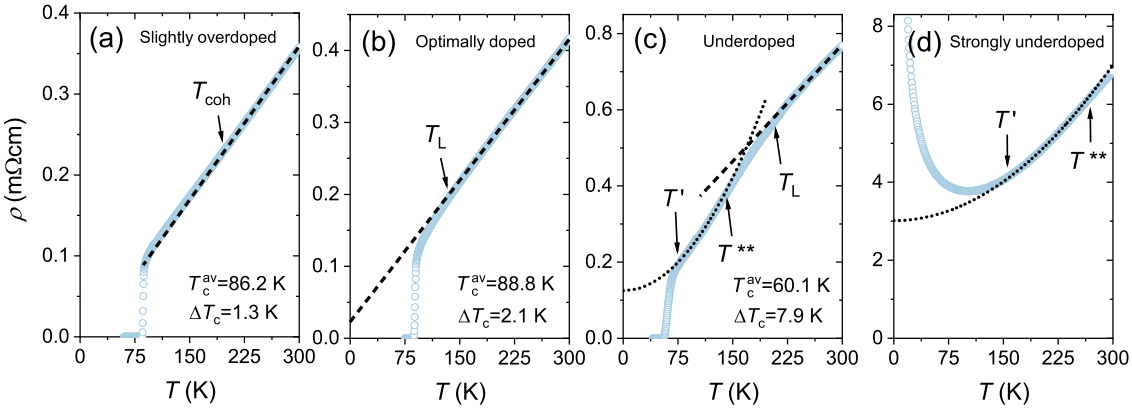

Figure 3.14: Typical $\rho(T)$ of YBCO at different doping levels (a) Slightly overdoped, (b) Optimally doped, (c) Underdoped, (d) Strongly underdoped/undoped. The different characteristic temperatures that can be extracted from the shape of the $\rho(T)$ are pointed out. See the text for a description of each characteristic temperature.

In addition to T_c, there are other characteristic temperatures that can be extracted from the shape of the $\rho(T)$. In figure 3.14 typical $\rho(T)$ measured in YBCO films with different doping regimes is shown together with the characteristic temperatures which are described below:

- In the slightly overdoped regime ($p \approx 0.18$) $\rho(T)$ is linear down to what is

known as the coherence temperature T_{coh} where $\rho(T)$ increases faster with lower temperature [101] (figure 3.14(a)). T_{coh} is usually associated to the end of the strange metal regime on the overdoped side and to the recovery of the quasiparticle picture of the excitations [50] (see section 2.2).

- In the optimally doped regime ($p \approx 0.16$), $\rho(T)$ is linear in a wide temperature range down to T_{L}, where $\rho(T)$ decreases faster with lower temperature. T_{L} is commonly associated to the end of the strange metal regime on the underdoped side, and its value is close to the pseudogap temperature T^*.
- In the underdoped regime ($p \approx 0.08-0.16$), the range of linear $\rho(T)$ is smaller (T_{L} increases with decreasing p). In addition, $\rho(T)$ is quadratic below T^{**}. The T^2 dependence of $\rho(T)$ is sometimes seen as a recovery of Fermi liquid like transport in the underdoped regime. T^{**} has also been associated to the onset of electronic nematicity below $p \approx 0.11$ [102]. The quadratic T dependence ends at T'. In the underdoped regime T' is related to the onset of superconducting fluctuations slightly above T_{c}.
- In the strongly underdoped regime ($p \approx 0.04$) the range of quadratic $\rho(T)$ shifts to higher temperatures. Differently from the less underdoped case T' is associated to a metal/insulator transition, since $\rho(T)$ strongly increases below T'. The insulating behavior is thought to be related to the antiferromagnetic state at zero doping [103, 104].

Another trend that can be seen from the doping dependence of the resistivity in figure 3.14 is that both ρ_0 (the resistivity extrapolated to $T = 0K$ from the linear or quadratic fit at high T) and the width of the resistive transition ΔT_{c} (defined in section 3.3) increases with decreasing doping. A similar trend is seen in bulk single crystals [14, 41]. It is not believed to be strictly related to increased disorder, but is an intrinsic property of the cuprates, possibly related to the electronic orders developing in the underdoped regime [72, 86].

Structural characterization

There are significant changes of the structural parameters of the thin films when decreasing the doping. Figure 3.15 shows the XRD characterization of YBCO thin films of different doping levels. When the doping decreases, the $(00L)$ Bragg reflections are shifted to lower 2θ values, as expected from an expansion of the c-axis lattice parameter. The expansion is a consequence of the lower oxygen content in the CuO chain layers which has a cohesive effect on the YBCO unit cell [43]. The fact that the width of the Bragg peaks, in both 2θ and $\Delta\omega$, does not depend on the doping (see figure 3.15) tells that the structural quality of the films is similar, independently of the doping. This can indicate that the increase of the resistivity and ΔT_{c} in the underdoped films is not due to inhomogeneous doping but is an intrinsic property of the material.

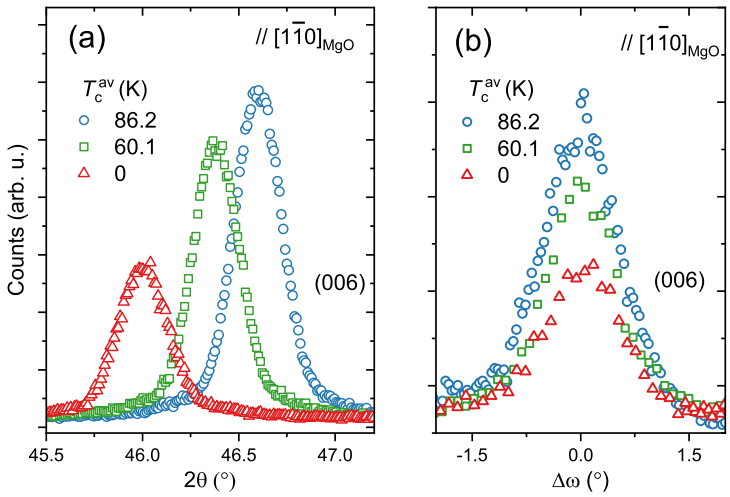

Figure 3.15: XRD structural characterization of 50 nm thick YBCO films of different doping levels grown on 5h annealed MgO(110) (a) $2\theta-\omega$-scan close to the (006) Bragg reflection. (b) Rocking curve (ω-scan) close to the (006) Bragg reflection.

Determination of the hole doping

To properly construct the phase diagram for our thin films we need a way of determining the hole doping. As described in chapter 2.2, the doping is set by the amount of oxygen in the CuO chains. In single crystals weighing methods are often used to determine the oxygen content $(7-\delta)$ which then can be translated to p, the number of holes per planar copper atom. Measurements of the Hall coefficient R_H is commonly used to determine the carrier concentration in other materials, but R_H is strongly temperature dependent in the cuprates (see chapter 7) which makes the interpretation difficult [105, 106]. As these methods does not work on YBCO thin films we need a different way of determining p [17]. A common approach to estimate p is to use the empirical parabolic relationship:

$$1 - T_c/T_c^{max} = 82.6 \cdot (p - 0.16)^2 \tag{3.1}$$

where T_c^{max} is the T_c at optimal doping ($p = 0.16$). However, this equation is not valid around $p = 1/8$ where T_c is lower than expected, presumably because of competition between superconductivity and CDW (as described in section 2.2). It also does not work for $0 < p < 0.05$ where T_c=0. Instead one can use the c-axis lattice parameter to estimate the doping level in thin films. Since c increases monotonically with decreasing p, a unique relationship can be established between the two [17]. First, we use equation 3.1 to estimate p from T_c extracted from the $\rho(T)$. Then, we plot the estimated p versus the c-axis length as extracted from XRD measurements and make a polynomial fit[1] to the data for $p < 0.09$ and

[1] The fit is phenomenological and is based on the assumption that the relationship between p

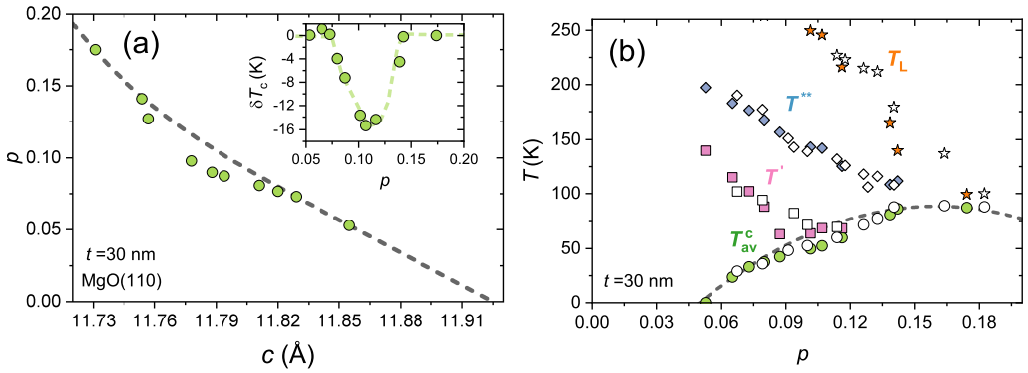

Figure 3.16: Determination of the doping of 30 nm thick YBCO thin films and construction of the phase diagram. (a) hole doping p (extracted from equation 3.1) versus c. The dashed gray line is a fit to the data for $p < 0.09$ and $p > 0.14$. The inset shows the difference between the measured T_c and equation 3.1. (b) Phase diagram for YBCO thin films on MgO(110) (filled symbols) and STO (open symbols). The characteristic temperatures T_L, T^{**}, T' and T_c^{av} are described in the text. The gray dashed line is the empirical parabolic $T_c(p)$ in equation 3.1.

$p > 0.14$ where equation 3.1 is valid. Figure 3.16(a) shows the $p(c)$ fit for 30 nm thick YBCO films on 1h annealed MgO(110). The gray dashed line corresponds to $p = 9y + 1.5 \cdot 10^9 y^6$ where $y = 1 - c/c_0$ and c_0=11.925 Å (the c-axis lattice parameter at p=0). The fit is then used to estimate p from the measured c at all doping levels (including close to 1/8). The parameters of the $p(c)$ fit will be different in single crystals and thin films on different substrates since c depends on the strain [17].

After determining the doping for each film we can construct a simple phase diagram with the characteristic temperatures extracted from the $\rho(T)$ as described above. The result for 30 nm thick films on MgO(110) and STO(001) is presented in figure 3.16(b). The doping dependence of all the characteristic temperatures are in qualitative agreement with those measured in single crystals [16, 27, 107]. T_L increases linearly with decreasing doping and is close to T^*, the pseudogap temperature. T^{**} also increases linearly while T' follows T_c down to $p \approx 0.09$ and increases quickly below this doping level. Regarding T_c, we observe a deviation from the parabolic doping dependence in the underdoped regime around $p \approx 0.125$, independently on the kind of substrate. The suppression is better visualized in the inset of figure 3.16(a), which shows that the largest suppression is $\delta T_c \approx 16$ K at $p \approx 0.11$. Since the strain is very different in the thin films on MgO and STO it seems like strain does not play a large role for the T_c suppression. A possible reason is that the CDW order is of similar strength in the films on both substrates, as will be discussed in chapter 5. Later on we will show that the situation is radically different in 10 nm thick films.

and c is smooth. This has been shown to be true by calculations [17].

The fact that we can reproduce the phase diagram of single crystals in our thin films indicates that the physics of the cuprates is preserved and that the quality of the thin films is good enough to study the intrinsic properties of cuprates.

10 nm thick underdoped films

In section 3.3 we showed that the strain in slightly overdoped thin films changes when decreasing the thickness t. The same is true for underdoped thin films. Figure 3.17(a-c) shows $2\theta - \omega$ measurements of the YBCO (006) and (038) Bragg reflections in underdoped films ($p \approx 0.125$) of varying t. In contrast to the slightly overdoped case, the c-axis lattice parameter decreases in the thin films. However, the a- and b-axis lattice parameters evolve with thickness in a similar way as in the slightly overdoped films, see figure 3.17(d). The increase of the b-axis length seems to be a general feature of very thin films on MgO(110). The increased strain and orthorhombicity in the 10 nm thick films has implications for both the transport and charge order, as will be discussed in chapters 5-7.

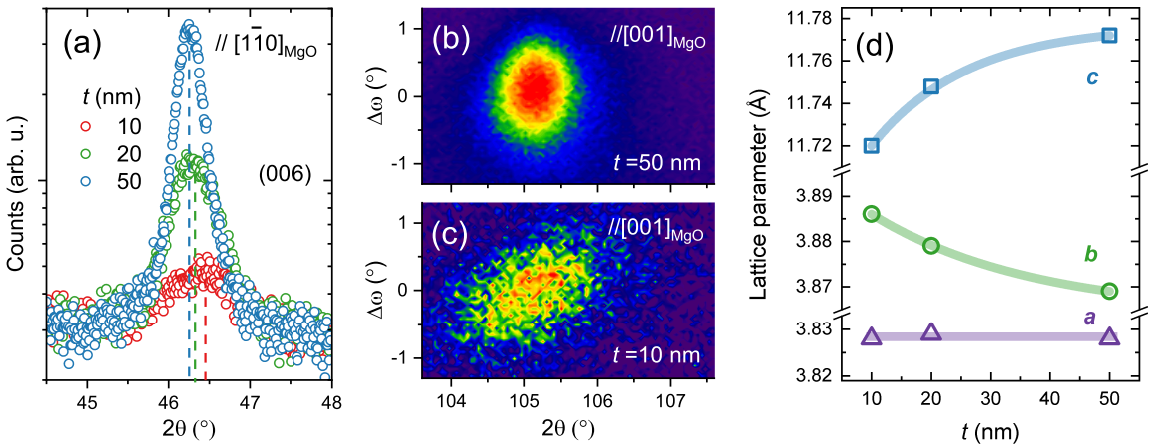

Figure 3.17: XRD structural characterization of underdoped ($p \approx 0.125$) YBCO films of different thickness grown on 5h annealed MgO(110) (a) $2\theta - \omega$-scan close to the (006) Bragg reflection. (b),(c) Asymmetric $2\theta - \omega$ maps of the YBCO (038) Bragg reflection in a 50 nm and 10 nm thick YBCO film respectively. (d) Thickness dependence of the extracted a,b and c lattice parameters.

Figure 3.18 shows the evolution of the YBCO (006) Bragg reflection with doping in 10 nm thick films. As shown in section 3.3, the peaks are much broader than in the thicker films, but the width in 2θ does not change with doping. The same applies to the rocking curves in figure 3.18(b), which again proves that the crystalline quality of our films is equally high in the strongly underdoped regime.

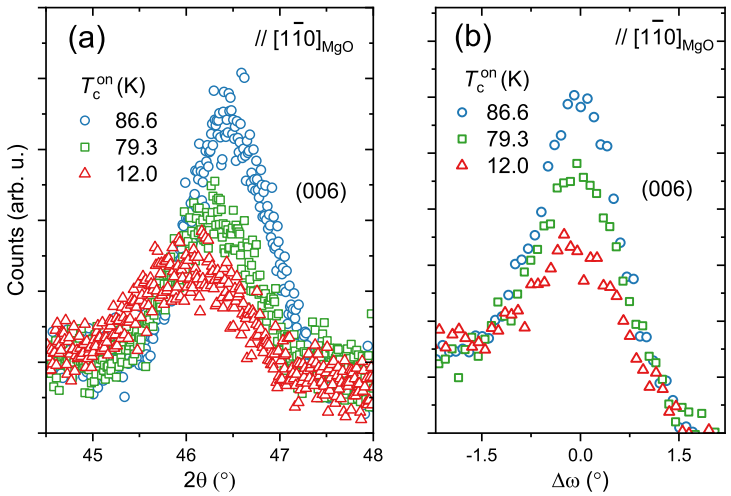

Figure 3.18: XRD structural characterization of 10 nm thick YBCO films of different doping levels grown on 5h annealed MgO(110) (a) $2\theta-\omega$-scan close to the (006) Bragg reflection. (b) Rocking curve (ω-scan) close to the (006) Bragg reflection.

4 Fabrication of underdoped $YBa_2Cu_3O_{7-\delta}$ nanowires

One of the key questions of the physics of HTS is to understand how nanoscale orders affect the properties of devices. The answer can be obtained by the fabrication of nanostructures with properties close to the bulk material. It is very challenging to pattern YBCO down to the nanoscale without negatively affecting the normal and superconducting properties [28, 108–110], mainly because of the chemical instability of the material and sensitivity to defects related to the small superconducting coherence length ξ. This is even more dramatic for underdoped nanowires where oxygen out-diffusion may easily bring the nanostructures to an insulating state. In this chapter we describe a strategy to overcome these problems and to realize pristine nanowires from underdoped thin films. These systems are desirable for applications such as single photon detectors, which will be discussed in chapter 8.

4.1 Nanowire fabrication process

One of the most common and successful methods to fabricate YBCO nanostructures is by electron beam lithography using a hard mask combined with argon ion milling. This method has been used and improved by our group at Chalmers in the past decade to fabricate slightly overdoped YBCO nanowires with cross-sections down to $\approx$ 50x50 nm showing a record high critical current density J_c [111–114]. The steps of the fabrication process (see figure 4.1) are the following:

1. **Deposition of a carbon hard mask**
   An amorphous carbon film is deposited by PLD. The advantage of using hard amorphous carbon lies in the low ion milling rate which allows to get nanostructures with sharp edges.

2. **Electron beam lithography**
   A double layer of positive resist is spin coated on top of the carbon film. The pattern is defined by exposure to a 100 kV electron beam followed by resist development.

3. **Chromium mask lift-off**
   A 10 nm thick chromium film is deposited on the carbon/resist by electron beam evaporation. The negative of the resist pattern is transferred to the chromium by lift-off.

4. **Oxygen plasma etching of the carbon mask**
   The carbon film that is not covered by chromium is removed by oxygen plasma etching.

5. **Argon ion milling of the YBCO thin film**
   The YBCO thin film that is not covered by carbon/chromium is etched by argon ion milling. To minimize the damage to the patterned structures the parameters (acceleration voltage, beam current) have been optimized to values close to the threshold for etching. During this step the chromium mask and some of the carbon mask is also etched.

6. **Oxygen plasma etching of the remaining carbon**
   In the final step the remaining carbon is removed from the top of the patterned YBCO structures by oxygen plasma etching.

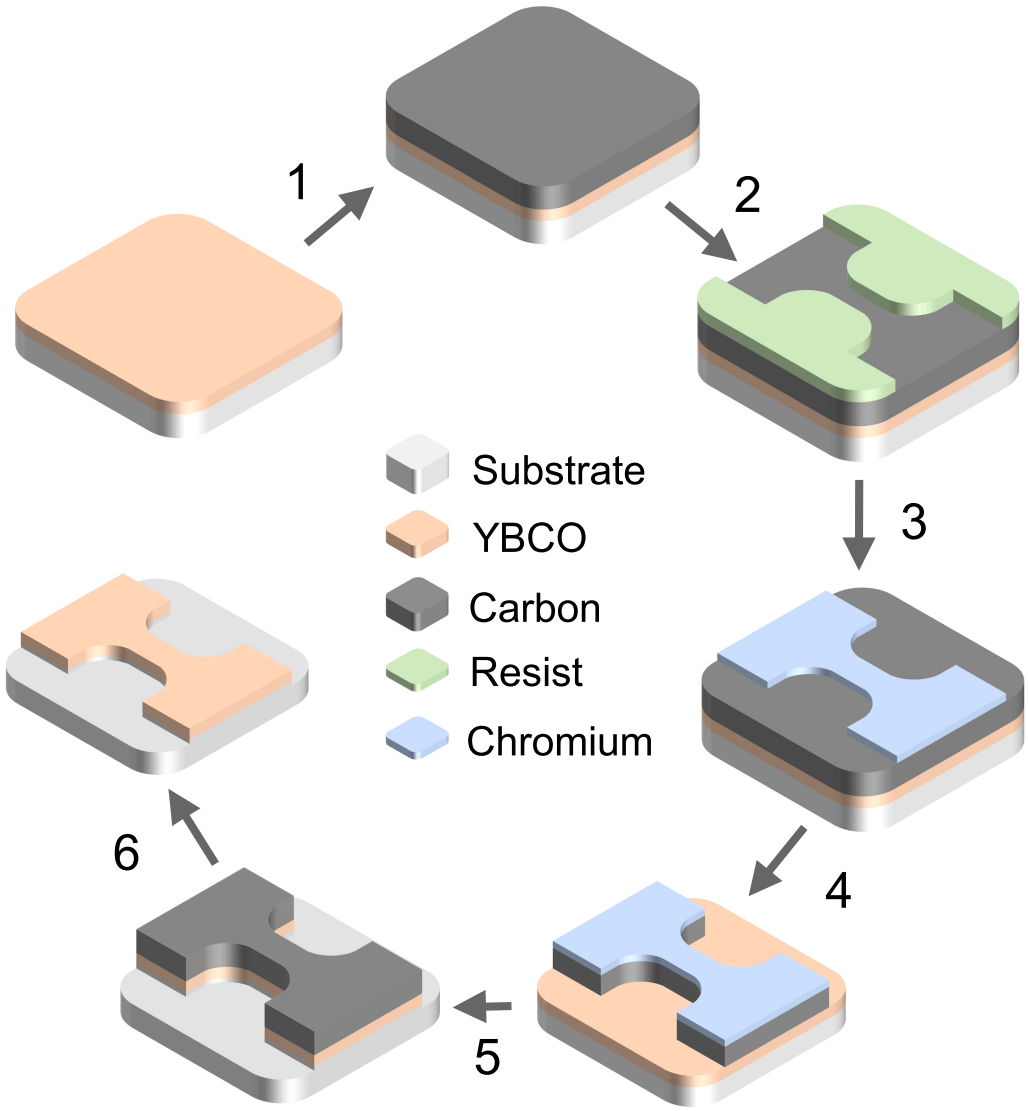

Figure 4.1: Illustration of the fabrication process of YBCO nanowires from thin films. The different fabrication steps are described in the text.

To minimize the damage to the nanostructures in the fabrication process described above, the YBCO thin film is usually capped by a 50 nm thick gold layer deposited on top of the film before the carbon layer [111] (step 1 in figure 4.1). The Au capping helps to protect the YBCO nanostructures during the fabrication in mainly two ways. First, the high thermal conductivity of gold compared to the amorphous carbon helps to mitigate the heat generated during the argon ion milling (step 5 in figure 4.1). Local overheating is a problem for YBCO nanostructures since elevated temperatures cause oxygen out-diffusion and thus reduce the doping level of the nanostructures. Second, the capping protects the surface of the nanowire during the oxygen plasma etching (step 6 of figure 4.1). The Au capping is however an issue if the goal is to study not only the superconducting properties of the nanowires but also the normal state properties. In the normal state it acts as a shunt. A solution to this problem is to remove the gold capping after the fabrication process, but this may also cause damage to the nanowire [113]. It is possible to fabricate high quality, slightly overdoped nanowires without the gold capping, but underdoped nanowires are heavily damaged and show very broad resistive transitions, if any [28, 108].

To fabricate underdoped nanowires without Au capping with transport properties close to the as-grown thin film we have improved the most critical fabrication steps described in figure 4.1. To reduce the local heating of the nanostructures during the ion milling (step 5) we use a cold stage with liquid nitrogen (LN2) cooling, and to reduce the surface damage during the oxygen plasma etching of the carbon (step 6) we use very low power (15 W), the minimum required to generate a stable oxygen plasma.

4.2 Electric transport characterization

Figure 4.2(b) shows a comparison of the normalized resistance close to the superconducting transition of w=200 nm wide, underdoped nanowires fabricated with (circles) and without (diamonds) the improved fabrication process described above. The underdoped nanowire that was etched using a water cooled stage shows no hint of superconductivity at the expected T_c, while the nanowire that was etched using the LN2 cooled stage shows a single resistive transition. This result demonstrates the severity of the damage done by local heating on underdoped nanowires when they are not cooled to cryogenic temperatures. In figure 4.2(c) we compare the resistive transition of a 200 nm wide nanowire to that of a 15 μm wide microbar patterned on the same film. Since there is no significant difference in the T_c^{on} or the width of the transitions we conclude that the doping level of the nanowire is the same as in the parent thin film. To further evaluate if the properties of the underdoped nanowires represent the bulk material we extract the characteristic temperatures in the same way as for underdoped thin films in section 3.4. The geometry of the nanowires is shown in figure 4.2(a) with two 50

nm wide voltage leads connected to the wire to estimate the magnitude of the resistivity through $\rho = R \cdot w \cdot t/l$ where l is the distance between the voltage leads. Figure 4.2(d) shows the $\rho(T)$ measurement of a t= 50 nm underdoped nanowire up to room temperature. Both the magnitude of ρ and ρ_0 together with the characteristic temperatures T_L, T^{**} and T' are comparable to the values found for thin films of equal doping. Summarizing, the measurements presented in figure 4.2 show that there are no significant changes of the resistivity in bare, underdoped nanowires compared to the parent thin film. This is a strong indication that the structure, and thus the doping, is not affected by the fabrication process which means that we can safely use the patterned nanostructures to study the YBCO phase diagram at low dimensionality.

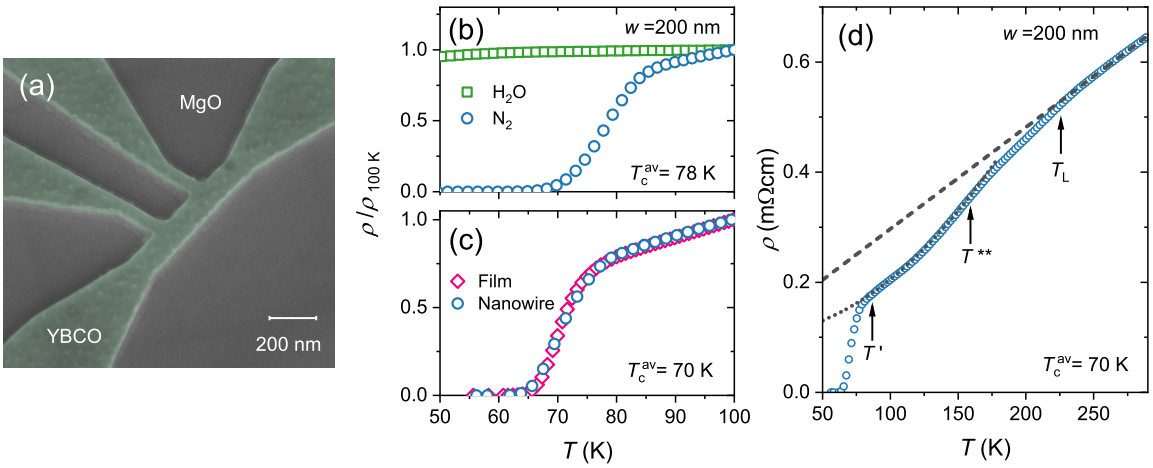

Figure 4.2: . Resistivity measurements of t=50 nm underdoped, uncapped YBCO nanowires. (a) False color SEM image of a 200 nm wide nanowire. (b) Comparison of the resistive transition in nanowires that were etched with argon ion milling while cooled with water and liquid nitrogen. (c) Comparison of the resistive transition in an underdoped thin film and a patterned 200 nm wide nanowire on the same sample. (d) $\rho(T)$ with arrows showing the characteristic temperatures T_L, T^{**} and T' of a 200 nm wide nanowire.

5 Characterization of CDW order in $YBa_2Cu_3O_{7-\delta}$ thin films

In the previous chapters we showed how part of the YBCO phase diagram can be constructed by resistivity measurements in underdoped thin films and nanowires. The charge density wave order, which occupies a significant portion of the underdoped side of phase diagram (see figure 2.3) does however not have a clear signature in the resistivity of the cuprates. Instead, one has to use other techniques to characterize the CDW. As introduced in section 2.2 the signature of the CDW order is a modulation of the charge density in the CuO_2 planes. The periodic modulation of charge in cuprates has been visualized by several different techniques such as scanning tunneling microscopy (STM) [115], nuclear magnetic resonance spectroscopy (NMR) [116] and X-ray scattering techniques [10, 15]. STM measurements are complicated by the non-perfect stoichiometry and roughness of the surface for YBCO. Indeed, YBCO crystals cannot be exfoliated like BSCCO so spectroscpic measurements are very limited. Moreover, for thin films (which are the subject of this thesis) NMR investigations are not feasible because of the limited material volume. X-ray scattering is therefore the preferred technique to study the CDW order.

In this chapter we describe the characterization of the CDW order by resonant inelastic X-ray scattering (RIXS) in untwinned YBCO thin films of different thickness on MgO and STO. We start by introducing the RIXS technique and how it is used for CDW characterization and then present the results of the measurements.

5.1 Resonant inelastic X-ray scattering

RIXS is a synchrotron based spectroscopic technique used to study low energy excitations (e.g. charge, spin or lattice) of strongly correlated materials [117]. When an X-ray photon scatters from a material, the energy and momentum of the scattered photon is not always the same as that of the incoming photon. By measuring the energy and momentum transferred to the material one gains information about the excitations that occurred as a result of the scattering event. There are several advantages with RIXS compared to other scattering techniques (e.g. neutron scattering). RIXS is a resonant technique, which means the energy of the photons is tuned to a specific absorption edge of an element of the material. The resonant character of the scattering gives chemical and atomic site selectivity.

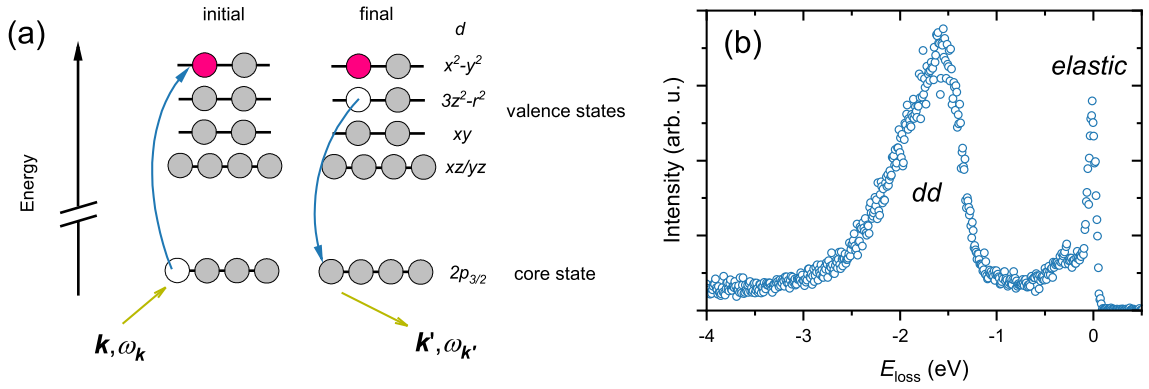

Figure 5.1: (a) Typical RIXS process and (b) RIXS spectra at the Cu L_3 edge for the cuprates.

It is thus possible to specifically study the excitations in the CuO_2 planes of YBCO (by a careful choice of the photon energy). Furthermore, because of the relatively strong interaction between light and matter and the large flux of photons available in a synchrotron, RIXS does not require large sample volumes. In the soft X-ray regime the penetration depth is in the order of 100 nm [117] which is perfectly compatible with thin film measurements.

Figure 5.1(a) shows an illustration of a typical RIXS process for the cuprates. Initially, an X-ray photon of energy $\omega_{\boldsymbol{k}}$ and momentum $\boldsymbol{k}$ impinges on the sample. $\omega_{\boldsymbol{k}}$ is tuned to the Cu L_3 edge (∼931 eV) which translates into a resonant absorption by the excitation of a core electron from $2p_{3/2}$ to a valence $d_{x^2-y^2}$ state. The excited state rapidly decays by the emission of an X-ray photon of energy $\omega_{\boldsymbol{k}'}$ and momentum $\boldsymbol{k}'$ when a valence electron falls back to the core level. The initial and final state of the system might not be equal, which means that the system is left in an excited state. The energy of the excited state is equal to the energy loss of the photon $E_{\text{loss}} = \hbar\omega_{\boldsymbol{k}} - \hbar\omega_{\boldsymbol{k}'}$ from energy conservation. In the example of figure 5.1(a) there is an inter-orbital *dd*-excitation with E_{loss} ≈2 eV left after the scattering event. There is also the possibility of elastic scattering with E_{loss}=0 where the initial and final states are equal. The CDW order is characterized by an enhanced quasi-elastic scattering, which is thought to mainly come from a periodic modulation of the energy of the $2p_{3/2}$ to $d_{x^2-y^2}$ transition [118]. Figure 5.1(b) shows a typical RIXS spectra of YBCO with the *dd*-excitation peak and elastic peak highlighted.

As mentioned above, RIXS can also be used to study the momentum dependence and thus the dispersion of the excitations in a material. The momentum transferred to the material in a scattering event is $\hbar\boldsymbol{q} = \hbar\boldsymbol{k} - \hbar\boldsymbol{k}'$ where the magnitude and direction of $\boldsymbol{q}$ is set by the scattering geometry. Figure 5.2 shows the scattering geometry one typically use in RIXS measurements (the polarization of

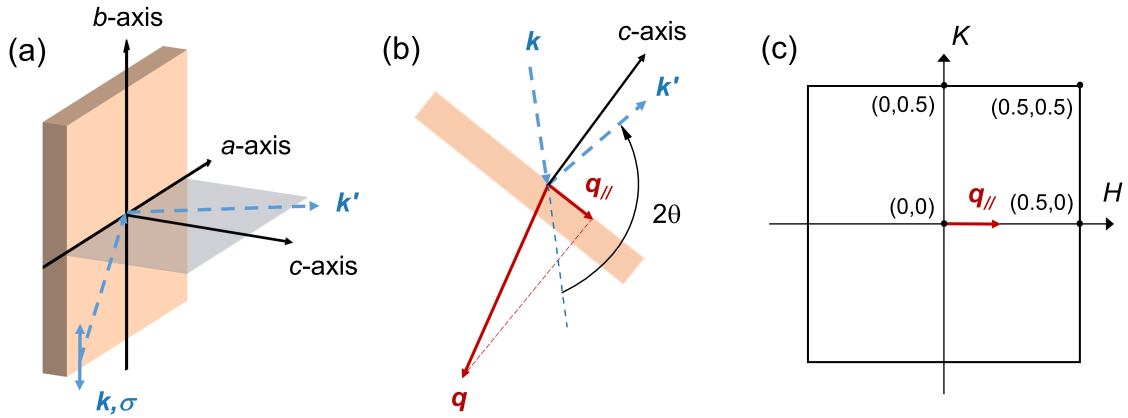

Figure 5.2: Geometry of the RIXS experimental setup in real and reciprocal space. See the text for description.

the incoming photons is set to vertical (σ), so to be parallel to the CuO_2 planes and therefore enhance the CDW signal.). In this example the scattering takes place in the YBCO a-c plane which means that $\boldsymbol{q}$ has components along the a- and c-axis. However, since the CuO_2 planes, that we probe by RIXS, are strongly 2D the meaningful momentum transfer is $\boldsymbol{q}_{//}$, the component of $\boldsymbol{q}$ parallel to the sample surface, see figure 5.2(b) [10]. To vary $\boldsymbol{q}_{//}$ the angle between the incoming and scattered photon 2θ (or equivalently the beam and the detector) is kept constant while the sample is rotated in the ab plane. Keeping a constant 2θ implies that the component of $\boldsymbol{q}$ parallel to the YBCO c-axis (L) will change when varying $\boldsymbol{q}_{//}$. This is however not a problem when measuring the CDW in YBCO since it is very weakly dependent on L [10], a consequence of its 2D nature. Figure 5.2(c) shows $\boldsymbol{q}_{//}$ in the Brillouin zone. The (H, K) components of $\boldsymbol{q}_{//}$ is given in units of the reciprocal lattice vectors $a^* = 2\pi/a$ and $b^* = 2\pi/b$.

5.2 Thickness dependence of CDW order in underdoped thin films

The RIXS measurements were carried out at the ID32 beamline at the European Synchrotron Radiaton Facility (ESRF) using the high-resolution ERIXS spectrometer [119]. The samples are mounted on a 6-axis in-vacuum diffractometer which allows full movement (translation and rotation). The energy and polarization of the incoming photons is set by the insertion device (wiggler) and the beamline optics ($\sim$ 931 eV, vertical polarization). The energy loss of the scattered photons is determined by the spectrometer, which mainly consists of a diffraction grating and a position sensitive detector. The energy resolution of the spectrometer was about 55 meV, determined by non-resonant elastic scattering of silver

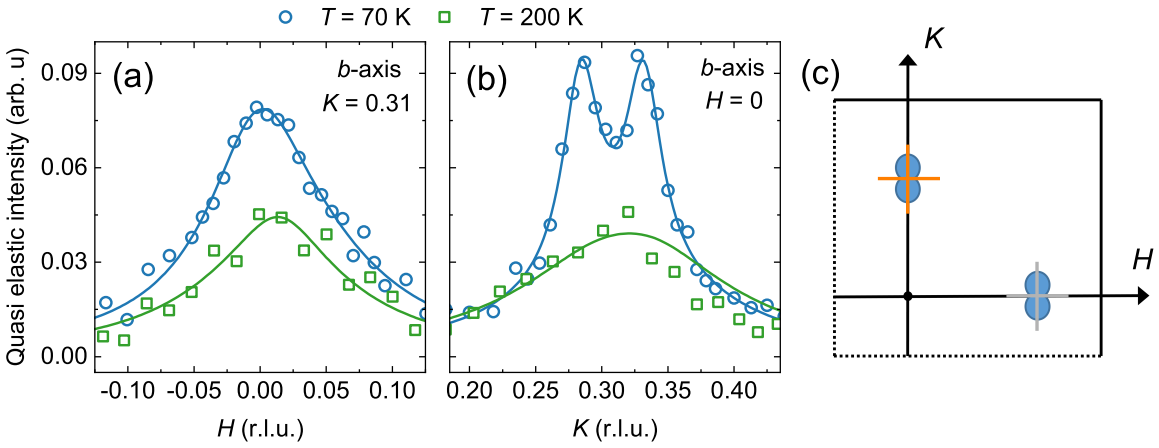

Figure 5.3: Quasi-elastic scans around $\boldsymbol{q}_{\mathrm{CDW,b}}$ measured at T= 70 K and T= 200 K in an untwinned 50 nm thick YBCO film on MgO with p ≈0.125. (a) H scan at K=0.31. (b) K scan at H=0. The lines are fits to the data (c) Positions of the CDW peaks (blue circles) and the scan directions (orange and gray lines) in momentum space. The scans of (a) and (b) correspond to the orange lines centered at (H,K)=(0,0.31).

paint. In order to maximize the transferable momentum to the sample the angle between the incoming beam and the spectrometer (2θ) was set to 149.5° which gives $|\boldsymbol{q}| = 0.91$ Å^{-1} (see figure 5.2). The large $|\boldsymbol{q}|$ allows access to the whole first Brillouin zone along H and K (0.5 rlu ≈ 0.81 Å^{-1}).

To characterize the CDW order as a function of the thickness (and strain) we measured t=10 and 50 nm untwinned YBCO thin films with p ≈0.125 on both MgO and vicinal angle cut STO. We performed scans in momentum space around the CDW component oriented along the a-axis $\boldsymbol{q}_{\mathrm{CDW,a}}$ (H=0.31, K=0) and b-axis $\boldsymbol{q}_{\mathrm{CDW,b}}$ (H=0, K=0.31). The measurements were done at two different temperatures, T = 70 K ≈ T_c and T = 200 K, close to the onset of the CDW order ($T^{\mathrm{on}}_{\mathrm{CDW}}$). At T_c, the CDW order is strongest and thus the scattering intensity maximized [10, 15]. The high T measurement is used to estimate the background since the CDW peak should be weak close to $T^{\mathrm{on}}_{\mathrm{CDW}}$. The quasi-elastic intensity at each value of $\boldsymbol{q}_{//}$ was extracted by integrating the spectra from -100 to +100 meV. To properly compare the quasi-elastic intensity in samples of different thickness and on different substrates we normalize the spectra to the intensity of the *dd*-excitation peaks, which is determined by integration from -1 to -3 eV.

MgO

In Figure 5.3 we present the momentum dependence of the quasi-elastic intensity around $\boldsymbol{q}_{\mathrm{CDW,b}}$ measured in a 50 nm thick film on MgO. In order to capture the full profile of the CDW peak in momentum space we measured along both the H

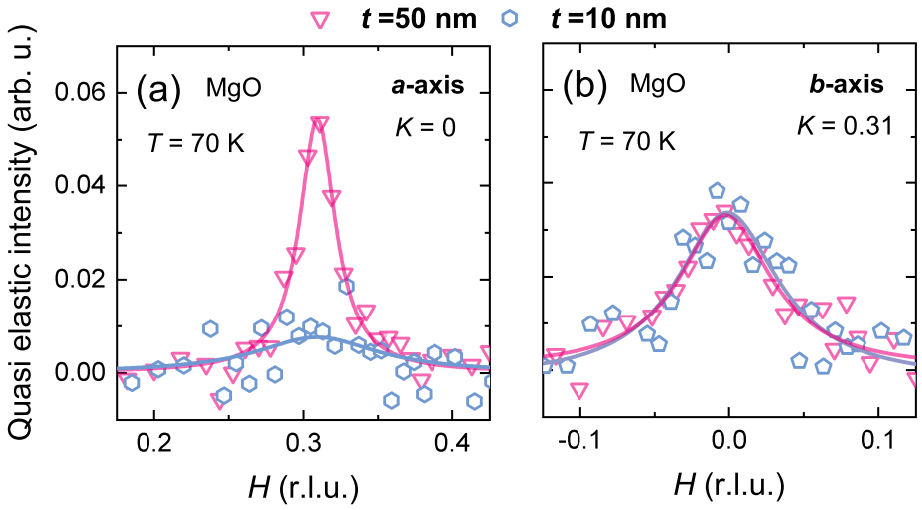

Figure 5.4: Thickness dependence of the CDW in underdoped ($p \approx 0.125$) YBCO thin films on 5h annealed MgO. (a) H-scans around $\boldsymbol{q}_{\mathrm{CDW,a}}$ (b) H-scans around $\boldsymbol{q}_{\mathrm{CDW,b}}$ in a t=50 nm film and a t=10 nm film.

and K directions, for both in-plane axes. The H scan at T=70 K (figure 5.3(a)) shows a single peak centered at $\boldsymbol{q}_{\mathrm{CDW,b}}$, as expected from scattering of the CDWs. The K scan instead (figure 5.3(b)) shows a broad peak centered at $\boldsymbol{q}_{\mathrm{CDW,b}}$ that is split along K. The peak splitting is a consequence of the buckling of YBCO thin films grown on MgO, as discussed in section 3.2. Since the CuO_2 planes (where the CDW order is localized) are buckled along the b-axis, the CDW scattering peak splits in the K direction. Figure 5.3(c) illustrates the shape of the CDW in momentum space (blue areas) and the scans along H and K (orange cross).

At T=200 K there is less quasi-elastic intensity at $\boldsymbol{q}_{\mathrm{CDW,b}}$, but there is still a broad feature in the scans. The broad peak comes from short-range charge density fluctuations (CDFs) which can be thought of as precursors to the CDW order [68]. CDFs are present in the major part of the YBCO phase diagram and have no significant temperature dependence, in contrast to the quasi-static CDW [68]. Since the CDFs are almost temperature independent the contribution of the quasi-static CDW peak at T=70 K can be isolated by subtracting the broad CDF peak.

Figure 5.4 summarizes the characterization of the CDW done on 10 and 50 nm thick YBCO thin films on MgO. To avoid the complications of the CDW peak splitting in K we focus on the scans measured along the H direction. The high T CDF contribution has been subtracted from the data for each scan. For the 50 nm thick film there is a clear CDW peak along both directions which means that there are CDW modulations along both in-plane axes. The presence of a biaxial CDW with equally intense a- and b- axis peaks is in perfect agreement with measurements on single crystals [10, 14]. In the 10 nm thick film instead

the H-scan of the b-axis CDW peak is nearly identical to the 50 nm case, while the a-axis CDW peak has a dramatically reduced contribution. If we consider the finite twinning of the thin film, the intensity of the a-axis peak can be considered to be zero. The absence of a CDW scattering peak along the a-axis tells that in the 10 nm thick film the CDW is uniaxial and oriented along the b-axis.

STO

To discern whether the uniaxial CDW is a unique property of films grown on MgO and thus related to the strain, or if it is general for very thin films, we performed the same kind of measurements on 10 and 50 nm thick untwinned films on vicinal angle cut STO at the same doping ($p \approx 0.125$). Since there is no buckling of the YBCO films grown on STO the CDW peaks are not split, but to compare to the films on MgO we focus on the data from the H-scans. The high T background is subtracted from the data in the same way as for the films on MgO. There are no significant difference in the shape or intensity of the CDF peak in the films grown on different substrates and of different thickness. Figure 5.5 summarizes the measurements of the CDW in the underdoped YBCO thin films on STO.

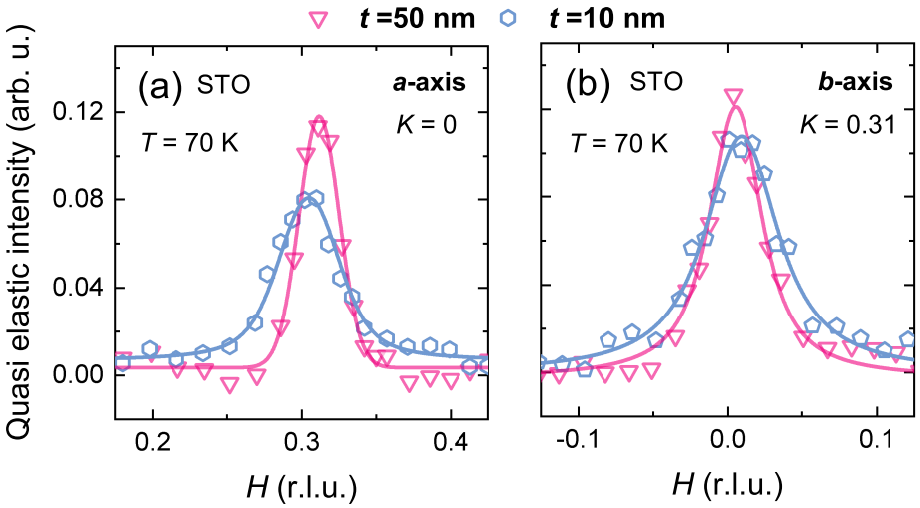

Figure 5.5: Thickness dependence of the CDW in underdoped ($p \approx 0.125$) YBCO thin films on vicinal angle cut STO. (a) H-scans around $\boldsymbol{q}_{\mathrm{CDW,a}}$ (b) H-scans around $\boldsymbol{q}_{\mathrm{CDW,b}}$ in a t=50 nm film and t=10 nm film.

The intensity of the CDW scattering peaks is higher compared to the ones measured in the films on MgO. This might be due to the buckling in the films on MgO which spreads the scattering intensity in reciprocal space. The CDW is biaxial, with almost equal scattering peaks at $\boldsymbol{q}_{\mathrm{CDW,a}}$ and $\boldsymbol{q}_{\mathrm{CDW,b}}$, just like for the 50 nm thick film on MgO. The measurements of the 10 nm thick film shows nearly the same result, but with a slight reduction of the intensity at $\boldsymbol{q}_{\mathrm{CDW,b}}$.

Discussion

The difference in the thickness dependence of the CDW in the films on MgO and STO can be accounted for if one considers the strain induced by the substrates. As we showed in figure 3.17(d) there is an increase of the YBCO b-axis lattice parameter by $\approx$0.44% in the films on MgO when the thickness is reduced from 50 to 10 nm. In the films on STO there is a similar but weaker effect. Here b increases by $\approx$0.18% when the thickness is reduced to 10 nm. For both substrates the a-axis lattice parameter is almost thickness independent. Thus there is a large in-plane uniaxial strain in the 10 nm thick YBCO films on MgO. RIXS measurements of the CDW order in YBCO single crystals have shown that uniaxial compression of one of the in-plane axes results in an enhancement of the CDW scattering intensity along the perpendicular in-plane axis [120], i.e compressing a gives more CDW along b. It is therefore likely that we observe the opposite effect in our strained thin films. As will be shown in the following chapter a strain induced distortion of the Fermi surface might also play a role in promoting the uniaxial CDW.

6 Interplay between strain, CDW and electric transport in underdoped $YBa_2Cu_3O_{7-\delta}$

Ever since the CDW was first discovered in the cuprates both its relation to the other local orders and its relevance in influencing the physics of the cuprates has been under intense investigation. In various other materials (not cuprates) which host CDW order there is a clear anomaly in the resistivity at $T_{\mathrm{CDW}}^{\mathrm{on}}$ [121, 122]. In YBCO instead, the proximity of the onset temperature of CDW with T^* (pseudogap temperature) does not allow to univocally associate the occurrence of CDW order with changes in $\rho(T)$. The only discernible effect of the CDW on the transport properties is the reduction of T_{c} due to the competition with superconductivity [15, 17, 64]. Recent experiments have shown that $T_{\mathrm{CDW}}^{\mathrm{on}}$ is much closer to T^* for $p > 0.12$ than previous measurements have shown (see supplementary materials of paper [IV]) . This opens up for a new possibility that the departure of linear in T resistivity, which happens at T^*, could be due to the CDW. In this thesis we have used strained ultrathin films to study the interplay between CDW and the linear $\rho(T)$ characteristic of the strange metal. The aim was to understand the physical mechanism breaking down the T-linear resistivity in YBCO and therefore the strange metal.

6.1 In-plane angular dependence of the resistivity

Since the uniaxial CDW order in the 10 nm thick films break the rotational symmetry of the CuO_2 planes one can expect an effect on the in-plane transport that depends on the angle. To investigate this possibility we have studied the in-plane angular dependence of the resistivity by 4-point measurements of microbars patterned at different angles ϕ relative to the YBCO a-axis using the method described in chapter 4. The geometry of the patterned devices is shown in figure 6.1. The bars, that are 5 μm wide with two voltage leads separated by 10 μm, were patterned on untwinned YBCO films grown on 5h annealed MgO and vicinal angle STO, 10 and 50 nm thick of different doping. In figure 6.2 we present $\rho(T)$ measurements of devices aligned to the YBCO a- and b-axis ($\phi = 0, 90°$) on four different YBCO films with $p \approx$0.11-0.12 to closely match the samples characterized by RIXS in chapter 5.

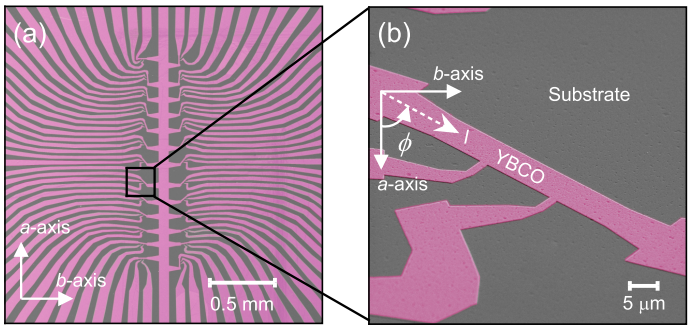

Figure 6.1: False color SEM images of the devices used to study the angular dependence of the resistivity in YBCO thin films.

By comparing the resistivity of the t=50 nm and t=10 nm devices on MgO in figure 6.2(a) and (b) we find three striking differences.

First, there is a large increase of the resistivity anisotropy ρ_a/ρ_b in the t=10 nm film. Second, the slopes $\gamma_{a,b}$ of the high temperature linear $\rho(T)$ are very different along the two directions in the t=10 nm film while $\gamma_a \approx \gamma_b$ in the t=50 nm film. Third, the temperature range of the linear resistivity at high T (T_L) is the same in ρ_a and ρ_b in the t=50 nm film ($T_L^a \approx T_L^b$) while the linear $\rho_b(T)$ extends to much lower T than $\rho_a(T)$ in the t=10 nm film ($T_L^a > T_L^b$). To estimate T_L we make a linear fit ($\rho_L = \gamma T + \rho_0$) to the high T resistivity data (dotted black lines in figure 6.2) and subtract it from the measured $\rho(T)$. The result of this procedure is shown in the insets of figure 6.2(a) and (b). We define T_L to be the temperature where there is a 1% deviation of $\rho(T)$ from the linear fit, marked by the black dashed line in the insets.

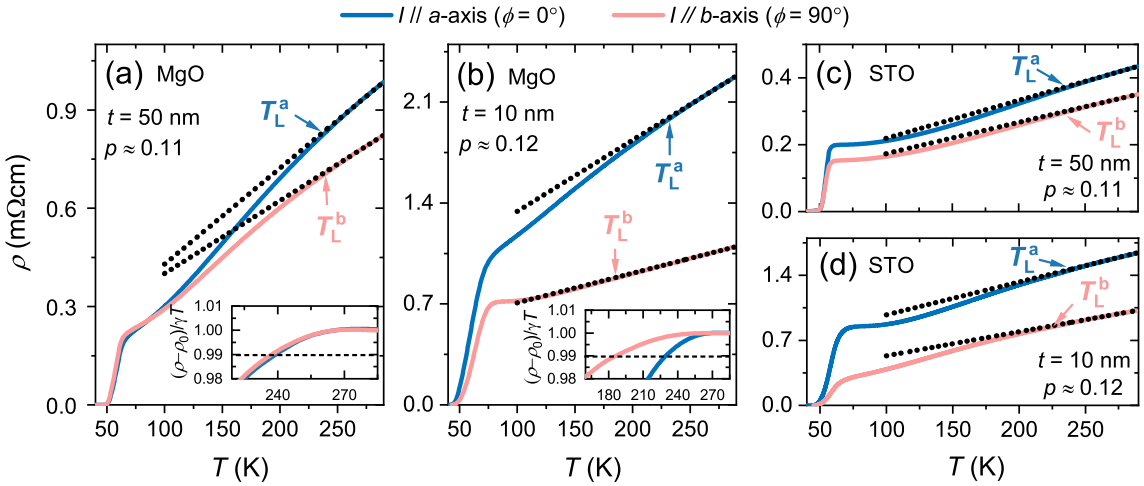

Figure 6.2: In-plane resistivity of devices oriented along the a- and b-axis in patterned YBCO thin films. (a) 50 nm thick film on MgO, (b) 10 nm thick film on MgO, (c) 50 nm thick film on STO and (d) 10 nm thick film on STO.

Substrate	t (nm)	ρ_a/ρ_b	γ_a/γ_b	T_L^a (K)	T_L^b (K)
MgO	50	1.2	1.3	239	238
MgO	10	2.1	2.3	229	187
STO	50	1.3	1.2	239	239
STO	10	1.6	1.3	236	235

Table 6.1: Summary of the anisotropic parameters extracted from the resistivity measurements in figure 6.2 for $p \approx 0.11 - 0.12$. Note that the values of ρ_a/ρ_b and γ_a/γ_b is reported at T=290 K.

Figure 6.2(c) and (d) shows analogous measurements of devices on vicinal angle cut STO substrates. Here, both the 10 and 50 nm thick samples show characteristics that are close to those measured in the 50 nm thick film on MgO. T_L does not depend on the current direction, and the ratio between the slopes γ_a/γ_b is approximately the same for the thin and thick samples. There is however a small increase of ρ_a/ρ_b when reducing the thickness. Table 6.1 presents the values of ρ_a/ρ_b, γ_a/γ_b and T_L extracted from the resistivity measurements in figure 6.2. The conclusion that can be drawn from this data is that there is an unconventional in-plane resistivity anisotropy in the 10 nm thick YBCO film on MgO. The anisotropic T_L and the increase of the ratio γ_a/γ_b is observed only in the 10 nm thick film on MgO while for the 10 nm thick films on STO and MgO the higher values of ρ_a/ρ_b compared to the 50 nm thick films might be partly due to thickness effects [123]. Which physical mechanism is behind the extension of the strange metal to lower temperatures?

Increase of ρ_a/ρ_b and γ_a/γ_b

As we discussed in section 3.2, the large ρ_a/ρ_b in slightly overdoped YBCO can be completely accounted for by considering the conductivity contribution of the *b*-axis oriented CuO chains [86, 87]. The parallel chain conductivity quickly diminishes when the doping (and therefore the oxygen content in the chains) is reduced which results in a smaller ρ_a/ρ_b. The small ρ_a/ρ_b at high T in the 50 nm thick films with $p \approx 0.11$ in figure 6.2(a,c) is in good agreement with measurements on untwinned single crystals of similar doping [86], where it is commonly ascribed to a small residual chain conductivity along the *b*-axis. The large ρ_a/ρ_b of the 10 nm thick film with $p \approx 0.12$ on MgO (figure 6.2(b)) is instead much higher than expected and close to that of slightly overdoped YBCO. There is no reason to believe that the chains are more conductive in the thinner sample, so the increased anisotropy should have a different origin. A hint comes from the increase of the ratio γ_a/γ_b. Following the Boltzmann transport theory, the electrical conductivity σ along the

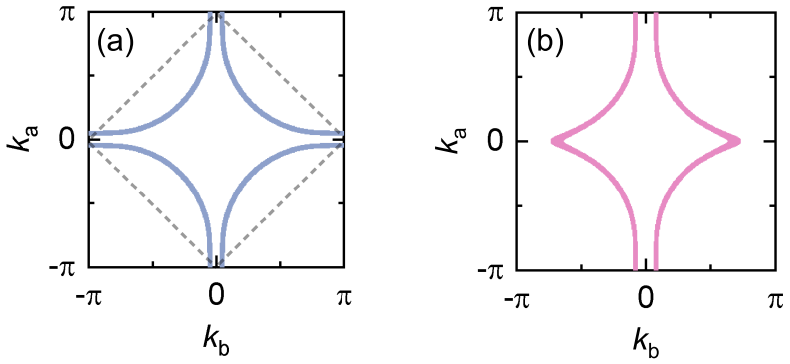

Figure 6.3: Example of Fermi surface modification that is compatible with the higher resistivity anisotropy in the 10 nm thick film on MgO. (a) Typical Fermi surface of the cuprates ($t_a = t_b$) (b) $t_b > t_a$. The effects of the CuO chains and bi-layer splitting is neglected.

a- and b-axis is given by

$$\sigma_{a,b}(T) = 2e^2 \sum_{\boldsymbol{k}} \frac{v^2_{F,a,b}}{\Gamma(\boldsymbol{k})}\{-n'_F\} \tag{6.1}$$

where $v_{F,a,b}$ is the Fermi velocity component directed along the YBCO a- and b-axis, $\Gamma(\boldsymbol{k})$ the $\boldsymbol{k}$ dependent scattering rate and n'_F the derivative of the Fermi distribution [45]. The scattering rate can be expressed as the sum of an elastic, temperature independent part and an inelastic, temperature dependent part $\Gamma = \Gamma_{el} + \Gamma_{inel}(T)$. Anisotropic elastic scattering from e.g. structural defects could in principle explain the increase of ρ_a/ρ_b, but cannot account for the increase of γ_a/γ_b [124]. The slope $\gamma_{a,b}$ is determined by the ratio $\Gamma_{inel}(\boldsymbol{k}, T)/v^2_{F,a,b}$, which means that the anisotropic $\rho(T)$ is compatible with different Fermi velocities along the two in-plane axes. Since $\gamma_a > \gamma_b$ we have that $v_{F,b} > v_{F,a}$ and consequently a strongly anisotropic Fermi surface in the 10 nm thick film on MgO. Figure 6.3(a) shows the typical Fermi surface of the cuprates which is relevant for the 50 nm thick sample and figure 6.3(b) a strongly anisotropic one compatible with the anisotropic resistivity of the 10 nm thick sample. What is the reason for the anisotropic Fermi surface? We know that there are two unique properties of the 10 nm thick film on MgO, namely the larger orthorhombicity (see figure 3.17) and the uniaxial CDW. Both break the C_4 symmetry of the plane. Since T^{on}_{CDW} is less than room temperature, where the resistivity anisotropy is already present, the CDW is not a likely candidate for the phenomenology we observe. Neither is the increased orthorhombicity. This is easily seen if we consider a simple tight-binding model commonly used for the cuprates [125]

$$E(k) = -2(t_a \cos(k_a) + t_a \cos(k_a)) + 4t' \cos(k_a)\cos(k_a) \tag{6.2}$$

where $t_{a,b}$ is the nearest neighbour hopping parameter along the a- and b-axis and t' the next-nearest neighbour hopping parameter. The fact that $\gamma_a > \gamma_b$ and $\rho_a > \rho_b$ ($v_{F,b} > v_{F,a}$) implies that $|t_b| > |t_a|$, while an increase of b relative to a implies a decrease of $|t_b|$ relative to $|t_a|$. The increased orthorhombicity should thus lead to an increase of ρ_b and γ_b, which is opposite to what we observe [126]. Instead, we can speculate that the anisotropic Fermi surface is a consequence of a nematic state that is stabilized because of the peculiar strain in the 10 nm thick film on MgO. Nematicity is a common feature of the cuprate phase diagram [102, 127, 128] and has been extensively investigated from a theoretical point of view [80, 129, 130]. A nematic state at room temperature has been experimentally found, by in plane resistivity anisotropy measurements, in tetragonal $La_{2-x}Sr_xCuO_4$ [131] films and at lower T in the other cuprates, including YBCO [102, 132]. It is not implausible that strain makes a nematic ground state more energetically favourable.

Anisotropic linear resistivity

In the previous section we argued that the increase of ρ_a/ρ_b and γ_a/γ_b can be explained by a strongly anisotropic Fermi surface. Can it also explain the anisotropy of the T-linear range of $\rho(T)$? A hint comes from the in-plane angular dependence of γ and T_L, shown in figure 6.4. $\gamma(\phi)$ can be perfectly fitted by a sinusoidal curve. In contrast $T_L(\phi)$ is narrowly peaked at $\phi = 90°$ (b-axis). The different angular dependence of γ and T_L suggests that their anisotropic behavior is of different origin.

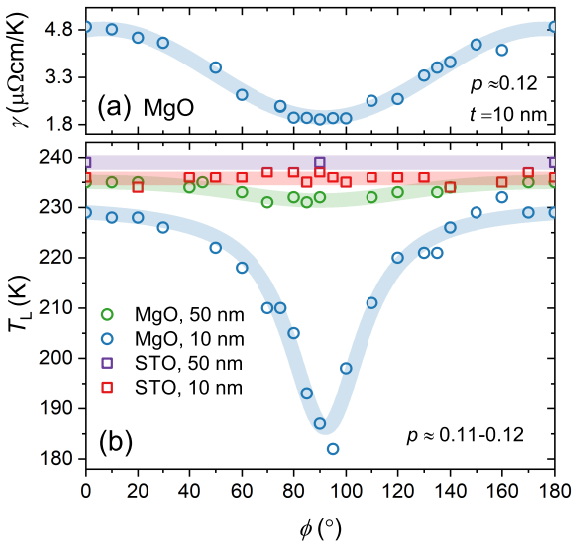

Figure 6.4: In-plane angular dependence of (a) γ measured in the patterned 10 nm thick film on MgO and (b) T_L measured in the samples presented in figure 6.2.

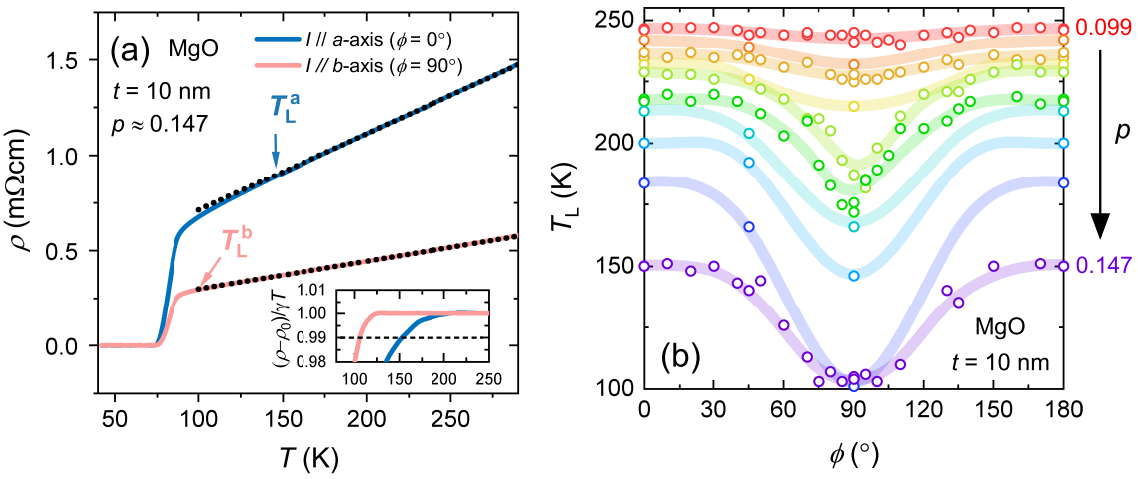

Figure 6.5: Doping dependence of the in-plane resistivity measured in 10 nm thick devices on MgO. (a) $\rho(T)$ of $p \approx 0.147$ devices aligned along the a- and b-axis. (b) In-plane angular dependence of T_L as a function of the doping in patterned 10 nm thick films on MgO. The approximate doping values of the films are from low to high: 0.099, 0.103, 0.108, 0.117, 0.118, 0.120, 0.123 , 0.134, 0.140, 0.147.

To gain more information on the anisotropy of T_L with ϕ we measured the angular dependence of the resistivity as a function of the doping. Figure 6.5(a) shows $\rho(T)$ measured in devices oriented along the a- and b-axis of a slightly underdoped film ($p \approx 0.147$). The slight increase of resistivity anisotropy at 290 K ($\rho_a/\rho_b \approx 2.6$) compared to the measurements at $p \approx 0.12$ (figure 6.2(b)) is compatible with measurements on single crystals where the increase of ρ_a/ρ_b with doping is commonly ascribed to CuO chain conductivity [86]. This finding suggests that the excess anisotropy coming from the anisotropic Fermi surface in the 10 nm thick films is not very sensitive to the doping.

The in-plane anisotropy of T_L instead is strongly doping dependent. $\rho_b(T)$ is linear down to the superconducting resistive transition at $p \approx 0.147$ which normally only happens close to $p^*=0.19$ where the strange metal phase extends to $T = 0$ [3, 46, 47]. In figure 6.5 we present the ϕ dependence of T_L measured in thin film devices spanning a wide doping range. There is a clear trend that the difference between T_L^a and T_L^b decreases when the doping is reduced. At $p \approx 0.1$, $T_L(\phi)$ is almost constant while the largest difference is found in the $p \approx 0.14$ sample where T_L^b is close to T_c. The fact that T_L^a/T_L^b is larger at $p \approx 0.14$ than at $p \approx 0.147$ indicates that $T_L^b \approx 100$ K is only an upper limit in those samples. To get the exact value of T_L^b at this doping one would need to suppress superconductivity with a strong magnetic field to extend the normal state to lower temperatures. The fact that T_L^a/T_L^b is strongly doping dependent while γ_a/γ_b and ρ_a/ρ_b is not (subtracting the intrinsic doping dependence found in crystals) further strengthen the claim that the effects have different origins.

As we mentioned in the introduction of this chapter and in section 2.2, T_{L} has historically been associated to the appearance of the pseudogap at T^* [9]. Here we will argue that the extension of the linear $\rho(T)$ down to T_{c} can be connected to the disappearance of the CDW along the a-axis, and therefore that T_{L} should be associated to the onset of CDW, at least in the doping range that we have investigated.

Discussion

The first point to address is why the linear $\rho(T)$ is modified along the b-axis when the CDW is suppressed along the a-axis. The answer comes from the geometry of the Fermi surface and its relation to the scattering by a CDW. At the temperature onset of a translational symmetry breaking order, such as the CDW, new scattering channels become available for electron states close to the Fermi level that can be connected by the characteristic q-vector of the order. If we consider the typical cylindrical Fermi surface of the cuprates and scattering by a uniaxial CDW along the b-axis with q_{CDW}=0.31 rlu there are two different possible scattering channels: one connecting states in the nodal region in the center of the Brillouin zone and one in the anti-nodal region crossing the zone boundary and connecting different zones, as shown by the red arrows in figure 6.6(a). The impact of the scattering on the transport along the a- and b-axis can be evaluated through the Boltzmann transport equation 6.1. In the nodal region, the Fermi velocity components directed along the a- and b-axis are approximately equal ($v_{\mathrm{F,a}} \approx v_{\mathrm{F,b}}$), which means that the scattering from the CDW will affect the resistivity in both directions. In the anti-nodal region instead, the Fermi velocity component along a is much larger than the component along b ($v_{\mathrm{F,a}} > v_{\mathrm{F,b}}$) which means that here the b-axis oriented CDW primarily affects the a-axis resistivity. We can thus reconcile the anisotropic T_{L} to the uniaxial CDW if the scattering in the anti-nodal region is more pronounced than in the nodal region. This is indeed the case, since the CDW scattering rate is proportional to the density of states at the Fermi level, which is larger close to the zone boundary, giving a scattering rate that is approximately double in the anti-nodal region [52]. The scattering rate in the anti-nodal region increases even more if we consider the anisotropic Fermi surface that is compatible with the resistivity anisotropy discussed above, see figure 6.6(b). Here the density of states is strongly enhanced at the tips of the Fermi surface which results in a CDW scattering rate that is almost four times higher than in the nodal region. Figure 6.6(c) shows the CDW scattering rates (Γ_{CDW}) versus the angle φ for the isotropic and anisotropic Fermi surfaces, calculated according to reference [52] (see supplementary materials of paper [IV]).

Figure 6.6(d) shows the Fermi velocity a- and b-axis components versus φ for the anisotropic Fermi surface. Similarly to the isotropic Fermi surface we have that $v_{\mathrm{F,a}} \approx v_{\mathrm{F,b}}$ in the nodal region while $v_{\mathrm{F,a}} \gg v_{\mathrm{F,b}}$ close to the tip. The

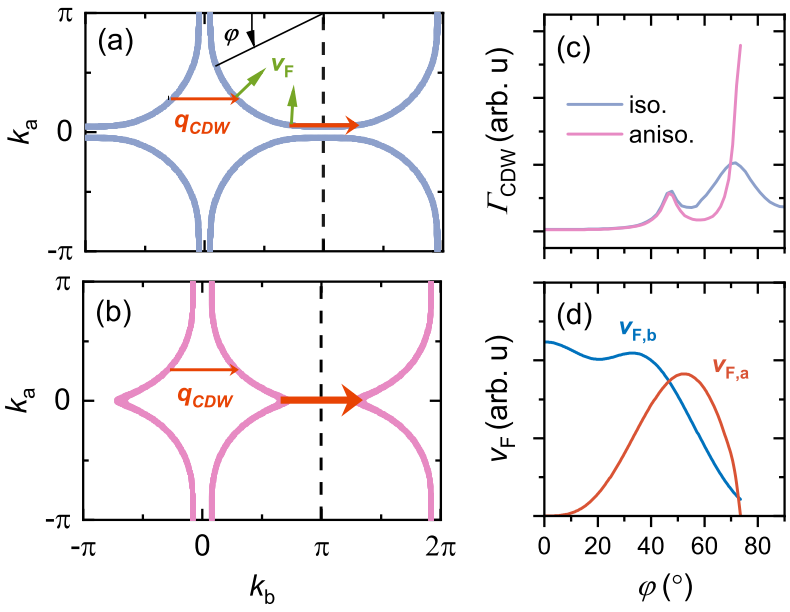

Figure 6.6: Uniaxial CDW scattering on (a) isotropic and (b) anisotropic Fermi surface. The red arrows shows the CDW scattering vector where the size is proportional to the scattering rate. The green arrows show the direction of the Fermi velocity at the CDW scattering points. (c) Angular dependence of the CDW scattering rate in for the isotropic Fermi surface in (a) and the anisotropic Fermi surface in (b).(d) Fermi velocity versus the angle ϕ defined in (a) for the anisotropic Fermi surface in (b).

strong scattering from the CDW in the anti-nodal region described here, together with the anisotropic Fermi surface as shown in figure 6.6(b), can account for the anisotropic transport that we observe in the 10 nm thin film on MgO (see figure 6.2(b) and 6.5(a)) if we make the following assumptions:

- Above T_L^a and T_{CDW}^{on} the inelastic scattering rate is proportional to the temperature ($\Gamma_{inel} \sim T$) which gives $\rho(T) \sim T$.
- The large ρ_a/ρ_b and γ_a/γ_b comes from the anisotropic Fermi velocity $v_{F,b} \gg v_{F,a}$, a consequence of the nematic Fermi surface.
- Below T_L^a, the uniaxial b-axis oriented CDW sets in and mainly affects the scattering in the orthogonal a-axis direction, which causes a deviation from the linear $\rho_a(T)$.

Since there is no a-axis oriented CDW (that would mainly affect the scattering in the b-axis direction) ρ_b remains linear in T across T_{CDW}^{on} (and T^*). In this scenario the strange metal phase would extend to lower T and p in the absence of CDW order.

However, we need to explain why the CDW causes the resistivity to decrease below T_{L}. In most cases the introduction of a new scattering channel increases the scattering rate. To account for the faster decrease of $\rho_{\mathrm{a}}(T)$ at $T_{\mathrm{L}}^{\mathrm{a}}$ the CDW should in principle cause Γ_{inel} to decrease. A decrease of Γ_{inel} can come from e.g. paraconductivity mediated by the quasi-elastic CDW [133]. Another possibility is that the deviation from the linear $\rho_{\mathrm{a}}(T)$ is caused by the opening of a CDW gap in the Fermi surface. If there are regions of the Fermi surface that support scattering by electronic excitations the opening of a gap in those specific regions can reduce scattering events and thus decrease the resistivity [9, 48].

One remaining point to address is why T_{L} is isotropic below $p \approx$0.11. In this doping range it is safe to assume that the CDW is still uniaxial. Since the anisotropy in γ ($\gamma_{\mathrm{a}}/\gamma_{\mathrm{b}}$) does not change significantly with the doping we can assume a nematic Fermi surface also for $p < 0.11$, supporting a uniaxial CDW. Nonetheless we do not observe an anisotropy in T_{L}. It thus seems that the CDW order has a different impact on the transport above and below $p \approx 0.11$. A possible explanation comes from the different doping dependence of $T_{\mathrm{CDW}}^{\mathrm{on}}$, T_{L} and T^*. At low doping ($p < 0.11$) both $T_{\mathrm{L}}^{\mathrm{a}}$ and $T_{\mathrm{L}}^{\mathrm{b}}$ are close to T^*, the pseudogap temperature. $T_{\mathrm{CDW}}^{\mathrm{on}}$ instead is much lower. This hints at a pseudogap that is isotropic on the nematic Fermi surface, and that in this doping range the deviation from linear $\rho(T)$ at T_{L} can be caused by a pseudogap-related mechanism. An isotropic pseudogap cannot explain the anisotropic T_{L} at higher doping ($p > 0.11$). In this doping range, where $T_{\mathrm{CDW}}^{\mathrm{on}} \approx T_{\mathrm{L}}^{\mathrm{a}} \approx T^*$, the T-linear resistivity behavior is broken down by the CDW order, which is anisotropic in the 10 nm thin film on MgO resulting in $T_{\mathrm{L}}^{\mathrm{b}} < T_{\mathrm{L}}^{\mathrm{a}}$. This conjecture is supported by transport measurements in YBCO single crystals which show that the in-plane transport anisotropy in the normal state can be associated to the CDW order above $p \approx$0.11 and to the pseudogap below that doping [102].

To summarize, the measurements shown here provide convincing evidence that the CDW order has a strong impact on the normal state transport properties in YBCO. In the absence of symmetry-breaking orders such as CDW the strange metal phase would cover a larger part of the phase diagram and could be the true ground state of the cuprates.

7 Reshaping the phase diagram with strained $YBa_2Cu_3O_{7-\delta}$ thin films

The electronic phase diagram of the HTS cuprates describes how the properties of the materials evolve with doping. New information about the hierarchy among the different phases can be an important step towards understanding the HTS phenomenon. The relation between CDW order and superconductivity has received a lot of attention lately and it is by now well established that they are competing. However, the exact nature of the competition is still not settled [64]. The CDW order also have implications on the normal state of the cuprates. The experimental finding of small Fermi surface electron pockets, inferred from quantum oscillations in underdoped YBCO [18], seem to points towards an active role of bidirectional CDW to reconstruct the Fermi surface of the cuprates [19, 67]. It might also be involved in the breaking of the strange metal, as we argued for in chapter 6.

To get a better understanding of the role of CDW order in the physics of the cuprates we have measured the Hall coefficient and the resistivity as a function of the doping and temperature of the 10 nm thick YBCO films on MgO. These measurements show how the phase diagram is reconstructed for the highly strained thin films in connection with the uniaxial CDW.

7.1 Resistivity measurements

To understand how strain and dimensionality affect the phase diagram of the 10 nm thick YBCO films we need to carefully determine the doping dependence of T_c. This is particularly important since the changes that we have detected in the CDW might change the competition with superconductivity and possibly the suppression of T_c around $p \approx 1/8$. Figure 7.1 shows the $\rho(T)$, measured in t= 10 nm untwinned YBCO films on MgO, along the a- and b-axis in a 4-point van der Pauw configuration [85]. We observe similar behavior as in the patterned devices in chapter 6 regarding the anisotropic resistivity with $T_L^b < T_L^a$. This tells that the extension of linear $\rho(T)$ along the b-axis is not a peculiarity of the patterning process but and intrinsic property of the strained thin films.

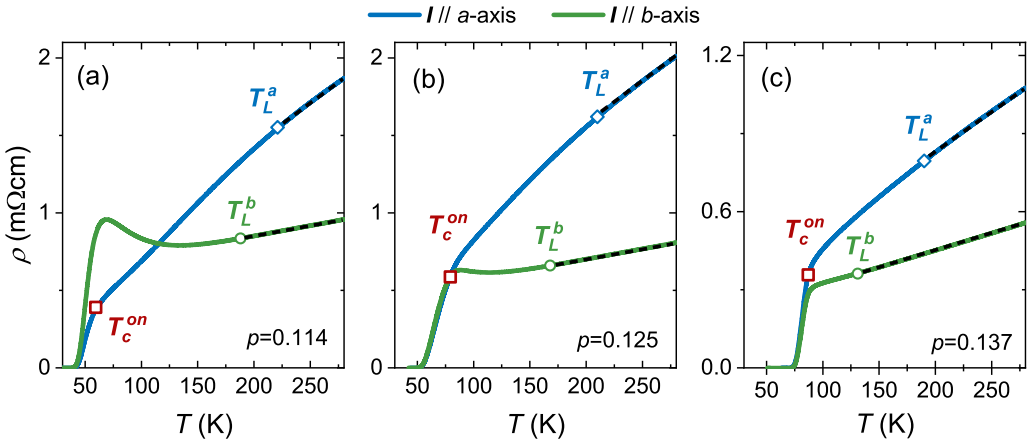

Figure 7.1: Resistivity measurements along the a- and b-axis of 10 nm thick untwinned YBCO films on MgO. (a) $p \approx 0.114$ (b) $p \approx 0.125$ (c) $p \approx 0.137$

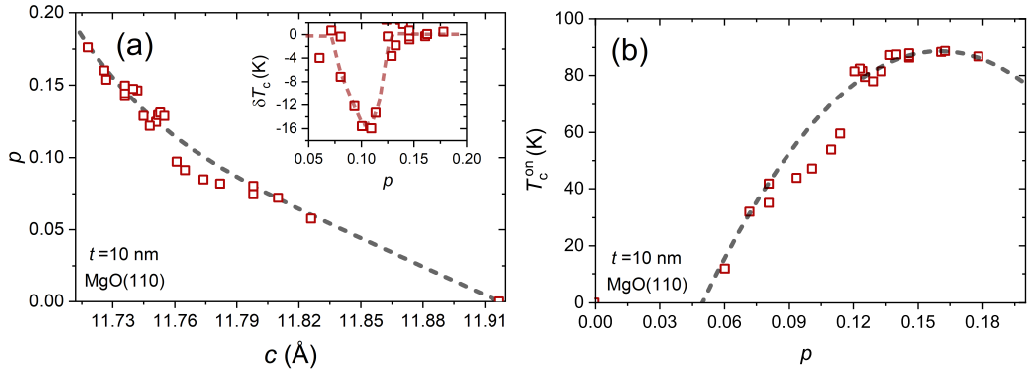

Figure 7.2: Determination of the doping of 10 nm thick untwinned YBCO thin films on 5h annealed MgO(110) and construction of the phase diagram. (a) hole doping p (extracted from equation 3.1) versus c. The dashed gray line is a fit to the data for $p < 0.09$ and $p > 0.14$. The inset shows the difference between the measured T_c and equation 3.1. (b) Doping dependence of T_c^{on} The gray dashed line is the empirical parabolic $T_c(p)$.

The doping of each film is determined in the same way as described for the 30 nm thick twinned films in section 3.4 by correlating the the c-axis lengths extracted from the $(00L)$ Bragg reflections (see figure 3.18) to T_c. To account for the large broadening of the transition and the upturn of ρ_b at low T, which complicates the determination of T_c (see figure 7.1(a)), we use T_c=$T_c^{on,a}$ in the empirical parabolic equation 3.1. Figure 7.2(a) shows the $p(c)$ fit for the 10 nm thick films and figure 7.2(b) the resulting $T_c^{on,a}(p)$. There is a clear deviation of T_c from the parabolic doping dependence at low doping and the magnitude of the deviation δT_c (shown in the inset of 7.2(a)) is approximately equal to what we found for the 30 nm thick films. However, the doping range of suppressed T_c is different. In the 10 nm thick films $T_c(p)$ follows the parabolic dome down to

$p \approx 0.12$ in contrast to the thicker films where the deviations are observed already at $p \approx 0.14$ (see figure 3.16(a))[1].

More information about the interaction between the uniaixal CDW and superconductivity can be gained by looking at the broadening of the resistive transition. Figure 7.3(a)-(c) shows the derivative of the $\rho(T)$ curves in figure 7.1 around T_c. The excess broadening at $p \approx 1/8$ [41] is clearly seen in figure 7.3(b). The transition is sharper at higher and lower doping (figures 7.3(a) and (c)). However, an interesting feature is that the broadening is more significant in ρ_a than in ρ_b. Since the zero resistance critical temperature T_c^0 is the same in the two directions the anisotropy of ΔT_c must come from a difference in T_c^{on}. To highlight the anisotropy of the resistive transition we plot the difference between ΔT_c along the a-axis, ΔT_c^a and that along the b-axis, ΔT_c^b as a function of the doping (see figure 7.3(d)). We also include data from 50 nm thick untwinned YBCO films for comparison. In the 50 nm thick YBCO films (with biaxial CDW) ΔT_c is isotropic with no strong doping dependence. In the 10 nm thick films (with uniaxial CDW) there is instead a peak which highlight an increased anisotropy at $p \approx 0.128$.

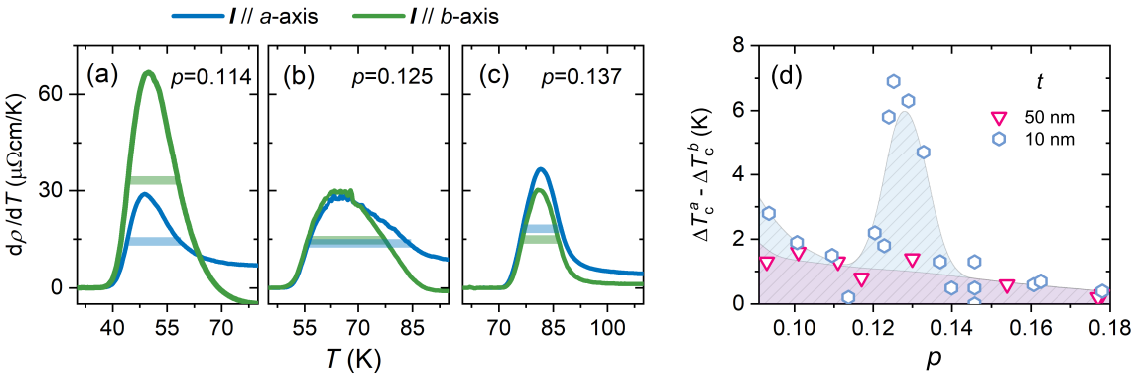

Figure 7.3: Broadening of the resistive transition in YBCO thin films. (a)-(c) temperature derivative of $\rho(T)$ at the resistive transition measured along a and b. The wide bars correspond to ΔT_c (FWHM). (d) difference between ΔT_c along a and b in 10 and 50 nm thick films. The shaded areas are guides for the eye.

The smaller suppression of T_c^{on} (primarily along the a-axis) and the anisotropic ΔT_c in the doping interval $0.12 \leq p \leq 0.14$ are most likely consequences of the modified CDW in the 10 nm thin films. First, because of the suppression of the a-axis oriented CDW component, the total volume of CDW order domains is smaller. This should lead to a weaker influence of the CDW order on the superconducting state. Pressure studies on YBCO crystals have shown an enhancement of T_c that can be related to the suppression of CDW order [23, 24]. In these works no anisotropy of T_c was observed, most likely because the applied pressure was

[1] We get a similar $T_c(p)$ for the 10 nm thick films by considering T_c^{av} instead of T_c^{on} but shifted to lower p and T

isotropic. Second, since the CDW is uniaxial it has different influence on the transport parallel and perpendicular to the charge modulation. This leads to an unperturbed T_c^{on} along the a-axis that follows the empirical parabolic dome (down to $p \approx 0.12$).This result is in line with studies of stripe ordered Nd-LSCO where modest uniaxial strain has been shown to strongly suppress the stripe order and recover a T_c that is close to the value expected from a empirical parabolic doping dependence [134, 135].

7.2 Fermi surface reconstruction

As was briefly introduced in section 2.2 there is strong evidence for a reconstruction of the Fermi surface (FS) from hole-like at high T to electron like at low T in underdoped YBCO [20]. The reconstruction is inferred from a change of the sign of the Hall coefficient R_H from positive to negative at $T \approx 100$ K, indicative of a change of the dominant charge carrier from holes to electrons [65]. Further evidence comes from the observation of quantum oscillations of e.g. the resistivity in underdoped YBCO [18]. The oscillation frequency, that is directly related to the area of closed orbits on the FS, is incompatible with the large hole-like cylinder (and the Fermi arcs) common in the cuprates. Instead the quantum oscillation measurements indicate a small closed pocket with an area of only 2% of the Brillouin zone [18].

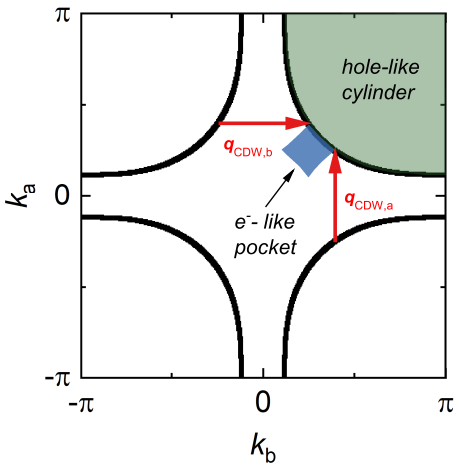

Figure 7.4: Illustration showing how a biaxial CDW can reconstruct a large hole-like cylinder to a small electron-like pocket through zone-folding [67].

Since both the sign change of R_H and the quantum oscillations are only present in the doping range $0.08 < p < 0.16$, where there is CDW order at low temperature, it is very likely that the FS reconstruction is a consequence of the CDW. Figure 7.4 illustrates the commonly proposed scenario for the mechanism of FS

reconstruction by the CDW [19, 67]. At high T the FS consists of a large hole-like cylinder (centered at (π,π)), as inferred from e.g. ARPES measurements [136] or quantum oscillations [137] in overdoped $Tl_2Ba_2CuO_{6+\delta}$. If we assume that the FS is zone-folded by q_{CDW} along the a- and b-axes one gets a small electron like pocket in the nodal direction (blue area in figure 7.4), the size of which is compatible with the quantum oscillation frequency measured in underdoped YBCO [18]. However, the mechanism of figure 7.4 requires a bi-axial CDW to work. A uniaxial CDW would produce open FS sheets and no closed pockets that can give rise to quantum oscillations [138].

Since the CDW evolves from biaxial for $t = 50$ nm to uniaxial for $t = 10$ nm in our films we can use this experimental finding to test the validity of the scenario outlined above. Quantum oscillation measurements require extremely high magnetic fields and very pure samples which makes them challenging for thin films while measurements of R_H only require modest fields. Following Ref. [139] the sign change of the Hall coefficient can be inferred from the maximum of R_H at the temperature T_{max}, which does not require high fields to suppress superconductivity.

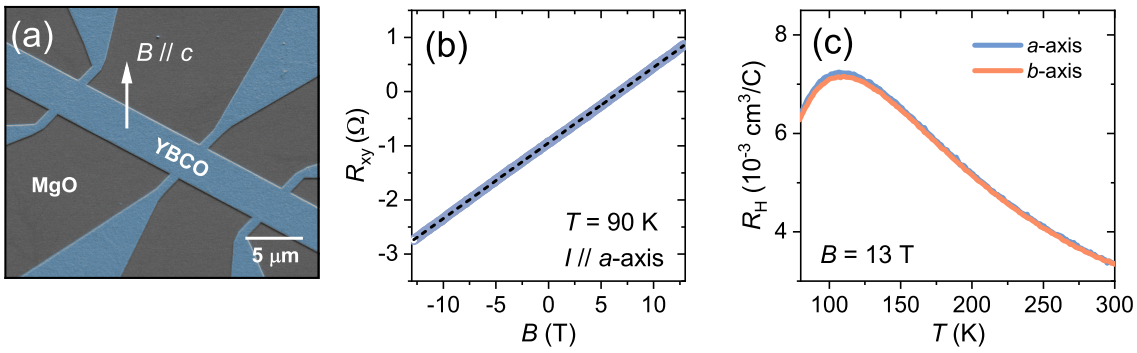

Figure 7.5: Measurements of the Hall coefficient in YBCO thin films. (a) False color SEM image of a patterned Hall Bar. (b) Magnetic field sweep of the transverse resistance R_{xy} in a 50 nm thick Hall bar oriented along a. (c) Temperature sweep of the Hall coefficient R_H in Hall bars oriented along a and b in the same film as (b).

In order to measure the temperature dependence of the Hall coefficient R_H we patterned Hall bars on the untwinned YBCO thin films on MgO. The Hall bars are $5\mu m$ wide and oriented along the YBCO a- or b- axis with 1μm wide voltage leads to measure the transverse voltage V_H in a c-axis oriented magnetic field, see figure 7.5(a). Figure 7.5(b,c) show a magnetic field sweep of $R_{xy}=V_H/I$ at $T = 90$K and a temperature sweep of $R_H(T)$ in a 50 nm thick underdoped Hall bar ($p \approx 0.115$) respectively. In all measurements there is a zero field offset of R_{xy} that possibly comes from a small misalignment of the voltage probes or from the presence of nematic order [131], which will be the object of further investigation and therefore outside the scope of this thesis. The Hall coefficient

is estimated from the linear slope of $R_{xy}(B)$, or in most cases from $R_{xy}(T)$ at constant $B = 0,13$ T, through $R_H = R_{xy}/B \cdot t$[1]. The temperature dependence of R_H shown in figure 7.5(c) is typical of underdoped YBCO [106]. R_H is positive, indicating hole-like transport, and increases with lower T to reach a maximum at $T = T_{max}$. Below T_{max} R_H decreases and eventually would turn negative if the magnetic field was strong enough to suppress superconductivity [65, 139]. The sign change of R_H is commonly ascribed to a Fermi surface transformation as described above. Superconducting fluctuations close to T_c can also give rise to a decrease of R_H, but then $R_{xy}(B)$ becomes non-linear. To avoid misinterpretation of the data we only show $R_H(T)$ where $R_{xy}(B)$ is linear in the full magnetic field range. As shown in figure 7.5(c), $R_H(T)$ is independent of the measurement direction. This is expected from Onsager's reciprocal relations [140], but it is also a confirmation of the homogeneity of the samples since variation in doping between the different Hall bars would affect the magnitude and shape of $R_H(T)$.

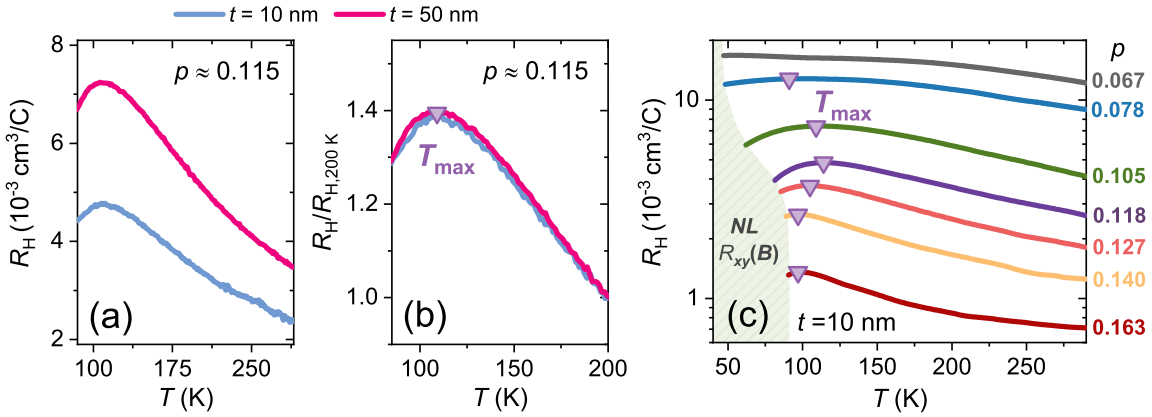

Figure 7.6: (a) Comparison of $R_H(T)$ in 10 and 50 nm thick, underdoped Hall bars oriented along a. (b) same as (a) but normalized at T= 200 K. (c) Doping dependence of $R_H(T)$ in 10 nm thick Hall bars. The green shaded area roughly corresponds to the temperature range where $R_{xy}(B)$ is non-linear.

Figure 7.6(a) shows a comparison of $R_H(T)$ measured in 10 and 50 nm thick Hall bars with similar doping level. We observe that the magnitude of $R_H(T)$ is lower in the 10 nm thick Hall bar. However, T_{max}, a measure of the FS reconstruction, is approximately the same. This is better visualized in figure 7.6(b) where the normalized curves fall on top of each other. Figure 7.6(c) shows the result of $R_H(T)$ measurements of 10 nm thick Hall bars spanning a wide doping range. The shape of the curves correspond well to what has been measured in single crystals [106], where $T_{max}(p)$ has a dome-like shape with a maximum at $p \approx 0.12$, similar to $T_{CDW}^{on}(p)$. Below $p \approx 0.08$, where there is no CDW order, $R_H(T)$ is flat at low T without any decrease, which is one of the reasons for the association of

[1] The zero field offset of R_{xy} is taken into account and does not affect the results.

T_{max} with the CDW [139]. $T_{max}(p)$ is also presented in the phase diagram for the 10 nm thick films on MgO in figure 7.8.

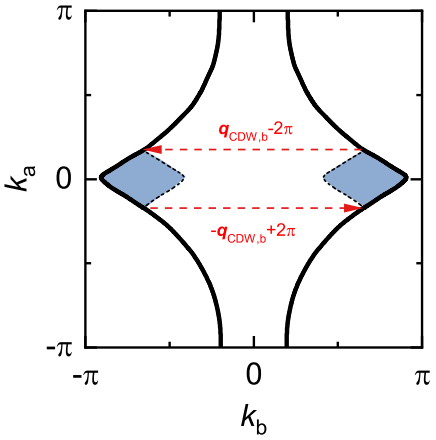

Figure 7.7: Illustration showing how a uniaxial CDW can reconstruct a nematic Fermi surface to small electron-like pockets through zone-folding. The picture is adapted from Ref. [130].

If we consider the commonly proposed scenario of FS reconstruction shown in figure 7.4 it is surprising that T_{max} and the shape of $R_H(T)$ does not depend on the thickness. This finding instead suggests that either a uniaxial CDW is responsible for the creation of the electron pocket, or that one has to come up with a completely different mechanism. Fermi surface reconstruction by a uniaxial CDW in YBCO has been extensively discussed in literature [67, 130, 138, 141]. A uniaxial CDW does not produce small electron pockets if one considers a nearly circular FS. However it does in the presence of a nematic distortion of the FS. The nematic distortion that has been considered in the theoretical proposals is similar to the one we have used to reproduce the large resistivity anisotropy in the 10 nm thick films, see figure 6.3. Figure 7.7 shows the possible electron pockets that are located in the anti-nodal direction close to (π,0) obtained by FS zone folding by a uniaxial CDW [130]. The strongly anisotropic FS in the 10 nm thick films might also explain the difference in magnitude of $R_H(T)$ in figure 7.6(a) [129].

7.3 Reshaped phase diagram

To conclude we put together all characteristic temperatures that we have extracted from transport measurements along the *a*- and *b*-axis in the 10 nm thick YBCO films and patterned Hall bar devices to construct the new phase diagram redesigned by strain. The modified phase diagram is presented in figure 7.8 and summarizes the results presented in this and the previous chapters. If we go from high to low T, the first characteristic temperature we encounter is T_L^a. It

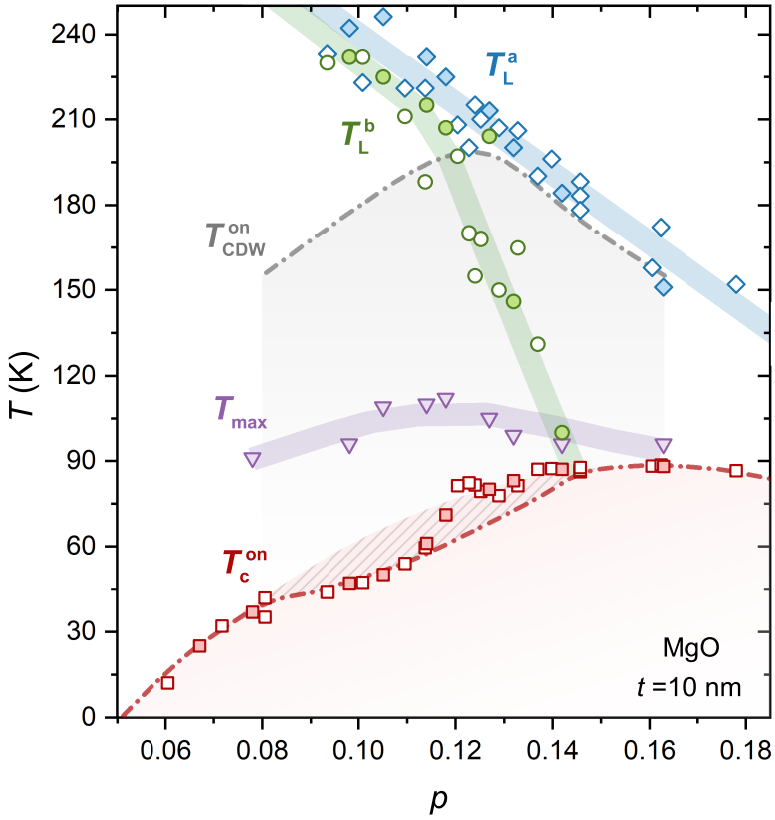

Figure 7.8: Phase diagram of 10 nm thick YBCO films. Open and filled symbols are from measurements of unpatterned films and patterned Hall bars respectively. The filled lines are guides for the eye. The red dash-dotted line shows T_c measured in relaxed YBCO thin films and crystals and the red striped area the suppression of T_c from parabolic p- dependence due to competition with the CDW order.

is approximately linear in doping with values close to what has been measured in crystals [127, 142]. T_L^b instead strongly deviates from the expected doping dependence when $p \gtrsim 0.11$ and is linear down to T_c at $p \approx 0.14$. The extension of the strange metal phase to lower temperatures can be connected to the uniaxial CDW, as we argued in chapter 6. The CDW onset temperature T_{CDW}^{on} is close to T_L^a for $p \gtrsim 0.11$, while it is much lower for doping levels $p < 0.11$[1]. The next characteristic temperature in the phase diagram is T_{max}. It has a dome-shape like doping dependence with a maximum at $p \approx 0.12$, similar to T_{CDW}^{on} [14]. The fact that there is no substantial difference in T_{max} and the shape of $R_H(T)$ in the 10 nm thick films compared to bulk YBCO [106, 139] points towards a scenario where the uniaxial CDW is mainly responsible for the Fermi surface reconstruction, or

[1] There are no recent RIXS measurements of the CDW order in YBCO thin films below $p \approx 0.12$, but we assume that the doping dependence is similar to that of single crystals [14] but shifted to higher T.

alternatively that a different mechanism has to be found to explain the quantum oscillation measurements. Finally, $T_c^{on}(p)$ follows the empirical parabolic dome down to $p \approx 0.12$, differently from thicker films and crystals where T_c is suppressed below $p \approx 0.14$ [17]. The increase of T_c^{on} is ascribed to the uniaxial CDW in the 10 nm thick films.

An interesting finding that comes from the phase diagram of figure 7.8 is that the doping range of strong anisotropy of T_L is the same as where we observe an increase of $T_c^{on,a}$. Previous studies have hinted that the nature of the CDW order and its impact on the properties of the cuprates is different below and above $p \approx 0.12$ [102]. If we assume that the CDW is uniaxial at all doping levels, it seems that it mostly affect the transport properties of the thin films only above this doping. This reinforces the picture where $p \approx 1/8$ is a special doping in the cuprate phase diagram.

8 Voltage switching in underdoped $YBa_2Cu_3O_{7-\delta}$ nanowires

Underdoped high T_c superconductor nanostructures are interesting from both a basic physics and applications point of view. This field is still a largely unexplored area of research because of the difficulty in preserving properties close to those of the bulk material in nanostructures. The ability to fabricate pristine HTS nanowires described in chapter 4 thus gives access to a variety of new experiments. In particular, one can investigate the intertwining of the various local electronic orders with superconductivity on the nanoscale. The characterization of underdoped nanowires with dimensions that are comparable to the length scales of the local orders could also help to clarify how they are related to the HTS phenomenon. Regarding applications, it is known that properties like the resistivity changes with doping. This can be utilized to improve the performance of devices. For example, an increased resistivity improves the flux noise properties of nanowire based superconducting quantum interference devices [143–145] and the sensitivity of superconducting nanowire based single photon detectors (SNSPDs) [146].

8.1 I-V characteristics of underdoped 50 nm thick nanowires

Figure 8.1(a) shows the current voltage (IV) characteristics measured at T=4.5 K of a bare 50 nm thick underdoped ($p \approx 0.13$) nanowire on MgO(110) (see figure 4.2 for the wire geometry). At the critical current I_c, where the nanowire enters the normal resistive state, there is a large hysteretic voltage switch followed by a linear increase of $V(I)$. The differential resistivity $\delta\rho = dV/dI \times A/l$, extracted from the linear $V(I)$ in the normal state, is close to the normal state resistivity above T_c ($\rho_N \approx 160$ $\mu\Omega$cm). This indicates that the full length of the nanowire has turned resistive. This kind of switching behavior is reminiscent of the formation of a so called hot spot in the nanowire [147]. When the bias current exceeds the local I_c in some part of the nanowire a normal state resistive region forms. The extent of the resistive region is determined by a balance between Joule heating which causes expansion of the hot spot and thermal relaxation which quenches it [146]. Hot spot formation is favourable in nanowires with high critical current that maximizes the

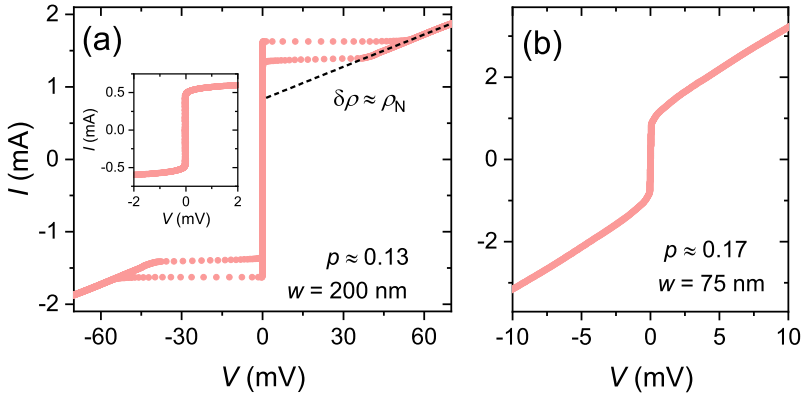

Figure 8.1: IV characteristics of 50 nm thick (a) underdoped ($p \approx 0.13$)and (b) slightly overdoped ($p \approx 0.17$) YBCO nanowires at $T \approx$4.5 K. The dashed line is a linear fit to the high voltage data and $\delta\rho$ the dynamical resistivity after the switch. The inset in (a) shows the IV characteristics of an underdoped nanowire with the same cross section but lower I_c.

Joule heating and low thermal conductivity which instead minimizes the thermal relaxation. Indeed, we only observe hysteretic voltage switches in devices with high J_c. The inset of figure 8.1(a) shows the IV characteristics of a nanowire with three times lower I_c (and the same cross-section) that has typical flux-flow behavior [110].

Normally, hysteretic voltage switching directly from the superconducting state is only observed in nanowires with extremely small cross-sections [94]. Figure 8.1(b) shows the IV characteristic typical of a 50 nm thick slightly overdoped nanowire that is only 75 nm wide; nevertheless it has flux-flow like behavior. Indeed, contrary to the underdoped nanowires, switching in slightly overdoped YBCO is only observed if the thickness of the nanowire is reduced to $\approx$ 10 nm [94, 148]. We attribute the different characteristics of the underdoped and slightly overdoped nanowires to a difference in the thermal conductivity. As we showed in figure 3.14, the resistivity in YBCO increases with decreasing doping. According to the Wiedemann-Franz law, which has recently been demonstrated to hold for underdoped cuprates [149], the thermal conductivity is inversely proportional to the resistivity ($\kappa = LT/\rho$, where $L = \pi^2 k_b^2/3e^2$ is the Lorenz number). Consequently, the conditions for stabilizing a hot spot are in principle much more favourable in underdoped nanowires [150].

Nanowires with IV characteristics similar to those of figure 8.1(a) (a sharp voltage switch that brings the wire directly from the superconducting to the resistive state) are commonly utilized for single photon detection [151]. In SNSPDs, the device is current biased close to I_c where a small perturbation, such as a photon hitting the device, can locally suppress the critical current and induce the voltage switch (through hot-spot formation) [146]. The energy of the photon has to be

much larger than the superconducting gap and the nanowire cross-section small for a single photon to be able to have impact on the superconducting properties of the device. When the nanowire turns resistive the bias current is redirected through an external load R_{L} (usually $\approx 50\Omega$) in a readout circuit which registers the photon event. To increase the area of the detector and thus the detection efficiency a SNSPD usually consists of multiple meandering nanowires in parallel.

At present, SNSPDs are commonly made from granular low T_{c} superconductors such as NbN. [146] The main reason comes from the relative ease to fabricate long nanowires of extremely small cross-section (which makes them sensitive to single photons) and high normal state resistance and J_{c} (which maximizes the current redistribution to the readout circuit), that are stable over time. Herein lies the problem in realizing HTS SNSPDs. The narrrow, and extremely thin, slightly overdoped YBCO nanowires that show hysteretic switching have problems with stability over time, and are very challenging to fabricate into the long meandering structures while maintaining a high J_{c} [152]. This problem might be less severe in the underdoped YBCO nanowires presented here. Because of their relatively large cross-sections it might be easier to realize long and stable structures, which makes them promising candidates for future application as SNSPDs. One would however need to optimize the nanowire dimensions and study how the voltage switching changes when the nanowire length is increased together with photoresponse measurements to further investigate their potential, which is outside the scope of this thesis work.

8.2 IV characteristics of 12 nm thick nanowires as a function of the doping

To further expand the investigation of the in-plane anisotropy of the transport properties of the very thin YBCO films discussed in chapter 6 and 7 we have patterned nanowires oriented along the *a*- and *b*-axis on 12 nm thick untwinned YBCO films grown on MgO(110) in a wide range of doping levels, using the procedure described in chapter 4. The nanowires were designed with five different widths w=65, 100, 200, 500 and 800 nm. The width gradually increases from the center towards the electrodes to reduce current crowding effects that can reduce I_{c} [111], see figure 8.2(a).

Typical IV characteristics of underdoped nanowires oriented along a and b are presented in figure 8.2(b) and (c). Along a the voltage increases smoothly above I_{c}. Along b instead there are multiple hysteretic voltage switches occurring at $I > I_{\mathrm{c}}$. This kind of anisotropic behavior is not present in slightly overdoped nanowires, see figure 8.2(d) and (e). Here, the typical IV characteristics include a single large hysteretic voltage switch in the normal state that is similar along both directions. There is also a significant difference in the magnitude of the voltage

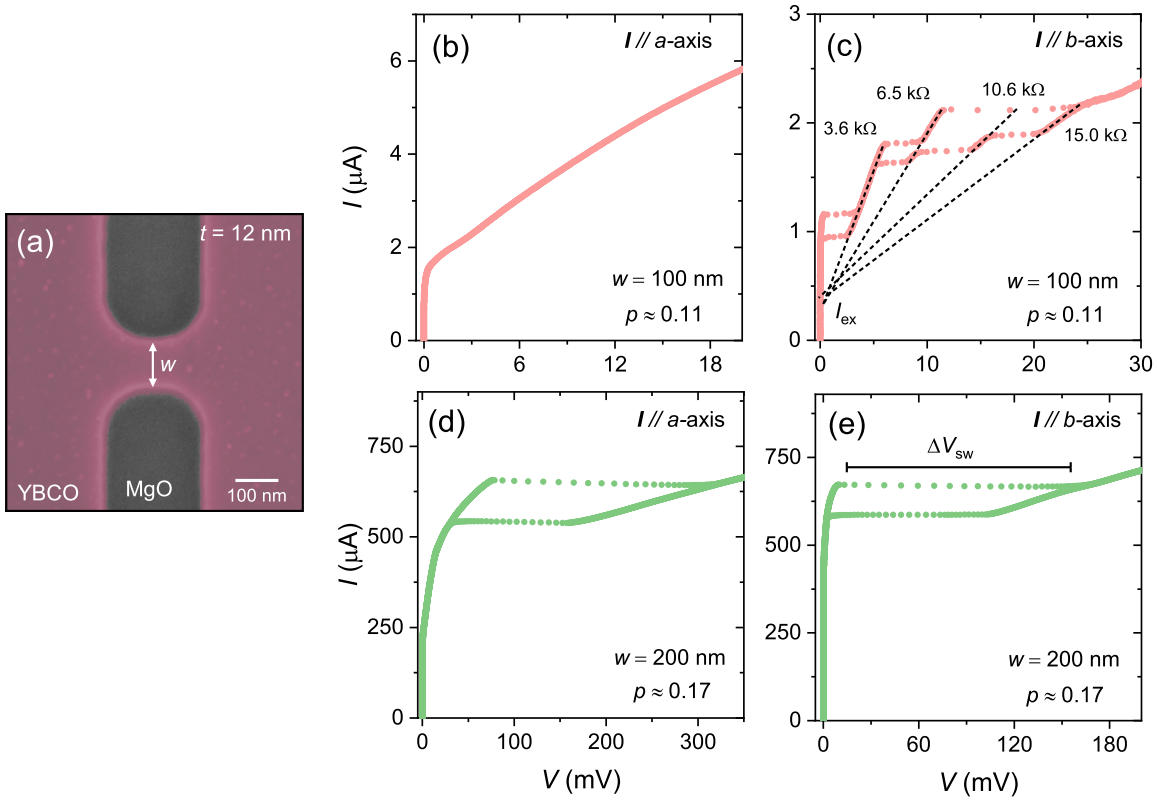

Figure 8.2: IV measurements in 12 nm thick YBCO nanowires at T=5 K. (a) False color SEM image showing the geometry of the nanowires. (b),(c) IV characteristics of 100 nm wide underdoped nanowires oriented along the a-axis and b-axis. (d),(e) IV characteristics of 200 nm slightly overdoped nanowires oriented along the a-axis and b-axis. The dashed lines in (c) are linear fits to the data following each voltage switch and the numbers are δR extracted from the fits. I_{ex} is where the dashed lines cross zero voltage.

switches in the underdoped ($\Delta V_{sw} \sim 5$ mV) and overdoped ($\Delta V_{sw} \sim 100$ mV) nanowires. This indicates that the mechanism responsible for the voltage switch is different at these two doping levels.

The step-like IV characteristics of the underdoped b-axis oriented nanowire (figure 8.2(c)), where each voltage switch adds a constant differential resistance $\delta R = dV/dI$ (black dashed lines), suggests that localized resistive regions are formed across the nanowire as the bias current is increased. The fact that ΔV_{sw} and the increase of δR is approximately equal at each switch, and that the excess current I_{ex} is the same for each resistive branch is suggestive of the appearance of phase-slips in the nanowires [153]. Phase-slip centers (PSC) have been used to describe voltage switching in one-dimensional ($w \ll \xi$) low T_c superconductor bridges. Figure 8.3 shows a simple model used to describe the phenomenon. When the current reaches the local I_c in some part of the nanowire, a PSC can form (associated to a slip of 2π of the superconducting order parameter). In

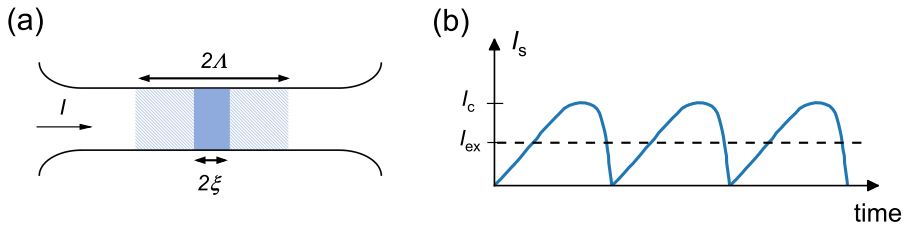

Figure 8.3: (a) Illustration of the PSC model in a nanowire. (b) Oscillations of the superconducting part of the current I_s in the PSC. I_{ex} is the average I_s through the PSC (dashed line). See the text for a description. Adapted from Ref. [153].

the PSC the supercurrent oscillates over time (where each period is accompanied by a phase-slip of 2π) in a region of length 2ξ. The resistive region extends to $\Lambda > \xi$ which represents the diffusion length of non-equilibrium quasi-particles. I_{ex} represents the average supercurrent through the phase-slip center, which is usually $\approx I_c/2$ [153]. The voltage difference across each phase-slip center can be estimated to

$$V = 2\Lambda\rho(I - I_{ex})/A \tag{8.1}$$

The PSC model has been shown to apply also to two-dimensional superconducting bridges where phase-slip centers are substituted by phase-slip lines [148, 154]. The exact relation between the two phase-slip phenomena is however not settled [155]. Equation 8.1 is perfectly compatible with the IV characteristics in figure 8.2(c) if we assume that $2\Lambda\rho/A = \delta R$ (so $V = \delta R(I - I_{ex})$) as we will elaborate below. The single large voltage switch in the slightly overdoped nanowires instead is not compatible with a pure phase-slip mechanism. The large ΔV_{sw} indicates that a significant volume of the nanowires is in the normal state after the switch. Since it occurs in the flux-flow normal state it possibly comes from vortex assisted hot-spot formation [156].

To learn more about the extent of the phase-slip lines/hot-spot regions we fabricated long nanowires with multiple voltage probes, see figure 8.4(a). Figure 8.4(b) shows the IV characteristics (measured between two adjacent voltage probes) of an underdoped nanowire. Since we can accurately determine the resistivity of the wire (see inset of figure 8.4(b)), we can use equation 8.1 to determine the quasi-particle diffusion length Λ. If we assume that $\rho = \rho_N \approx 0.7\text{m}\Omega\text{cm}$ we get $\Lambda \approx 15$ nm for the first switch in figure 8.4(b). This means that only part of the wire segment is resistive (the gap between the voltage probes is 50 nm). However, since we do not know the real temperature of the nanowire after the voltage switch $\Lambda \approx 15$ nm is only an upper estimation. Because of the upturn of ρ_b close to T_c (see inset of figure 8.4(b)) the resistivity is most likely higher than ρ_N after the switch (and therefore Λ smaller than we estimate).

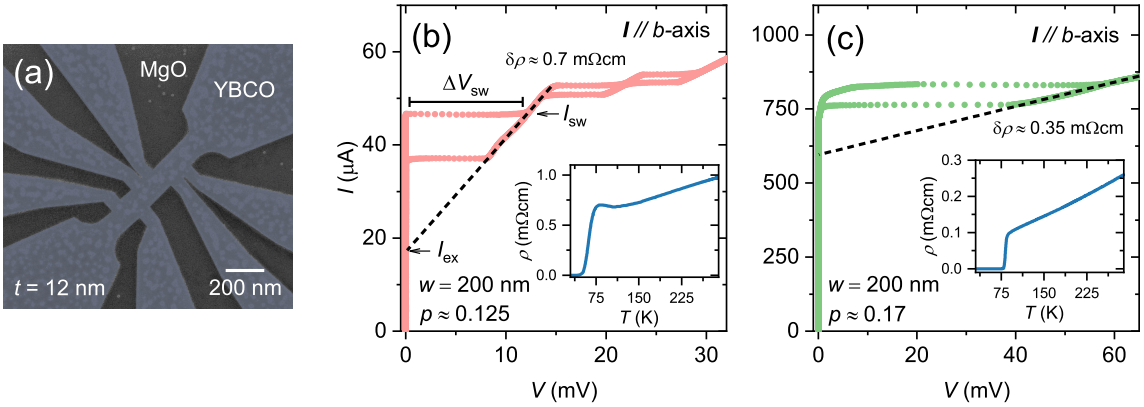

Figure 8.4: IV measurements in 12 nm thick YBCO nanowires with multiple voltage probes at T=5 K. (a) False color SEM image showing the geometry of the nanowires. IV characteristics of a 200 nm wide (b) underdoped ($p \approx 0.125$) nanowire and (c) slightly overdoped ($p \approx 0.17$) nanowire oriented along the b-axis. The measurements were done on a 50 nm wide segment between two adjacent voltage probes. The dashed lines are linear fits to the data following the voltage switch. The insets show $\rho(T)$ measurements of the same nanowires.

Figure 8.4(c) shows the IV characteristics of a similar, slightly overdoped nanowire. Here the differential resistivity $\delta\rho$ is much larger than the resistivity of the nanowire, even at room T. This indicates that the whole nanowire has turned resistive, which is supported by the fact that we observe the switch at the same current bias in adjacent segments of the nanowire. This is in contrast to the underdoped nanowire in figure 8.4(b) where the switches are localized in a single segment.

To gain more information on the voltage switching behavior and the a-b anisotropy in the underdoped nanowires we studied the doping dependence of the IV characteristics of a large number of wires (with the geometry shown in figure 8.2). Figure 8.5 summarizes the results. In figure 8.5(a), we present the fraction of the measured nanowires at each doping level which show hysteretic voltage switching (N_{sw}). This includes both the small switches in the underdoped nanowires and the large switches in the slightly overdoped nanowires. As anticipated in figure 8.2 most of the measured nanowires ($N_{sw} \approx 70\%$) do switch in the optimally doped/slightly overdoped regime (shaded region) and there is no significant difference in N_{sw} along a and b. Around $p \approx 0.16$ N_{sw} drops to ≈ 25 %, and for lower doping N_{sw} increases along b and decreases along a indicating a strong anisotropy between the two directions. In the strongly underdoped regime ($p \approx 0.08$) the anisotropy decreases again and only a small fraction of the wires show hysteretic switching behavior. The voltage switching amplitude (figure 8.5(b)) has a similar doping dependence. ΔV_{sw} strongly decreases when the doping is reduced, and in the underdoped regime ΔV_{sw} is larger in nanowires along b than along a.

Considering the doping dependence of N_{sw} and ΔV_{sw} there is a possible con-

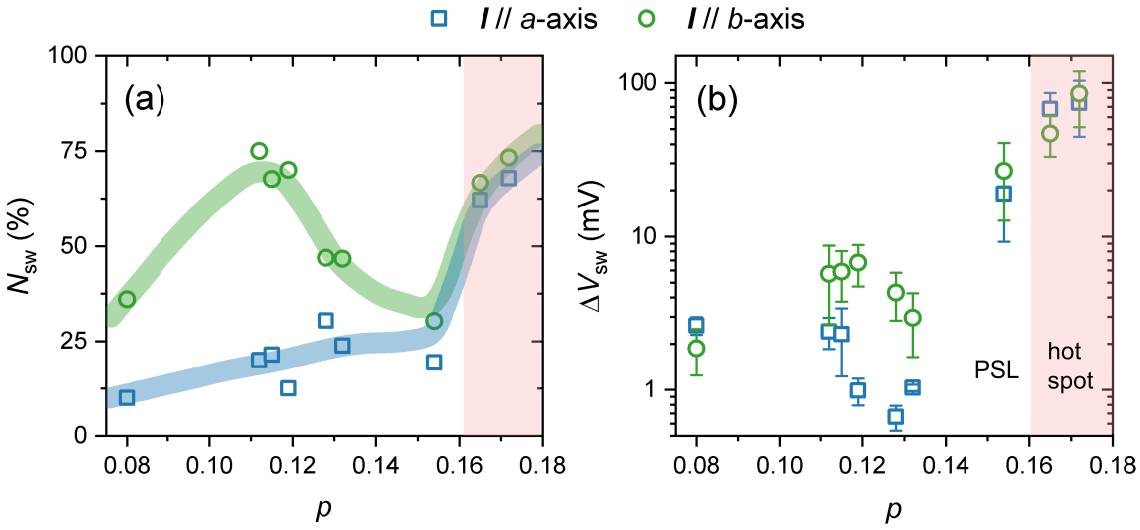

Figure 8.5: Doping dependence of the hysteretic voltage switching in 12nm thick YBCO nanowires. (a) Fraction of nanowires (N_{sw}) that show hysteretic voltage switching. Each point corresponds to $\approx$ 25 nanowires of varying width. (b) Average magniture of the hysteretic voltage switches (ΔV_{sw}). The error bars correspond to $\pm$ one standard deviation. There is less statistics for the wires along the a-axis since a smaller fraction showed switching behavior.

nection between the hysteretic voltage switch and the uniaxial CDW in the underdoped YBCO thin films. Along the b-axis, where the current is in the same direction as the CDW modulations, both N_{sw} and ΔV_{sw} peak close to $p = 1/8$ and drop of towards p=0.08 and p=0.16. Along the a-axis the doping dependence of these quantities is less significant. Since the CDW order and superconductivity are competing, one can imagine that the presence of CDW modulations in the nanowires can impact the IV characteristics and the transition from the superconducting to the normal state. The nature of the competition and its relevance for phase-slips is currently under investigation.

If we consider equation 8.1 the larger ΔV_{sw} (along b compared to a) at $p \approx 1/8$ should correspond to an increase of either I_c, ρ or Λ. Regarding the critical current, we see no significant trend of increase along b compared to along a in the underdoped regime. Figure 8.6 shows J_c versus doping for the 12 nm thick nanowires. The reduction of J_c with lower doping is expected and mainly comes from an increase of λ_L [153, 157]. The resistivity ρ on the other hand is strongly anisotropic in the YBCO thin films. As we showed in figure 7.1, $\rho_b < \rho_a$ at room temperature, but close to T_c there is an upturn in ρ_b which means that at $T \ll T_c$ ρ_b might be much larger than ρ_a. If we assume that the temperature of the nanowire is still much smaller than T_c for $I > I_c$ the large ρ_b can contribute to an increase of ΔV_{sw} and to the hysteresis of the switching through an increased Joule heating. This can however not be the sole explanation for the voltage

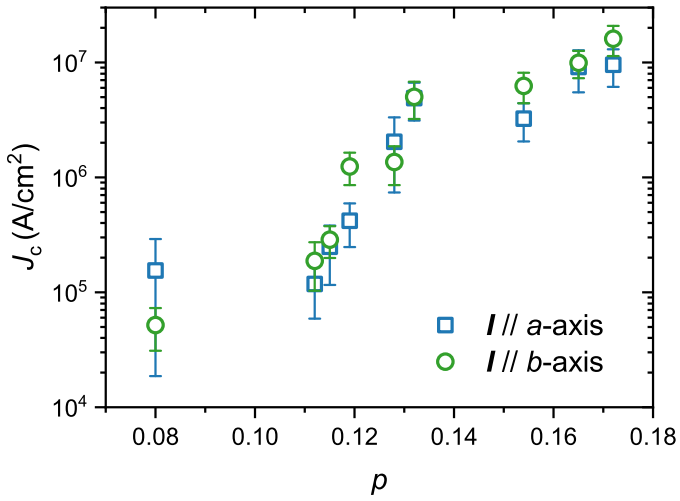

Figure 8.6: Average critical current density J_c at T=5 K versus doping for the 12 nm thick nanowires. Each point corresponds to $\approx$ 25 nanowires of varying width. The error bars correspond to $\pm$ one standard deviation.

switching, since at $p \approx 0.08$ where the anisotropy in ρ should be more significant we observe a less significant anisotropy in the switching behavior. The effects of the CDW modulations on Λ remains to be investigated. A possible scenario of the anisotropic switching behavior is shown in figure 8.7. Here, the *b*-axis oriented CDW modulations may act as weak spots orthogonal to the current (and the nanowire direction) which facilitates the formation of phase-slip lines across the nanowire width.

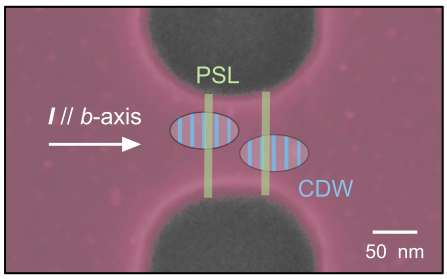

Figure 8.7: Sketch of hypothetical scenario where *b*-axis oriented CDW domains facilitate phase-slip lines (PSL) crossing the nanowire.

Finally, we should discuss the sudden decrease of N_{sw} and ΔV_{sw} at $p \approx 0.16$. Similarly to the underdoped regime, there is no sudden change of J_c in this interval of doping, see figure 8.6. There is also no indication of a dramatic change of ρ. These facts tend to to exclude scenarios where the decrease is due to a change of normal state heating properties of the nanowires. Studies have shown that the

quasiparticle relaxation time strongly decreases around this doping level [158], which possibly contributes to the different behaviors. Another possibility is that the quasiparticle properties are affected by the onset of CDW modulations at $p \approx 0.16$, which transforms the Fermi surface at low T, as discussed in chapter 7.

9 Summary and outlook

The main focus of the thesis work has been to study the structural and transport properties as a function of the doping in strained nm thick YBCO thin films and nanostructures.

The first part of the thesis has dealt with the development of the tools necessary for studying the YBCO material properties. We have demonstrated that our underdoped thin films, grown on MgO and STO substrates, reproduce the transport properties of single crystals, including the suppression of T_c around $p \approx 1/8$. The thin films can be made untwinned, which is instrumental for studying the anisotropic in-plane transport properties of the cuprates. We showed that a peculiar strain develops when the film thickness is reduced to the nanoscale, and that we are able to fabricate nanostructures that retain the properties of the bulk material. These results are an important first step in exploring the properties of strained nanoscale HTS structures and devices covering the whole underdoped side of the phase diagram. There are several promising future experiments which can help to disclose the microscopic mechanism of high T_c superconductivity.

In the second part of the thesis we make use of the thin film and nanostructure platform for various experiments concerning the transport properties of the HTS cuprates.

- We showed that the T-linear resistivity of strained, ultrathin YBCO films is extended to lower temperatures along the YBCO b-axis. We argued that this phenomenon is connected to the change of the CDW from biaxial to uniaxially directed along the YBCO b-axis, and to the presence of a strongly nematic Fermi surface. This finding points towards an intimate connection between the onset of CDW order and the breakdown of the strange metal linear resistivity in underdoped cuprates, a link that was missing until now. This has the potential to be an important piece in the puzzle of understanding the strange metal phase and its relevance for high-T_c superconductivity.
- We constructed the phase diagram for the strained, ultrathin YBCO films. The doping dependence of T_c was found to be different in the thin films compared to bulk YBCO in that it follows the empirical parabolic dome down to $p \approx 0.12$. We also found that the superconducting resistive transition is anisotropic where the strength of the CDW order is maximum. These

results are consequences of the competition between the uniaxial CDW and superconductivity. By measurements of the Hall coefficient we found that the Fermi surface reconstruction is of similar character in thick and thin films, even though the CDW order is uniaxial in the thin and biaxial in the thick films. This hints at an active role of the uniaxial CDW for the Fermi surface reconstruction. The reshaped phase diagram also highlighted the different impact of the CDW order on the transport properties above and below $p \approx 0.11$. The meaning of this special point of doping is unknown at the time. A future research direction is to focus on the strongly underdoped regime where also spin order plays a large role.

- We characterized the transport properties of underdoped YBCO nanowires through current-voltage measurements at low T. 50 nm thick nanowires show a single large voltage switch from the superconducting to the normal state, despite their relatively large cross-section. This makes them potential candidates for future application in single photon detectors. For 12 nm thick underdoped nanowires instead we found that the transport properties along the two in-plane directions are very different. Along the b-axis, which is the direction of the uniaxial CDW modulations, the transition from the superconducting to the normal state is characterized by the appearance of phase-slips. The amplitude of the phase-slip voltage scales with the CDW strength, which points towards an entanglement between the two phenomena. Further analysis of these results can lead to a better understanding of the competition and intertwining of the CDW and superconducting order.

To conclude, we will elaborate on possible future research directions.

In this thesis we have mostly focused on the underdoped region of the phase diagram. There is however a lot left to explore in the strongly underdoped and overdoped regime.

- As we showed in figure 7.1, the resistivity along the YBCO b-axis in the 10 nm thick has an upturn close to T_c for $p \lesssim 1/8$. In crystals this insulating-like behaviour has only been observed at much lower doping ($p < 0.08$) [139], and along both in-plane axes [86, 104]. $p \approx 0.08$ is a special doping level in YBCO since it is where the CDW order ends from the high doping side and the SDW order ends from the low doping side (see the phase diagram of figure 2.3). The insulating like behaviour for $p < 0.08$ is therefore commonly associated to the presence of these local orders [86, 139, 159]. In the strained 10 nm thick untwinned films we observe a dramatically different behaviour. Figure 9.1(a) shows the $\rho(T)$ along both in-plane axes of a film with $p \approx 0.07$. Here, the resistivity along b is larger than along a in the full temperature range

and is strongly insulating-like at low T. This result indicates that we are able to tune the ground state also in the spin order regime. High magnetic field measurements which suppress superconductivity to 0 K could help to identify the insulating state.

- In the slightly overdoped regime we also observe different resistivity behaviour in the 10 nm thick films compared to the thicker ones. In the 50 nm thick films (see figure 3.14(a)) ρ_a deviates upwards from the T-linear behaviour at T_{coh}. In contrast, the ρ_a measured in a 10 nm thick slightly overdoped film in figure 9.1(b) shows a downward deviation at $T_L \approx 150$ K, similarly to the underdoped case. This different behaviour in the thick and thin films can possibly be related to the increase of the unit cell volume in the 10 nm thin film, as we discussed in section 3.3. Further investigations in the overdoped regime could lead to a better understanding of the strange metal behaviour close to the putative critical point at p^*.

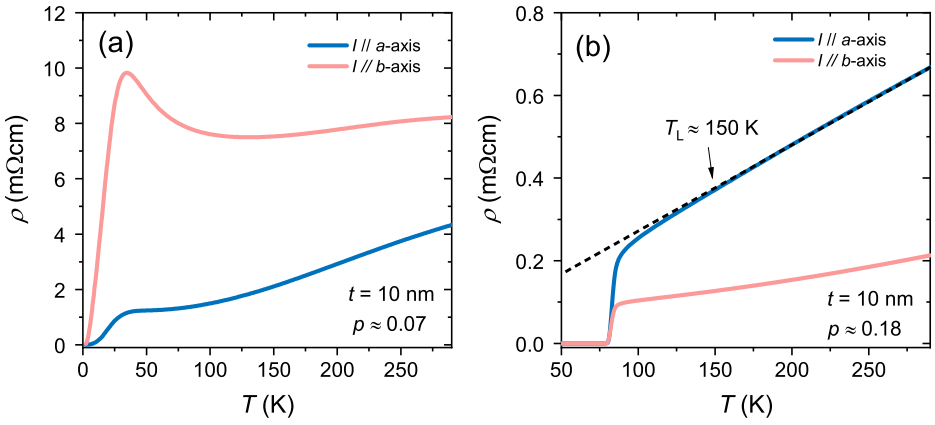

Figure 9.1: Resistivity measurements along the a- and b-axis of 10 nm thick untwinned YBCO films on MgO. (a) $p \approx 0.07$ (b) $p \approx 0.18$

Finally, the underdoped nanowires presented in chapters 4 and 8 shows promise for both new understanding of HTS physics and applications. Since this is a largely unexplored research area there are many possible directions to explore. We already discussed the potential of the underdoped nanowires for future application in single photon detectors. A thorough optimization of the nanowire dimensions to increase the amplitude of the voltage switch can be the next step in this direction.

Another example is the realization of HTS single electron transistors, which could be used to map the symmetry and doping dependence of a fully gapped superconducting order parameter [160].

Appendices

Appendix A

Nanowire fabrication process parameters

What follows is a description of the cleanroom fabrication process that has been used to obtain the microbars/nanowires shown in the main text of the thesis. The process is already partly described in figure 4.1.

1. A 10-50 nm thick YBCO film is deposited by PLD on one of the substrates described in chapter 3. Typical deposition parameters are presented in table 3.1.

2. 25 nm thick Au is sputtered through a metal mask to define an area of the sample for electrical contact pads.

3. An 80-100 nm thick amorphous C film is deposited by PLD on top of the YBCO film. The deposition is done at room temperature with an Ar background pressure $3.4{\cdot}10^{-4}$. The laser energy is ramped up in steps from 60 to 110 mJ to increase adhesion. The laser spot size is $\approx$ 4 mm.

4. A double layer of e-beam resist is spin coated on the C surface. The bottom layer is MCC NANO Copolymer EL4 and the top layer ARP6200.13:Anisol 1:2. Both are spin coated at 6000 rpm for 60 seconds and baked at 90° for 5 minutes on a hot plate.

5. The film is exposed by a 100kV e-beam lithography system (JEOL JBX 9300 FS) in a pattern defined by a CAD mask. A beam current of 1nA is used for small structures and 35nA for large ones.

6. The resist is developed for 40 seconds in O-Oxylene 95% (top layer) followed by 35 seconds in MIBK:IPA 1:3 (bottom layer). The sample is then etched 5 seconds in 50 W oxygen RIE plasma to remove resist residues.

7. A 10 nm thick Cr metal mask is e-beam evaporated at a rate of 1 Å/s on the sample.

8. The Cr mask is lift-off by leaving it in 60° remover 1165 for 10 minutes.

9. The carbon not protected by Cr is etched for 25 minutes in a 50 W oxygen RIE plasma at 100mbar oxygen pressure.

10. The YBCO that is not protected by the remaining C mask is etched by Ar ion milling on a LN2 cooled stage. The voltage and current are set very low (300V, 2mA ($\approx 30\mu A/cm^2$)) to minimize heating of the film. The background pressure during the process is $\approx 1 \cdot 10^{-4}$mbar. A neutralizer is used to minimize charging of the sample. The etching time varies from 50-150 minutes depending on the film thickness.

11. The remaining C on top of the YBCO structures is etched by a low power (15W) oxygen RIE plasma at 100mbar oxygen pressure.

References

[1] J. G. Bednorz and K. A. Müller, "Possible high T_c superconductivity in the Ba-La-Cu-O system", *Zeitschrift für Physik B Condensed Matter* **64**, 189–193 (1986).

[2] B. Keimer, S. A. Kivelson, M. R. Norman, S. Uchida, and J Zaanen, "From quantum matter to high-temperature superconductivity in copper oxides", *Nature* **518**, 179–186 (2015).

[3] S Martin, A. T. Fiory, R. Fleming, L. Schneemeyer, and J. V. Waszczak, "Normal-state transport properties of $Bi_{2+x}Sr_{2-y}CuO_{6+\delta}$ crystals", *Phys. Rev. B* **41**, 846 (1990).

[4] J. Bruin, H Sakai, R. Perry, and A. Mackenzie, "Similarity of scattering rates in metals showing T-linear resistivity", *Science* **339**, 804–807 (2013).

[5] S Kasahara, T Shibauchi, K. Hashimoto, K Ikada, S Tonegawa, R Okazaki, H Shishido, H Ikeda, H Takeya, K Hirata, et al., "Evolution from non-Fermi-to Fermi-liquid transport via isovalent doping in $BaFe_2(As_{1-x}P_x)_2$ superconductors", *Phys. Rev. B* **81**, 184519 (2010).

[6] Y. Cao, V. Fatemi, A. Demir, S. Fang, S. L. Tomarken, J. Y. Luo, J. D. Sanchez-Yamagishi, K. Watanabe, T. Taniguchi, E. Kaxiras, et al., "Correlated insulator behaviour at half-filling in magic-angle graphene superlattices", *Nature* **556**, 80–84 (2018).

[7] S. Sachdev, *Quantum phase transitions* (Cambridge university press, 2011).

[8] C Castellani, C Di Castro, and M Grilli, "Singular quasiparticle scattering in the proximity of charge instabilities", *Phys. Rev. Lett.* **75**, 4650 (1995).

[9] T. Timusk and B. Statt, "The pseudogap in high-temperature superconductors: an experimental survey", *Rep. Prog. Phys.* **62**, 61 (1999).

[10] G Ghiringhelli, M Le Tacon, M. Minola, S Blanco-Canosa, C. Mazzoli, N. Brookes, G. De Luca, A Frano, D. Hawthorn, F He, et al., "Long-range incommensurate charge fluctuations in (Y, Nd)$Ba_2Cu_3O_{6+x}$", *Science* **337**, 821–825 (2012).

[11] Y Sato, S Kasahara, H Murayama, Y Kasahara, E.-G. Moon, T Nishizaki, T Loew, J Porras, B Keimer, T Shibauchi, et al., "Thermodynamic evidence for a nematic phase transition at the onset of the pseudogap in $YBa_2Cu_3O_y$", *Nat. Phys.* **13**, 1074–1078 (2017).

[12] J. Tranquada, B. Sternlieb, J. Axe, Y Nakamura, and S Uchida, "Evidence for stripe correlations of spins and holes in copper oxide superconductors", *Nature* **375**, 561–563 (1995).

[13] B Fauqué, Y. Sidis, V Hinkov, S Pailhes, C. Lin, X. Chaud, and P. Bourges, "Magnetic order in the pseudogap phase of high-T_c superconductors", *Phys. Rev. Lett.* **96**, 197001 (2006).

[14] S Blanco-Canosa, A Frano, E Schierle, J Porras, T Loew, M Minola, M Bluschke, E Weschke, B Keimer, and M Le Tacon, "Resonant x-ray scattering study of charge-density wave correlations in $YBa_2Cu_3O_{6+x}$", *Phys. Rev. B* **90**, 054513 (2014).

[15] J Chang, E. Blackburn, A. Holmes, N. B. Christensen, J. Larsen, J Mesot, R. Liang, D. Bonn, W. Hardy, A Watenphul, et al., "Direct observation of competition between superconductivity and charge density wave order in $YBa_2Cu_3O_{6.67}$", *Nat. Phys.* **8**, 871–876 (2012).

[16] Y. Ando, S. Komiya, K. Segawa, S Ono, and Y Kurita, "Electronic phase diagram of high-T_c cuprate superconductors from a mapping of the in-plane resistivity curvature", *Phys. Rev. Lett.* **93**, 267001 (2004).

[17] R. Liang, D. Bonn, and W. Hardy, "Evaluation of CuO_2 plane hole doping in $YBa_2Cu_3O_{6+x}$ single crystals", *Phys. Rev. B* **73**, 180505 (2006).

[18] N. Doiron-Leyraud, C. Proust, D. LeBoeuf, J. Levallois, J.-B. Bonnemaison, R. Liang, D. Bonn, W. Hardy, and L. Taillefer, "Quantum oscillations and the Fermi surface in an underdoped high-T_c superconductor", *Nature* **447**, 565–568 (2007).

[19] S. E. Sebastian, N. Harrison, and G. G. Lonzarich, "Towards resolution of the Fermi surface in underdoped high-T_c superconductors", *Rep. Prog. Phys.* **75**, 102501 (2012).

[20] C. Proust and L. Taillefer, "The remarkable underlying ground states of cuprate superconductors", *Annu. Rev. Condens. Matter Phys.* **10**, 409–429 (2019).

[21] E. Fradkin, S. A. Kivelson, and J. M. Tranquada, "Colloquium: Theory of intertwined orders in high temperature superconductors", *Rev. Mod. Phys.* **87**, 457 (2015).

[22] T. Wu, H. Mayaffre, S. Krämer, M. Horvatić, C. Berthier, W. Hardy, R. Liang, D. Bonn, and M.-H. Julien, "Incipient charge order observed by NMR in the normal state of $YBa_2Cu_3O_y$", *Nat. Commun.* **6**, 1–9 (2015).

[23] O Cyr-Choinière, D LeBoeuf, S. Badoux, S Dufour-Beauséjour, D. Bonn, W. Hardy, R Liang, D Graf, N Doiron-Leyraud, and L. Taillefer, "Sensitivity of T_c to pressure and magnetic field in the cuprate superconductor $YBa_2Cu_3O_y$: Evidence of charge-order suppression by pressure", *Phys. Rev. B* **98**, 064513 (2018).

[24] S. Souliou, H Gretarsson, G Garbarino, A Bosak, J Porras, T Loew, B Keimer, and M Le Tacon, "Rapid suppression of the charge density wave in $YBa_2Cu_3O_{6.6}$ under hydrostatic pressure", *Phys. Rev. B* **97**, 020503 (2018).

[25] H.-H. Kim, S. Souliou, M. Barber, E Lefrançois, M Minola, M Tortora, R Heid, N Nandi, R. A. Borzi, G Garbarino, et al., "Uniaxial pressure control of competing orders in a high-temperature superconductor", *Science* **362**, 1040–1044 (2018).

[26] M Bluschke, A Frano, E Schierle, D Putzky, F Ghorbani, R Ortiz, H Suzuki, G Christiani, G Logvenov, E Weschke, et al., "Stabilization of three-dimensional charge order in $YBa_2Cu_3O_{6+x}$ via epitaxial growth", *Nat. Commun.* **9**, 1–8 (2018).

[27] M. Huecker, N. B. Christensen, A. Holmes, E. Blackburn, E. M. Forgan, R. Liang, D. Bonn, W. Hardy, O. Gutowski, M. v. Zimmermann, et al., "Competing charge, spin, and superconducting orders in underdoped $YBa_2Cu_3O_y$", *Phys. Rev. B* **90**, 054514 (2014).

[28] J. Bonetti, D. Caplan, D. Van Harlingen, and M. Weissman, "Electronic Transport in Underdoped $YBa_2Cu_3O_{7-\delta}$ Nanowires: Evidence for Fluctuating Domain Structures", *Phys. Rev. Lett.* **93**, 087002 (2004).

[29] F. Carillo, G. M. De Luca, D. Montemurro, G. Papari, M. Salluzzo, D. Stornaiuolo, F. Tafuri, and F. Beltram, "Coherent transport in extremely underdoped $Nd_{1.2}Ba_{1.8}Cu_3O_z$ nanostructures", *New J. Phys.* **14**, 083025 (2012).

[30] H Kamerlingh Onnes, "The resistance of pure mercury at helium temperatures", *Commun. Phys. Lab. Univ. Leiden* **120** (1911).

[31] W. Meissner and R. Ochsenfeld, "Ein neuer effekt bei eintritt der supraleitfähigkeit", *Naturwissenschaften* **21**, 787–788 (1933).

[32] F. London and H. London, "The electromagnetic equations of the supraconductor", *Proc. R. Soc. Lond. A Math. Phys. Sci.* **149**, 71–88 (1935).

[33] L. D. Landau and V. L. Ginzburg, "On the theory of superconductivity", *Zh. Eksp. Teor. Fiz.* **20**, 1064 (1950).

[34] A. A. Abrikosov, "On the magnetic properties of superconductors of the second group", *Sov. Phys. JETP* **5**, 1174–1182 (1957).

[35] J. R. Waldram, *Superconductivity of metals and cuprates* (CRC Press, 2017).

[36] J. Bardeen, L. N. Cooper, and J. R. Schrieffer, "Theory of superconductivity", *Phys. Rev.* **108**, 1175 (1957).

[37] J. Gavaler, "Superconductivity in Nb-Ge films above 22 K", *Appl. Phys. Lett.* **23**, 480–482 (1973).

[38] H. Maeda, Y. Tanaka, M. Fukutomi, and T. Asano, "A new high-T_c oxide superconductor without a rare earth element", *Jpn. J. Appl. Phys.* **27**, L209 (1988).

[39] G Grissonnanche, O Cyr-Choinière, F. Laliberté, S. R. De Cotret, A Juneau-Fecteau, S Dufour-Beauséjour, M.-E. Delage, D LeBoeuf, J Chang, B. Ramshaw, et al., "Direct measurement of the upper critical field in cuprate superconductors", *Nat. Commun.* **5**, 1–8 (2014).

[40] D. J. Van Harlingen, "Phase-sensitive tests of the symmetry of the pairing state in the high-temperature superconductors - Evidence for $d_{x^2-y^2}$ symmetry", *Rev. Mod. Phys.* **67**, 515 (1995).

[41] R. Cava, A. Hewat, E. Hewat, B Batlogg, M Marezio, K. Rabe, J. Krajewski, W. Peck Jr, and L. Rupp Jr, "Structural anomalies, oxygen ordering and superconductivity in oxygen deficient $Ba_2YCu_3O_x$", *Physica C* **165**, 419–433 (1990).

[42] J. Zaanen, S. Chakravarty, T Senthil, P. Anderson, P. Lee, J. Schmalian, M. Imada, D. Pines, M. Randeria, C. Varma, et al., "Towards a complete theory of high T_c", *Nat. Phys.* **2**, 138–143 (2006).

[43] J. Jorgensen, B. Veal, A. P. Paulikas, L. Nowicki, G. Crabtree, H Claus, and W. Kwok, "Structural properties of oxygen-deficient $YBa_2Cu_3O_{7-\delta}$", *Phys. Rev. B* **41**, 1863 (1990).

[44] W. E. Pickett, "Electronic structure of the high-temperature oxide superconductors", *Rev. Mod. Phys.* **61**, 433 (1989).

[45] A. A. Abrikosov, *Fundamentals of the Theory of Metals* (Courier Dover Publications, 2017).

[46] A Legros, S Benhabib, W. Tabis, F Laliberté, M Dion, M Lizaire, B. Vignolle, D. Vignolles, H Raffy, Z. Li, et al., "Universal T-linear resistivity and Planckian dissipation in overdoped cuprates", *Nat. Phys.* **15**, 142–147 (2019).

[47] R. Cooper, Y Wang, B. Vignolle, O. Lipscombe, S. Hayden, Y. Tanabe, T Adachi, Y. Koike, M. Nohara, H Takagi, et al., "Anomalous criticality in the electrical resistivity of $La_{2-x}Sr_xCuO_4$", *Science* (2009).

[48] B Bucher, P Steiner, J Karpinski, E Kaldis, and P Wachter, "Influence of the spin gap on the normal state transport in $YBa_2Cu_4O_8$", *Phys. Rev. Lett.* **70**, 2012 (1993).

[49] A. Ioffe and A. Regel, "Non-crystalline, amorphous and liquid electronic semiconductors", *Prog. Semicond* **4**, 237–291 (1960).

[50] A Kaminski, S Rosenkranz, H. Fretwell, Z. Li, H Raffy, M Randeria, M. Norman, and J. Campuzano, "Crossover from Coherent to Incoherent Electronic Excitations in the Normal State of $Bi_2Sr_2CaCu_2O_{8+\delta}$", *Phys. Rev. Lett.* **90**, 207003 (2003).

[51] K Takenaka, J Nohara, R Shiozaki, and S Sugai, "Incoherent charge dynamics of $La_{2-x}Sr_xCuO_4$: dynamical localization and resistivity saturation", *Phys. Rev. B* **68**, 134501 (2003).

[52] G. Seibold, R. Arpaia, Y. Y. Peng, R. Fumagalli, L. Braicovich, C. Di Castro, M. Grilli, G. C. Ghiringhelli, and S. Caprara, "Strange metal behaviour from charge density fluctuations in cuprates", *Commun. Phys.* **4**, 1–6 (2021).

[53] B Michon, C Girod, S. Badoux, J Kačmarčík, Q Ma, M Dragomir, H. Dabkowska, B. Gaulin, J.-S. Zhou, S Pyon, et al., "Thermodynamic signatures of quantum criticality in cuprate superconductors", *Nature* **567**, 218–222 (2019).

[54] B. Ramshaw, S. Sebastian, R. McDonald, J. Day, B. Tan, Z Zhu, J. Betts, R. Liang, D. Bonn, W. Hardy, et al., "Quasiparticle mass enhancement approaching optimal doping in a high-T_c superconductor", *Science* **348**, 317–320 (2015).

[55] J. Zaanen, "Planckian dissipation, minimal viscosity and the transport in cuprate strange metals", *SciPost Phys.* **6**, 061 (2019).

[56] S Nakamae, K Behnia, N Mangkorntong, M Nohara, H Takagi, S. Yates, and N. Hussey, "Electronic ground state of heavily overdoped nonsuperconducting $La_{2-x}Sr_xCuO_4$", *Phys. Rev. B* **68**, 100502 (2003).

[57] D. Marshall, D. Dessau, A. Loeser, C. Park, A. Matsuura, J. Eckstein, I Bozovic, P Fournier, A Kapitulnik, W. Spicer, et al., "Unconventional electronic structure evolution with hole doping in $Bi_2Sr_2CaCu_2O_{8+\delta}$: Angle-resolved photoemission results", *Phys. Rev. Lett.* **76**, 4841 (1996).

[58] M. Hashimoto, I. M. Vishik, R.-H. He, T. P. Devereaux, and Z.-X. Shen, "Energy gaps in high-transition-temperature cuprate superconductors", *Nat. Phys.* **10**, 483–495 (2014).

[59] H Takagi, B Batlogg, H. Kao, J Kwo, R. J. Cava, J. Krajewski, and W. Peck Jr, "Systematic evolution of temperature-dependent resistivity in $La_{2-x}Sr_xCuO_4$", *Phys. Rev. Lett.* **69**, 2975 (1992).

[60] T Ito, K Takenaka, and S.-i. Uchida, "Systematic deviation from T-linear behavior in the in-plane resistivity of $YBa_2Cu_3O_{7-y}$: Evidence for dominant spin scattering", *Phys. Rev. Lett.* **70**, 3995 (1993).

[61] S. Badoux, W. Tabis, F Laliberté, G Grissonnanche, B. Vignolle, D. Vignolles, J. Béard, D. Bonn, W. Hardy, R Liang, et al., "Change of carrier density at the pseudogap critical point of a cuprate superconductor", *Nature* **531**, 210–214 (2016).

[62] P. Monceau, "Electronic crystals: an experimental overview", *Adv. Phys.* **61**, 325–581 (2012).

[63] J Chang, E Blackburn, O Ivashko, A. Holmes, N. B. Christensen, M Hücker, R. Liang, D. Bonn, W. Hardy, U Rütt, et al., "Magnetic field controlled charge density wave coupling in underdoped $YBa_2Cu_3O_{6+x}$", *Nat. Commun.* **7**, 1–7 (2016).

[64] M. E. Barber, H.-h. Kim, T. Loew, M. L. Tacon, M. Minola, M. Konczykowski, B. Keimer, A. P. Mackenzie, and C. W. Hicks, "Suppression of superconductivity by charge density wave order in $YBa_2Cu_3O_{6.67}$", *arXiv preprint arXiv:2101.02923* (2021).

[65] D. LeBoeuf, N. Doiron-Leyraud, J. Levallois, R. Daou, J.-B. Bonnemaison, N. Hussey, L. Balicas, B. Ramshaw, R. Liang, D. Bonn, et al., "Electron pockets in the Fermi surface of hole-doped high-T_c superconductors", *Nature* **450**, 533–536 (2007).

[66] A. J. Millis and M. Norman, "Antiphase stripe order as the origin of electron pockets observed in 1/8-hole-doped cuprates", *Phys. Rev. B* **76**, 220503 (2007).

[67] N Harrison and S. Sebastian, "Fermi surface reconstruction from bilayer charge ordering in the underdoped high temperature superconductor $YBa_2Cu_3O_{6+x}$", *New J. Phys.* **14**, 095023 (2012).

[68] R Arpaia, S Caprara, R Fumagalli, G De Vecchi, Y. Peng, **E. Andersson**, D Betto, G. De Luca, N. Brookes, F Lombardi, et al., "Dynamical charge density fluctuations pervading the phase diagram of a Cu-based high-T_c superconductor", *Science* **365**, 906–910 (2019).

[69] J. Tranquada, D. Cox, W Kunnmann, H Moudden, G Shirane, M Suenaga, P Zolliker, D Vaknin, S. Sinha, M. Alvarez, et al., "Neutron-Diffraction Determination of Antiferromagnetic Structure of Cu Ions in $YBa_2Cu_3O_{6+x}$ with x= 0.0 and 0.15", *Phys. Rev. Lett.* **60**, 156 (1988).

[70] F Coneri, S. Sanna, K Zheng, J Lord, and R De Renzi, "Magnetic states of lightly hole-doped cuprates in the clean limit as seen via zero-field muon spin spectroscopy", *Phys. Rev. B* **81**, 104507 (2010).

[71] V Hinkov, D Haug, B Fauqué, P Bourges, Y. Sidis, A Ivanov, C. Bernhard, C. Lin, and B Keimer, "Electronic liquid crystal state in the high-temperature superconductor $YBa_2Cu_3O_{6.45}$", *Science* **319**, 597–600 (2008).

[72] D. Haug, V. Hinkov, Y. Sidis, P. Bourges, N. B. Christensen, A. Ivanov, T. Keller, C. Lin, and B. Keimer, "Neutron scattering study of the magnetic phase diagram of underdoped $YBa_2Cu_3O_{6+x}$", *New J. Phys.* **12**, 105006 (2010).

[73] C. Niedermayer, C Bernhard, T Blasius, A Golnik, A Moodenbaugh, and J. Budnick, "Common phase diagram for antiferromagnetism in $La_{2-x}Sr_xCuO_4$ and $Y_{1-x}Ca_xBa_2Cu_3O_6$ as seen by muon spin rotation", *Phys. Rev. Lett.* **80**, 3843 (1998).

[74] M Fujita, H Goka, K Yamada, J. Tranquada, and L. Regnault, "Stripe order, depinning, and fluctuations in $La_{1.875}Ba_{0.125}CuO_4$ and $La_{1.875}Ba_{0.075}Sr_{0.050}CuO_4$", *Phys. Rev. B* **70**, 104517 (2004).

[75] Q Li, M Hücker, G. Gu, A. Tsvelik, and J. Tranquada, "Two-dimensional superconducting fluctuations in stripe-ordered $La_{1.875}Ba_{0.125}CuO_4$", *Phys. Rev. Lett.* **99**, 067001 (2007).

[76] D. F. Agterberg, J. S. Davis, S. D. Edkins, E. Fradkin, D. J. Van Harlingen, S. A. Kivelson, P. A. Lee, L. Radzihovsky, J. M. Tranquada, and Y. Wang, "The physics of pair-density waves: cuprate superconductors and beyond", *Annu. Rev. Condens. Matter Phys.* **11**, 231–270 (2020).

[77] S. D. Edkins, A. Kostin, K. Fujita, A. P. Mackenzie, H. Eisaki, S Uchida, S. Sachdev, M. J. Lawler, E.-A. Kim, J. S. Davis, et al., "Magnetic field–induced pair density wave state in the cuprate vortex halo", *Science* **364**, 976–980 (2019).

[78] D. J. Scalapino, "A common thread: The pairing interaction for unconventional superconductors", *Rev. Mod. Phys.* **84**, 1383 (2012).

[79] P. W. Anderson, "The Resonating Valence Bond State in La_2CuO_4 and Superconductivity", *Science* **235**, 1196–1198 (1987).

[80] S. A. Kivelson, I. P. Bindloss, E. Fradkin, V. Oganesyan, J. Tranquada, A. Kapitulnik, and C. Howald, "How to detect fluctuating stripes in the high-temperature superconductors", *Rev. Mod. Phys.* **75**, 1201 (2003).

[81] H Sato, A Tsukada, M Naito, and A Matsuda, "$La_{2-x}Sr_xCuO_y$ epitaxial thin films (x= 0 to 2): Structure, strain, and superconductivity", *Phys. Rev. B* **61**, 12447 (2000).

[82] R. Baghdadi, R. Arpaia, T. Bauch, and F. Lombardi, "Toward YBCO Nanoscale Structures for Hybrid Devices", *IEEE Trans. Appl. Supercond.* **25**, 1–4 (2014).

[83] F. Lombardi, Z. Ivanov, G. Fischer, E Olsson, and T Claeson, "Transport and structural properties of the top and bottom grain boundaries in $YBa_2Cu_3O_{7-\delta}$ step-edge Josephson junctions", *Appl. Phys. Lett.* **72**, 249–251 (1998).

[84] G Chern, J. Huang, and T. Leung, "Atomic force microscopy study of the faceting on MgO (110) surface", *J. Vac. Sci. Technol A* **16**, 964–967 (1998).

[85] L. J. van der Pauw, "A method of measuring the resistivity and Hall coefficient on lamellae of arbitrary shape", *Philips technical review* **20**, 220–224 (1958).

[86] Y. Ando, K. Segawa, S. Komiya, and A. Lavrov, "Electrical resistivity anisotropy from self-organized one dimensionality in high-temperature superconductors", *Phys. Rev. Lett.* **88**, 137005 (2002).

[87] R. Gagnon, C. Lupien, and L. Taillefer, "T^2 dependence of the resistivity in the Cu-O chains of $YBa_2Cu_3O_{6.9}$", *Phys. Rev. B* **50**, 3458 (1994).

[88] J Zegenhagen, T Haage, and Q. Jiang, "Microscopic structure and structuring of perovskite surfaces and interfaces: $SrTiO_3$, $RBa_2Cu_3O_{7-\delta}$", *Appl. Phys. A* **67**, 711–722 (1998).

[89] J. M. Dekkers, G. Rijnders, S. Harkema, H. J. H. Smilde, H. Hilgenkamp, H. Rogalla, and D. H. Blank, "Monocrystalline $YBa_2Cu_3O_{7-x}$ thin films on vicinal $SrTiO_3$ (001) substrates", *Appl. Phys. Lett.* **83**, 5199–5201 (2003).

[90] J Brötz and H Fuess, "Detwinning in $YBa_2Cu_3O_{7-\delta}$ films on vicinal $SrTiO_3$ (0 0 1) due to anisotropic strain at the interface", *Physica C* **339**, 75–78 (2000).

[91] T Terashima, K Shimura, Y Bando, Y Matsuda, A Fujiyama, and S Komiyama, "Superconductivity of one-unit-cell thick $YBa_2Cu_3O_7$ thin film", *Phys. Rev. Lett.* **67**, 1362 (1991).

[92] Y. Yu, L. Ma, P. Cai, R. Zhong, C. Ye, J. Shen, G. D. Gu, X. H. Chen, and Y. Zhang, "High-temperature superconductivity in monolayer $Bi_2Sr_2CaCu_2O_{8+\delta}$", *Nature* **575**, 156–163 (2019).

[93] G. Goltsman, O Okunev, G Chulkova, A Lipatov, A Semenov, K Smirnov, B Voronov, A Dzardanov, C Williams, and R. Sobolewski, "Picosecond superconducting single-photon optical detector", *Appl. Phys. Lett.* **79**, 705–707 (2001).

[94] R. Arpaia, D. Golubev, R. Baghdadi, R. Ciancio, G. Dražić, P. Orgiani, D. Montemurro, T. Bauch, and F. Lombardi, "Transport properties of ultrathin $YBa_2Cu_3O_{7-\delta}$ nanowires: A route to single-photon detection", *Phys. Rev. B* **96**, 064525 (2017).

[95] N Savvides and A Katsaros, "Growth and evolution of microstructure of epitaxial $YBa_2Cu_3O_{7-x}$ ultrathin and thin films on MgO", *Physica C* **226**, 23–36 (1994).

[96] P. Probst, K. Ilin, A. Engel, A. Semenov, H.-W. Hübers, J. Hänisch, B. Holzapfel, and M. Siegel, "Magnetoresistivity of thin $YBa_2Cu_3O_{7-\delta}$ films on sapphire substrate", *Physica C* **479**, 173–175 (2012).

[97] B. Halperin and D. R. Nelson, "Resistive transition in superconducting films", *J. Low Temp. Phys.* **36**, 599–616 (1979).

[98] B Fisher, J Genossar, C. Kuper, L Patlagan, G. Reisner, and A Knizhnik, "Effects of substituting calcium for yttrium on the properties of $YBa_2Cu_3O_{7-\delta}$", *Phys. Rev. B* **47**, 6054 (1993).

[99] E Osquiguil, M Maenhoudt, B Wuyts, and Y Bruynseraede, "Controlled preparation of oxygen deficient $YBa_2Cu_3O_x$ films", *Appl. Phys. Lett.* **60**, 1627–1629 (1992).

[100] J. MacManus-Driscoll, J. Alonso, P. Wang, T. Geballe, and J. Bravman, "Studies of structural disorder in $ReBa_2Cu_3O_{7-x}$ thin films (Re= rare earth) as a function of rare-earth ionic radius and film deposition conditions", *Physica C* **232**, 288–308 (1994).

[101] N. E. Hussey, "Phenomenology of the normal state in-plane transport properties of high-T_c cuprates", *J. Phys. Condens. Matter* **20**, 123201 (2008).

[102] O Cyr-Choinière, G Grissonnanche, S Badoux, J Day, D. Bonn, W. Hardy, R Liang, N Doiron-Leyraud, and L. Taillefer, "Two types of nematicity in the phase diagram of the cuprate superconductor $YBa_2Cu_3O_y$", *Phys. Rev. B* **92**, 224502 (2015).

[103] Y Liu, J. Qu, M Zhu, S. Zhang, S. Feng, and X. Li, "Stripe characterization in $La_{1.6-x}Nd_{0.4}Sr_xCuO_4$ thin films", *Phys. Rev. B* **70**, 224512 (2004).

[104] X. Sun, K. Segawa, and Y. Ando, "Low-temperature nodal-quasiparticle transport in lightly doped $YBa_2Cu_3O_y$ near the edge of the superconducting doping regime", *Phys. Rev. B* **72**, 100502 (2005).

[105] Y. Ando, Y Kurita, S. Komiya, S Ono, and K. Segawa, "Evolution of the Hall coefficient and the peculiar electronic structure of the cuprate superconductors", *Phys. Rev. Lett.* **92**, 197001 (2004).

[106] K. Segawa and Y. Ando, "Intrinsic Hall response of the CuO_2 planes in a chain-plane composite system of $YBa_2Cu_3O_y$", *Phys. Rev. B* **69**, 104521 (2004).

[107] N. Barišić, M. K. Chan, Y. Li, G. Yu, X. Zhao, M. Dressel, A. Smontara, and M. Greven, "Universal sheet resistance and revised phase diagram of the cuprate high-temperature superconductors", *Proc. Natl. Acad. Sci. U.S.A* **110**, 12235–12240 (2013).

[108] G Papari, F Carillo, D Stornaiuolo, L Longobardi, F Beltram, and F Tafuri, "High critical current density and scaling of phase-slip processes in YBaCuO nanowires", *Supercond. Sci. Technol.* **25**, 035011 (2012).

[109] P. Larsson, B. Nilsson, and Z. Ivanov, "Fabrication and transport measurements of $YBa_2Cu_3O_{7-x}$ nanostructures", *J. Vac. Sci. Technol B* **18**, 25–31 (2000).

[110] J Schneider, H Kohlstedt, and R Wördenweber, "Nanobridges of optimized $YBa_2Cu_3O_7$ thin films for superconducting flux-flow type devices", *Appl. Phys. Lett.* **63**, 2426–2428 (1993).

[111] S. Nawaz, R. Arpaia, F. Lombardi, and T. Bauch, "Microwave Response of Superconducting $YBa_2Cu_3O_{7-\delta}$ Nanowire Bridges Sustaining the Critical Depairing Current: Evidence of Josephson-like Behavior", *Phys. Rev. Lett.* **110**, 167004 (2013).

[112] R. Arpaia, S. Nawaz, F. Lombardi, and T. Bauch, "Improved nanopatterning for YBCO nanowires approaching the depairing current", *IEEE Trans. Appl. Supercond.* **23**, 1101505–1101505 (2013).

[113] S. Nawaz, R. Arpaia, T. Bauch, and F. Lombardi, "Approaching the theoretical depairing current in $YBa_2Cu_3O_{7-x}$ nanowires", *Physica C* **495**, 33–38 (2013).

[114] E. Trabaldo, M. Arzeo, R. Arpaia, R. Baghdadi, **E. Andersson**, F. Lombardi, and T. Bauch, "Noise properties of YBCO Nanostructures", *IEEE Trans. Appl. Supercond.* **27**, 1–4 (2017).

[115] J. Hoffman, E. W. Hudson, K. Lang, V. Madhavan, H Eisaki, S Uchida, and J. Davis, "A four unit cell periodic pattern of quasi-particle states surrounding vortex cores in $Bi_2Sr_2CaCu2O_{8+\delta}$", *Science* **295**, 466–469 (2002).

[116] T. Wu, H. Mayaffre, S. Krämer, M. Horvatić, C. Berthier, W. Hardy, R. Liang, D. Bonn, and M.-H. Julien, "Magnetic-field-induced charge-stripe order in the high-temperature superconductor $YBa_2Cu_3O_y$", *Nature* **477**, 191–194 (2011).

[117] L. J. Ament, M. Van Veenendaal, T. P. Devereaux, J. P. Hill, and J. Van Den Brink, "Resonant inelastic x-ray scattering studies of elementary excitations", *Rev. Mod. Phys.* **83**, 705 (2011).

[118] A. Achkar, R Sutarto, X Mao, F He, A Frano, S Blanco-Canosa, M Le Tacon, G Ghiringhelli, L. Braicovich, M. Minola, et al., "Distinct charge orders in the planes and chains of ortho-III-ordered $YBa_2Cu_3O_{6+\delta}$ superconductors identified by resonant elastic x-ray scattering", *Phys. Rev. Lett.* **109**, 167001 (2012).

[119] N. Brookes, F Yakhou-Harris, K Kummer, A Fondacaro, J. Cezar, D Betto, E Velez-Fort, A Amorese, G Ghiringhelli, L Braicovich, et al., "The beamline ID32 at the ESRF for soft X-ray high energy resolution resonant inelastic X-ray scattering and polarisation dependent X-ray absorption spectroscopy", *Nucl. Instrum. Methods Phys. Res. A: Accel. Spectrom. Detect. Assoc. Equip.* **903**, 175–192 (2018).

[120] H.-H. Kim, E Lefrançois, K Kummer, R Fumagalli, N. Brookes, D Betto, S Nakata, M Tortora, J Porras, T Loew, et al., "Charge density waves in $YBa_2Cu_3O_{6.67}$ probed by resonant x-ray scattering under uniaxial compression", *Phys. Rev. Lett.* **126**, 037002 (2021).

[121] A. Sinchenko, P. Grigoriev, P. Lejay, and P. Monceau, "Spontaneous breaking of isotropy observed in the electronic transport of rare-earth tritellurides", *Phys. Rev. Lett.* **112**, 036601 (2014).

[122] M. Naito and S. Tanaka, "Electrical transport properties in 2H-NbS_2,-$NbSe_2$,-TaS_2 and-$TaSe_2$", *J. Phys. Soc* **51**, 219–227 (1982).

[123] M Ejrnaes, L Parlato, R Arpaia, T Bauch, F Lombardi, R Cristiano, F Tafuri, and G. Pepe, "Observation of dark pulses in 10 nm thick YBCO nanostrips presenting hysteretic current voltage characteristics", *Supercond. Sci. Technol.* **30**, 12LT02 (2017).

[124] E. Abrahams and C. Varma, "What angle-resolved photoemission experiments tell about the microscopic theory for high-temperature superconductors", *Proc. Natl. Acad. Sci. U.S.A* **97**, 5714–5716 (2000).

[125] H. Yao, D.-H. Lee, and S. Kivelson, "Fermi-surface reconstruction in a smectic phase of a high-temperature superconductor", *Phys. Rev. B* **84**, 012507 (2011).

[126] F. Liu, M. Press, S. Khanna, and P Jena, "Magnetism and local order: Ab initio tight-binding theory", *Phys. Rev. B* **39**, 6914 (1989).

[127] R Daou, J Chang, D. LeBoeuf, O. Cyr-Choiniere, F. Laliberté, N. Doiron-Leyraud, B. Ramshaw, R. Liang, D. Bonn, W. Hardy, et al., "Broken rotational symmetry in the pseudogap phase of a high-T_c superconductor", *Nature* **463**, 519–522 (2010).

[128] M. Lawler, K Fujita, J. Lee, A. Schmidt, Y Kohsaka, C. K. Kim, H Eisaki, S Uchida, J. Davis, J. Sethna, et al., "Intra-unit-cell electronic nematicity of the high-T_c copper-oxide pseudogap states", *Nature* **466**, 347–351 (2010).

[129] A. V. Maharaj, I. Esterlis, Y. Zhang, B. Ramshaw, and S. Kivelson, "Hall number across a van Hove singularity", *Phys. Rev. B* **96**, 045132 (2017).

[130] Y. Gannot, B. J. Ramshaw, and S. A. Kivelson, "Fermi surface reconstruction by a charge density wave with finite correlation length", *Phys. Rev. B* **100**, 045128 (2019).

[131] J. Wu, A. Bollinger, X He, and I Božović, "Spontaneous breaking of rotational symmetry in copper oxide superconductors", *Nature* **547**, 432–435 (2017).

[132] L. Mangin-Thro, Y. Li, Y. Sidis, and P. Bourges, "a- b anisotropy of the intra-unit-cell magnetic order in $YBa_2Cu_3O_{6.6}$", *Phys. Rev. Lett.* **118**, 097003 (2017).

[133] L. Aslamasov and A. Larkin, "The influence of fluctuation pairing of electrons on the conductivity of normal metal", *Phys. Lett. A* **26**, 238–239 (1968).

[134] Z. Guguchia, D. Das, C. Wang, T. Adachi, N. Kitajima, M. Elender, F Brückner, S. Ghosh, V. Grinenko, T. Shiroka, et al., "Using uniaxial stress to probe the relationship between competing superconducting states in a cuprate with spin-stripe order", *Phys. Rev. Lett.* **125**, 097005 (2020).

[135] T. Boyle, M Walker, A Ruiz, E Schierle, Z Zhao, F Boschini, R Sutarto, T. Boyko, W Moore, N Tamura, et al., "Large response of charge stripes to uniaxial stress in $La_{1.475}Nd_{0.4}Sr_{0.125}CuO_4$", *Phys. Rev. Research* **3** (2021).

[136] M Platé, J. Mottershead, I. Elfimov, D. Peets, R. Liang, D. Bonn, W. Hardy, S Chiuzbaian, M Falub, M Shi, et al., "Fermi surface and quasiparticle excitations of overdoped $Tl_2Ba_2CuO_{6+\delta}$", *Phys. Rev. Lett.* **95**, 077001 (2005).

[137] B. Vignolle, A Carrington, R. Cooper, M. French, A. Mackenzie, C Jaudet, D Vignolles, C. Proust, and N. Hussey, "Quantum oscillations in an overdoped high-T_c superconductor", *Nature* **455**, 952–955 (2008).

[138] N Harrison and S. Sebastian, "Protected nodal electron pocket from multiple-Q ordering in underdoped high temperature superconductors", *Phys. Rev. Lett.* **106**, 226402 (2011).

[139] D. LeBoeuf, N. Doiron-Leyraud, B. Vignolle, M. Sutherland, B. Ramshaw, J Levallois, R Daou, F. Laliberté, O. Cyr-Choiniere, J. Chang, et al., "Lifshitz critical point in the cuprate superconductor $YBa_2Cu_3O_y$ from high-field Hall effect measurements", *Phys. Rev. B* **83**, 054506 (2011).

[140] L. Onsager, "Reciprocal relations in irreversible processes. II.", *Phys. Rev.* **38**, 2265 (1931).

[141] B. Ramshaw, N. Harrison, S. Sebastian, S Ghannadzadeh, K. A. Modic, D. Bonn, W. Hardy, R. Liang, and P. Goddard, "Broken rotational symmetry on the Fermi surface of a high-Tc superconductor", *npj Quantum Mater.* **2**, 1–6 (2017).

[142] O Cyr-Choinière, R Daou, F Laliberté, C Collignon, S. Badoux, D LeBoeuf, J Chang, B. Ramshaw, D. Bonn, W. Hardy, et al., "Pseudogap temperature T* of cuprate superconductors from the Nernst effect", *Phys. Rev. B* **97**, 064502 (2018).

[143] R Arpaia, M Arzeo, R Baghdadi, E Trabaldo, F Lombardi, and T Bauch, "Improved noise performance of ultrathin YBCO Dayem bridge nanoSQUIDs", *Supercond. Sci. Technol.* **30**, 014008 (2016).

[144] E. Trabaldo, C. Pfeiffer, **E. Andersson**, R. Arpaia, A. Kalaboukhov, D. Winkler, F. Lombardi, and T. Bauch, "Grooved Dayem nanobridges as building blocks of high-performance $YBa_2Cu_3O_{7-\delta}$ SQUID magnetometers", *Nano Lett.* **19**, 1902–1907 (2019).

[145] E Trabaldo, R Arpaia, M Arzeo, **E. Andersson**, D Golubev, F Lombardi, and T Bauch, "Transport and noise properties of YBCO nanowire based nanoSQUIDs", *Supercond. Sci. Technol.* **32**, 073001 (2019).

[146] C. M. Natarajan, M. G. Tanner, and R. H. Hadfield, "Superconducting nanowire single-photon detectors: physics and applications", *Supercond. Sci. Technol.* **25**, 063001 (2012).

[147] D. Y. Vodolazov, "Single-photon detection by a dirty current-carrying superconducting strip based on the kinetic-equation approach", *Phys. Rev. Appl.* **7**, 034014 (2017).

[148] M Lyatti, M. Wolff, A Savenko, M Kruth, S Ferrari, U Poppe, W Pernice, R. Dunin-Borkowski, and C Schuck, "Experimental evidence for hotspot and phase-slip mechanisms of voltage switching in ultrathin $YBa_2Cu_3O_{7-x}$ nanowires", *Phys. Rev. B* **98**, 054505 (2018).

[149] B Michon, A Ataei, P Bourgeois-Hope, C Collignon, S. Li, S Badoux, A Gourgout, F Laliberté, J.-S. Zhou, N. Doiron-Leyraud, et al., "Wiedemann-Franz law and abrupt change in conductivity across the pseudogap critical point of a cuprate superconductor", *Phys. Rev. X* **8**, 041010 (2018).

[150] D Golubev, F. Lombardi, and T. Bauch, "Effect of heating on critical current of YBCO nanowires", *Physica C* **506**, 174–177 (2014).

[151] M Ejrnaes, A Casaburi, O Quaranta, S Marchetti, A Gaggero, F Mattioli, R Leoni, S Pagano, and R Cristiano, "Characterization of parallel superconducting nanowire single photon detectors", *Supercond. Sci. Technol.* **22**, 055006 (2009).

[152] R. Arpaia, M Ejrnaes, L Parlato, R Cristiano, M. Arzeo, T. Bauch, S. Nawaz, F Tafuri, G. Pepe, and F. Lombardi, "Highly homogeneous YBCO/LSMO nanowires for photoresponse experiments", *Supercond. Sci. Technol.* **27**, 044027 (2014).

[153] M. Tinkham, *Introduction to superconductivity* (Courier Corporation, 2004).

[154] A. Sivakov, A. Glukhov, A. Omelyanchouk, Y Koval, P Müller, and A. Ustinov, "Josephson behavior of phase-slip lines in wide superconducting strips", *Phys. Rev. Lett.* **91**, 267001 (2003).

[155] V. Dmitriev, I. Zolochevskii, T. Salenkova, and E. Khristenko, "Critical currents, phase slip centers, and phase slip lines in superconducting films in the absence of external magnetic field", *Low Temp. Phys.* **31**, 127–136 (2005).

[156] L. Bulaevskii, M. Graf, C. Batista, and V. Kogan, "Vortex-induced dissipation in narrow current-biased thin-film superconducting strips", *Phys. Rev. B* **83**, 144526 (2011).

[157] B. Ramshaw, J. Day, B. Vignolle, D. LeBoeuf, P Dosanjh, C. Proust, L. Taillefer, R. Liang, W. Hardy, and D. Bonn, "Vortex lattice melting and H_{c2} in underdoped $YBa_2Cu_3O_y$", *Phys. Rev. B* **86**, 174501 (2012).

[158] J Demsar, B Podobnik, J. Evetts, G. Wagner, and D Mihailovic, "Evidence for crossover from a Bose-Einstein condensate to a BCS-like superconductor with doping in $YBa_2Cu_3O_{7-\delta}$ from quasiparticle relaxation dynamics experiments", *EPL* **45**, 381 (1999).

[159] P Bourgeois-Hope, S. Li, F Laliberté, S Badoux, S. Hayden, N Momono, T Kurosawa, K Yamada, H Takagi, N. Doiron-Leyraud, et al., "Link between magnetism and resistivity upturn in cuprates: a thermal conductivity study of $La_{2-x}Sr_xCuO_4$", *arXiv preprint arXiv:1910.08126* (2019).

[160] D. Gustafsson, D Golubev, M. Fogelström, T. Claeson, S. Kubatkin, T. Bauch, and F. Lombardi, "Fully gapped superconductivity in a nanometre-size $YBa_2Cu_3O_{7-\delta}$ island enhanced by a magnetic field", *Nat. Nanotechnol* **8**, 25–30 (2013).